



**NOAA-18 SBUV/2 (FM#7)
Activation and Evaluation Phase (A&E) Report**

Matthew T. DeLand, Liang-Kang Huang

*Science Systems and Applications, Inc. (SSAI)
10210 Greenbelt Rd., Suite 400
Lanham, MD 20706*

4 November 2005

Document # SSAI-2015-180-MD-2005-02

Table of Contents

	Figure List.....	ii
	Table List	iv
1.	Introduction.....	1
2.	Executive Summary	2
3.	Operations.....	4
4.	Housekeeping Data.....	6
5.	Electronic Offsets.....	15
6.	Wavelength Calibration	25
7.	Goniometric Calibration	39
8.	Thermal Response.....	49
9.	Interrange Ratios.....	54
10.	Nonlinearity Correction	64
11.	Diffuser Reflectivity Characterization.....	73
12.	Radiometric Calibration.....	90
13.	Solar Irradiance.....	96
14.	Out of Band Response Correction	101
15.	Ozone Validation	105
16.	Conclusion	110
	References.....	111

Figure List

4.1	Digital A telemetry time series	7-9
4.2	Digital B telemetry time series	9-11
4.3	Analog telemetry time series	11-14
5.1	Range 1 offset data for July-September 2005: All latitudes	19
5.2	Range 1 offset data for July-September 2005: SAA excluded	19
5.3	Range 1 daily offset values at Channel 1	20
5.4	Time series of Range 1, Range 2, Range 3, CCR offset at Channel 1 (new moon)	20-21
5.5	Spectral dependence of Range 1 offset (time-averaged data).....	21
5.6	Spectral dependence of Range 2 offset (time-averaged data).....	22
5.7	Spectral dependence of Range 3 anode offset (time-averaged data)	22
5.8	Spectral dependence of CCR offset (time-averaged data)	23
5.9	Range 1 offset data (sweep mode).....	23
5.10	Spectral dependence of Range 3 cathode offset	24
5.11	Time series of Range 3 cathode offset data	24
6.1	Sweep mode wavelength calibration line profile at 185.0 nm.....	34
6.2	Sweep mode line center positions at 185.0 nm.....	34
6.4	Sweep mode line center positions at 253.7 nm.....	35
6.4	Sweep mode line center positions at 404.8 nm.....	35
6.5	4-step discrete mode line profile at 253.7 nm.....	36
6.6	4-step discrete mode line center positions (time dependence).....	36
6.7	2-step discrete mode line profile at 185.0 nm.....	37
6.8	Calculated Hg line positions: Sweep mode Ebert coefficients	37
6.9	Calculated Hg line positions: Discrete mode Ebert coefficients	38
7.1	Prelaunch goniometry data at 350 nm, FEL lamp	43
7.2	Elevation dependence of inflight data: sweep mode, CCR	44
7.3	Elevation and wavelength dependence of inflight data: position mode, 340 nm	45
7.4	Wavelength dependence error of prelaunch goniometry	46
7.5	Goniometry wavelength dependence correction: Slope	46
7.6	Goniometry wavelength dependence correction: Y-intercept	47
7.7	Sweep mode solar data: All goniometric corrections applied	48
8.1	FM#7 thermal sensitivity: Range 2 prelaunch data	51
8.2	FM#7 thermal sensitivity: Range 3 cathode prelaunch data	51
8.3	FM#7 thermal sensitivity: Spectral dependence	52
9.1	Time series of IRR ₁₂ data at 283.0 nm.....	58
9.2	IRR ₁₂ spectral dependence of time dependence.....	58
9.3	IRR ₁₂ “Day 1” spectral dependence.....	59

9.4	IRR ₂₃ A “Day 1” spectral dependence.....	59
9.5	Position mode Earth view IRR ₂₃ A data vs. scan position.....	60
9.6	Time series of IRR ₂₃ A data at 305.8 nm.....	60
9.7	IRR ₂₃ A spectral dependence of time dependence.....	61
9.8	IRR ₂₃ A solar zenith angle dependence.....	61
9.9	IRR ₂₃ C prelaunch data and 4 th order wavelength-dependent fit.....	62
9.10	IRR ₂₃ C data vs. wavelength for Jun-Sep 2005, shifted prelaunch fit.....	62
9.11	IRR ₂₃ C time dependence at 312.6 nm.....	63
10.1	Prelaunch Range 1 nonlinearity data + Ball, SSAI fits.....	68
10.2	Prelaunch Range 2 nonlinearity data + Ball, SSAI fits.....	68
10.3	IRR ₂₃ C dependence on Range 2 counts using prelaunch nonlinearity correction.....	69
10.4	Position mode data at 380 nm (Range 2 counts) vs. CCR data [prelaunch nonlinearity]..	69
10.5	Inflight IRR ₂₃ A measurements at 312.6 nm [prelaunch Range 2 nonlinearity].....	70
10.6	Prelaunch Range 3 anode nonlinearity data + Ball, SSAI fits.....	70
10.7	Inflight IRR ₂₃ A measurements at 312.6 nm [revised Range 2 nonlinearity].....	71
10.8	Position mode data at 380 nm (Range 3 counts) vs. CCR data [prelaunch nonlinearity]..	71
10.9	Prelaunch Range 3 cathode nonlinearity data + Ball, SSAI fits.....	72
11.1	Onboard calibration system configurations: Lamp view, diffuser view.....	81
11.2	Sweep mode diffuser reflectivity calibration sequence.....	81
11.3	Mercury lamp spectrum: Lamp view, diffuser view.....	82
11.4	Sweep mode line profiles (lamp, diffuser): 253.7 nm, 404.8 nm.....	82
11.5	Line intensity evolution (sweep mode).....	83
11.6	Diffuser reflectivity time series (no polarity correction).....	83
11.7	Discrete mode reflectivity measurement sequence.....	84
11.8	Discrete mode line profiles (lamp, diffuser): 404.8, 253.7 nm.....	84
11.9	Line intensity evolution (discrete) at 253.7 nm.....	85
11.10	Line intensity evolution (discrete) at 404.8 nm.....	85
11.11	Hg lamp intensity time series at 253.7 nm: Lamp view, diffuser view.....	86
11.12	Diffuser reflectivity time series (with polarity correction).....	86
11.13	Diffuser plate temperature, heater current during decontamination procedure.....	87
11.14	Diffuser reflectivity time series at 253.7 nm: June-September 2005.....	87
11.15	Diffuser reflectivity time series at 404.8 nm: June-September 2005.....	88
11.16	Diffuser reflectivity changes after solar exposure.....	88
11.17	Reflectivity change spectral dependence: On-orbit vs. prelaunch reference.....	89
12.1	FM#7 sweep mode air-vacuum calibration ratio.....	94
12.2	Sweep/discrete calibration ratio.....	94
12.3	NOAA-18 “Day 1” discrete solar irradiances vs. SSBUV-2.....	95
13.1	NOAA-18 “Day 1” sweep solar irradiances vs. Thuillier reference spectrum.....	98
13.2	Sweep mode irradiance ratio: 2005/242 vs. 2005/171 + air/vacuum calibration ratio.....	98
13.3	Position mode solar data at 400 nm, 2005/172.....	99
13.4	Power spectral analysis of sweep solar data.....	100

14.1	Albedo error at 273.7 nm vs. CCR albedo	103
14.2	Slit function model for OOB analysis	103
14.3	FM#7 OOB correction coefficient spectral dependence	104
14.4	Calculated NOAA-18 OOB radiance error at high reflectivity.....	104
15.1	NOAA-18 V6 total ozone: Difference between B-pair and D-pair	106
15.2	Comparison of V6 total ozone values between NOAA-18 and NOAA-16	107
15.3	Comparison of V8 total ozone values between NOAA-18 and NOAA-16	108
15.4	Comparison of V8 profile layer ozone values between NOAA-18 and NOAA-16	109

Table List

3.1	NOAA-18 SBUV/2 standard operational schedule	5
5.1	Electronic offset values in discrete mode	18
5.2	Electronic offset values in sweep mode.....	18
6.1	Sweep mode Hg lamp line centers: Inflight.....	30
6.2	2-step discrete mode Hg lamp line centers: Inflight	30
6.3	Ebert coefficients for wavelength calibration	30
6.4	Recommended operational grating positions and wavelengths	31
6.5	Lamp view <i>vs.</i> diffuser view line centers: Discrete mode	32
6.6	Lamp view <i>vs.</i> diffuser view line centers: Sweep mode.....	32
6.7	Spectral resolution: Prelaunch, discrete mode	33
6.8	Spectral resolution: Inflight, sweep mode	33
7.1	Standard goniometric fit coefficients.....	41
7.2	Goniometric elevation correction coefficients.....	41
7.3	Wavelength-dependent goniometric correction: Y-Intercept	41
7.4	Wavelength-dependent goniometric correction: Slope.....	42
8.1	PMT temperature dependence correction	50
9.1	IRR _{23C} wavelength dependence fit coefficients.....	57
9.2	IRR _{23C} values at ozone wavelengths.....	57
10.1	Non-linearity correction functions.....	67
11.1	Hg lamp polarity correction: On-orbit data	80
11.2	Diffuser reflectivity changes following solar exposure	80
11.3	Prelaunch diffuser reflectivity calibration	80
12.1	Calibration adjustment factors for ozone processing.....	91
12.2	Revised radiance calibration constants	92
12.3	Revised irradiance calibration constants.....	92
12.4	“Day 1” solar irradiance at ozone wavelengths	93
14.1	Revised OOB _R correction coefficients.....	102
15.1	Total ozone pair adjustment factors relative to A-pair	105
16.1	Ozone processing calibration data for NOAA-18 SBUV/2.....	110

1. Introduction

The SBUV/2 Flight Model #7 (FM#7) instrument is the latest in a series of remote-sensing instruments flown by NOAA to monitor stratospheric profile ozone and total column ozone abundances. SSAI is responsible for providing calibration parameters to NOAA for use in the operational ozone processing system (OOPS). Prelaunch calibration values were developed using data from the Specification Compliance and Calibration Data Book (hereafter Data Book) delivered by Ball Aerospace [*Ball Aerospace*, 2004]. SSAI used these data to derive initial V6 processing parameters, which were delivered to NOAA on January 31, 2005 [*DeLand et al.*, 2005]. The FM#7 instrument was launched on the NOAA-18 satellite on May 20, 2005.

The SBUV/2 FM#7 instrument first collected radiance data on June 3, 2005 (Julian day 154), and began making solar irradiance measurements on June 20, 2005. Initial solar irradiance measurements showed significant wavelength-dependent changes in the radiometric calibration, ranging from -2% at 331 nm to -9% at 273 nm. Additional data gathered during on-orbit Activation and Evaluation (A&E) phase operations evaluated the prelaunch wavelength calibration, non-linearity, interrange ratio, electronic offset, and goniometric correction results. A memo presenting recommended calibration changes was delivered to NOAA on July 17, 2005. Following the implementation of these changes, regular operations including solar and other calibration measurements began August 30, 2005. NOAA/NESDIS officially began operational ozone processing on that date. A preliminary time-dependent and wavelength-dependent instrument characterization was delivered on September 21, 2005 to improve the accuracy of NOAA-18 ozone data during the NOAA/NESDIS transition to new computing systems in fall 2005.

This report is intended to summarize the SBUV/2 FM#7 instrument status as of the beginning of operational processing. NOAA-18 inflight data evaluated here end on September 30, 2005 unless otherwise noted. In general, the NOAA-18 SBUV/2 calibration presented in this report is not intended to be completely representative of the instrument status for an indefinite period of time. SSAI will track instrument performance on a regular basis. We expect to update the NOAA-18 instrument characterization in early 2006, and intend to provide further updates at 6-12 month intervals.

2. Executive Summary

The body of this report discusses the detailed procedures used in characterizing the NOAA-18 SBUV/2 instrument and the results obtained. Brief summaries of each major section are provided below.

Operations. Activation and Evaluation phase tests were completed in July 2005. Additional special tests were conducted in late July and early August. The instrument began its normal schedule of measurements in late August 2005.

Housekeeping Data. Temperature, voltage, and current data are well-behaved. No grating drive problems have been observed.

Electronic Offsets. The Range 1 offset value is higher than for previous SBUV/2 instruments, consistent with prelaunch electronics modifications. The noise level is comparable to NOAA-17. Range 2 and Range 3 anode offset data show very low noise levels, as expected. Range 3 cathode noise is comparable to NOAA-17. There is no evidence of periodic behavior in Range 3 cathode mode data.

Wavelength Calibration. Prelaunch data taken after thermal vacuum testing showed an absolute offset from the reference wavelength calibration. This offset was adopted for initial on-orbit processing. A&E phase tests indicated that a different offset was appropriate for inflight measurements, so a revised wavelength calibration was created.

Goniometric Calibration. The initial goniometric correction derived from prelaunch data showed errors up to ~1% when it was applied to on-orbit solar data. An empirical elevation angle-dependent correction was derived. A wavelength dependence correction was derived from inflight position mode data.

Thermal Response. A wavelength-dependent correction for radiometric sensitivity changes based on PMT temperature variations was derived from prelaunch calibration data. A separate correction function was derived for Range 3 cathode data.

Interrange (Gain) Ratios. IRR_{12} values show a minimal wavelength dependence ($< 0.2\%$). A constant IRR_{12} value is recommended for operational processing. Inflight values of IRR_{23} measured with Range 3 anode data are ~8% lower than prelaunch data taken in 1995. This decrease is consistent with radiometric calibration changes observed after 1998 electronics modifications to the FM#7 instrument. A revised constant IRR_{23A} value is recommended for operational processing. Range 3 cathode IRR_{23} values were measured twice during A&E phase activities, and showed a decrease from the prelaunch estimate as well as on-orbit changes. A time-dependent characterization of PMT sensitivity change was developed using early operational data.

Nonlinearity Correction. The prelaunch nonlinearity corrections for all gain ranges have magnitudes $< 1\%$. On-orbit data showed an error in the Range 2 correction function at high count

levels (>45,000 counts), reaching +0.8% for the maximum signals used in ozone processing. A revised function was derived for operational use.

Diffuser Reflectivity. Initial on-orbit reflectivity values show fluctuations of less than $\pm 2\%$ relative to the prelaunch baseline data, but no apparent overall shift. The magnitude of reflectivity changes caused by mercury lamp polarity switching is smaller than the polarity term observed for NOAA-14. Discrete and sweep mode data are in good agreement. No correction for diffuser reflectivity changes has been made in the analysis of radiometric calibration changes.

Radiometric Calibration. Sweep mode and discrete mode calibration values agree to within 0.5% after adjusting for nominal integration time differences. Air and vacuum calibration data differ by $\pm 3\%$ at ozone wavelengths. "Day 1" discrete mode solar irradiances at ozone wavelengths are lower than predicted by SSBUV-2 data, with an approximate 5-6% spectral dependence. The CCR solar irradiance value is also lower than SSBUV. Sweep and discrete calibration data agree to within $\pm 0.5\%$.

Solar Irradiance. Sweep mode irradiance comparisons with reference data show spectrally dependent differences over a broad region, with a minimum difference of -3% at 360 nm and a maximum difference of -10% at 190 nm. Additional spectrally dependent sensitivity decreases were observed during early on-orbit operations. Outgassing of water vapor from MgF_2 -coated surfaces on the depolarizer is believed to be responsible for this behavior. All irradiance measurements show regular fluctuations of 0.3-0.6% peak-to-peak, with an approximate period of 8.7 seconds. These variations are induced by pitch angle oscillations of the NOAA-18 satellite.

Out-of-Band Response (OOBR) Correction. Prelaunch OOBR correction values were taken from NOAA-17 results, based on comparisons of FM#6 and FM#7 mercury lamp spectra. On-orbit measurement results for short wavelengths (252-292 nm) showed that smaller corrections were appropriate for NOAA-18 data. A modified instrument slit function model was used to generate OOBR correction coefficients for longer wavelengths (297-306 nm).

Ozone Validation. Initial ozone processing showed large total ozone pair differences (25-30 DU) using the prelaunch radiometric calibration. When solar flux values with spectrally-dependent calibration changes determined from on-orbit measurements were adopted, the pair differences were reduced to less than 5 DU. Initial total ozone comparisons with NOAA-16 show good agreement in both V6 and V8 products. V8 profile ozone comparisons with NOAA-16 at the Equator are within 10% at all altitudes, and most differences are less than $\pm 5\%$.

3. Operations

The NOAA-18 satellite was launched on May 20, 2005 (day 140). The SBUV/2 FM#7 instrument high voltage power supply (HVPS) was turned on June 4 (day 155), and radiance data were first collected on June 5. Initial solar irradiance data were not collected until June 20 (day 171) to allow sufficient time for outgassing. The nominal A&E phase tests were scheduled to last approximately 25 days following HVPS turn-on. The last A&E tests were finished on July 6, 2005, and revised calibration parameters for ozone processing were delivered on July 17, 2005. Following testing by NOAA/NESDIS, the normal operational schedule began on August 30, 2005.

Table 3.1 gives the normal operating schedule for NOAA-18 SBUV/2. The SBUV/2 instrument normally makes continuous discrete mode Earth view measurements at the 12 ozone wavelengths over the daytime portion of the Earth. Solar irradiance measurements can only be initiated at the day-night terminator. Daily solar observations are made in sweep mode over the wavelength range 160-406 nm, and in discrete mode across the Mg II absorption line at 280 nm. Weekly solar observations are made in discrete mode at the ozone wavelengths, and monthly position mode solar observations are made for tracking the goniometric calibration. Diffuser reflectivity measurements using the on-board mercury lamp calibration system are made every week on the night side of a selected orbit. Supplemental electronic offset data are also collected once per week by closing the calibration lamp door on the night side. Range 3 cathode Earth view measurements are made for four consecutive orbits once per week.

Some special measurements were made prior to the start of normal operations. One test on 2005/156 used a special set of three discrete wavelengths surrounding the Mg II absorption line (repeating the wavelength sequence 4 times within each discrete scan) to gather additional data about the FM#7 out-of-band response (OOBR) error. The wavelengths used for this test are listed in Table 6.4. Position mode data were collected at 380 nm on day 155 to provide comparison between monochromator and CCR measurements of the same scene. Two orbits of Earth view data on August 15 (day 227) were collected with the solar diffuser deployed to evaluate how well the diffuser prevents surface light from contaminating the solar measurement.

The NOAA-18 SBUV/2 instrument can collect Range 3 data in either anode mode or cathode mode. Range 3 anode mode will be used for normal ozone observations because the data have much less noise. However, continuous Range 3 anode operations do not provide independent tracking of PMT gain changes (see Section 9). Periodic Range 3 cathode operations are therefore used to provide data for monitoring the interranger ratio (IRR_{23C}), and thus PMT gain changes. Calibration data and ozone processing software modifications are provided to NOAA/NESDIS to permit continuous ozone processing during these periods.

TABLE 3.1
NOAA-18 SBUV/2 Standard Operational Schedule

Frequency	Mode	View	Wavelengths
Continuous	Discrete	Earth	Ozone [252-340 nm]
Daily	Discrete	Solar	Mg II [276-284 nm]; <i>9 scans</i>
Daily	Sweep	Solar	160-406 nm; <i>2 consecutive scans</i>
Weekly	Discrete	Solar	Ozone [252-340 nm]; <i>9 scans</i>
Weekly	Sweep	Hg lamp	Diffuser reflectivity; <i>10 scans</i>
Weekly	Discrete	Lamp (closed)	Ozone [electronic offset]; <i>30 minutes</i>
Weekly	Discrete	Earth	Ozone [Rng. 3 cathode]; <i>4 consecutive orbits</i>
Monthly	Position	Solar	400, 200 nm [goniometry]; <i>15 minutes each</i>

4. Housekeeping Data

The most fundamental information about the operational status of the SBUV/2 instrument comes from the digital and analog telemetry data, collectively referred to here as “housekeeping” data. These data consist of voltages, currents, absolute temperatures, and differential temperatures measured at various locations on the instrument. Samples are taken every 16 seconds, so that each daily average value represents the mean of approximately 5000 measurements. Figures 4.1a-4.1m show time series of daily average data from the Digital “A” telemetry channels taken between June 1, 2005 and September 30, 2005. Values are recorded at 8-bit resolution and converted to engineering units. Nominal telemetry values typically vary over only a small portion of the overall range, leading to visible steps in voltage and current channels which are in reality extremely stable (*e.g.* ECAL reference voltage, Figure 4.1f). Figures 4.2a-4.2l show corresponding time series for the Digital “B” telemetry channels, and Figures 4.3a-4.3p show time series of analog telemetry data. A complete description of parameters monitored by each telemetry channel can be found in the SBUV/2 User’s Guide [*SASC Technologies, 1986*].

In general, the NOAA-18 SBUV/2 instrument has enjoyed good health. Most component temperatures, such as the CCR diode (Figure 4.2f), PMT cathode (Figure 4.2k) and chopper motor (Figure 4.3f), were regularly between 21-24°C except on June 19-20, 2005. The calibration lamp heater was accidentally turned off following the diffuser decontamination procedure on June 19 (day 170), and was not turned on again until late on June 20. Most component temperatures dropped by 2-4°C during this period. The calibration lamp temperature decreased by a much larger amount when the heater was off, from ~55°C to 20-25°C (Figure 4.1e). The Hg lamp output was unstable during this cold period, as described in more detail in Section 11. The PMT high voltage power supply (HVPS, Figure 4.1c) has been stable between 1007.4 and 1008.2 volts. Most low voltage power supplies fluctuated by only ~0.1% of their average values (Figures 4.1d-f).

An additional indicator of good instrumental health is that the NOAA-18 SBUV/2 grating drive behaved very well. The grating drive positions were decoded and monitored for every spectral scan. No grating drive errors were found. The grating drive was firmly locked in the designated grating positions in both discrete mode and sweep mode. Since no grating drive errors were observed, the statistical charts for the grating drive position errors are not included in this report.

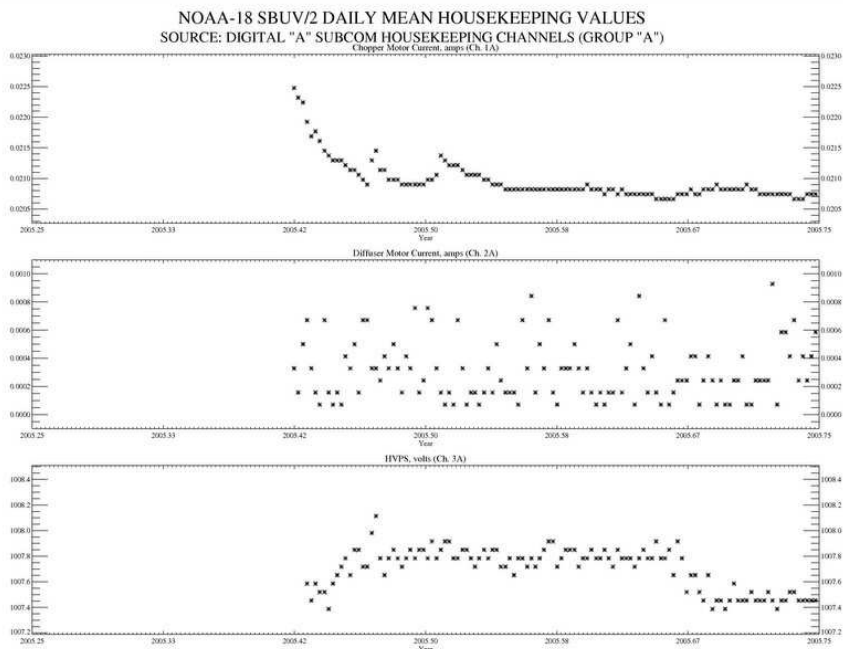


Figure 4.1: Digital A housekeeping values: (a) Chopper motor current; (b) Diffuser motor current; (c) High voltage power supply.

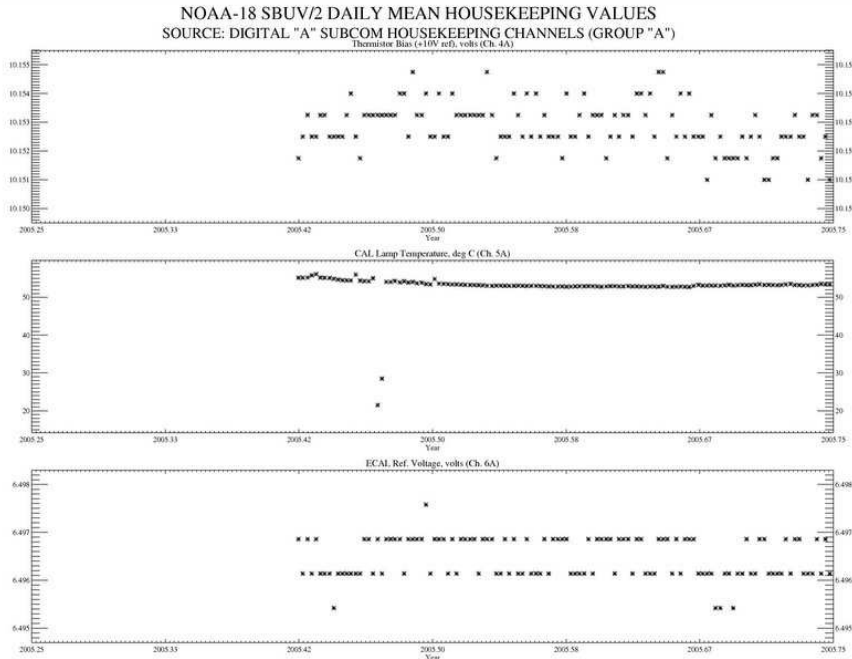


Figure 4.1: Digital A housekeeping values: (d) Thermistor bias; (e) Calibration lamp temperature; (f) ECAL reference voltage.

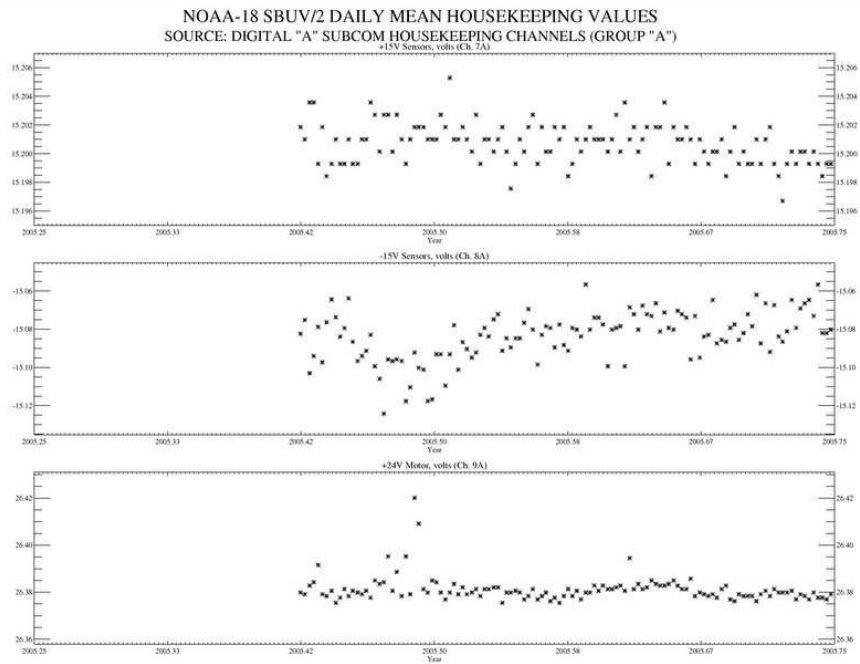


Figure 4.1: Digital A housekeeping values: (g) +15 V sensor; (h) -15 V sensor; (i) +24 V motor.

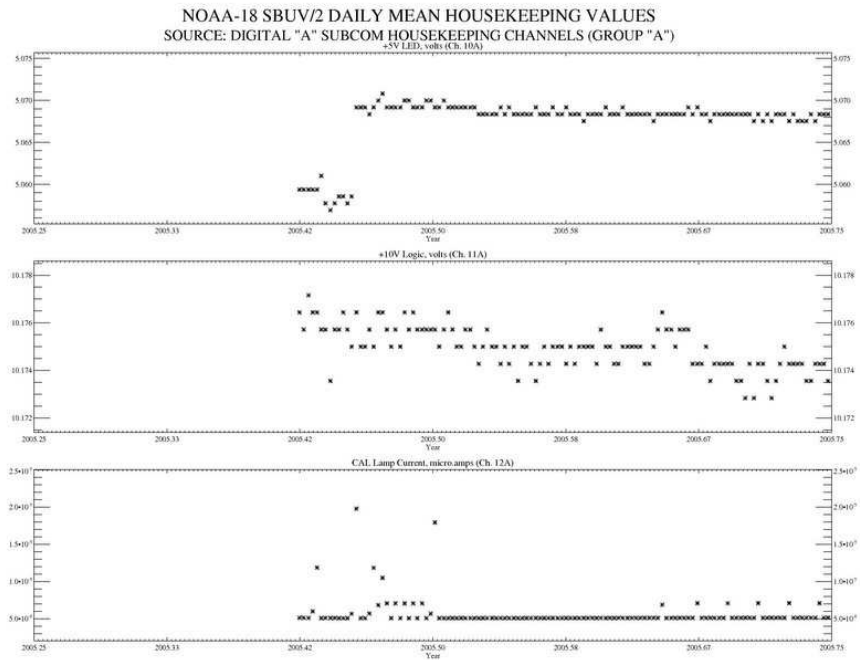


Figure 4.1: Digital A housekeeping values: (j) +5 V LED; (k) +10 V logic; (l) Calibration lamp current.

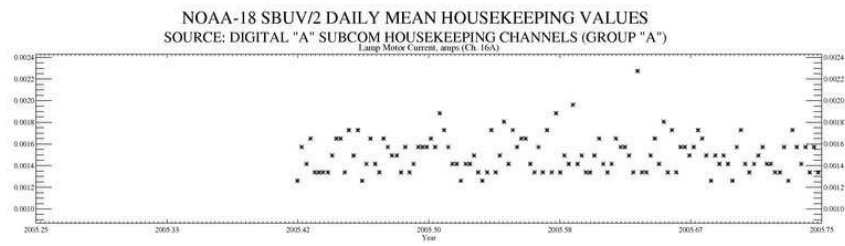


Figure 4.1: Digital A housekeeping values: (m) Lamp motor current.

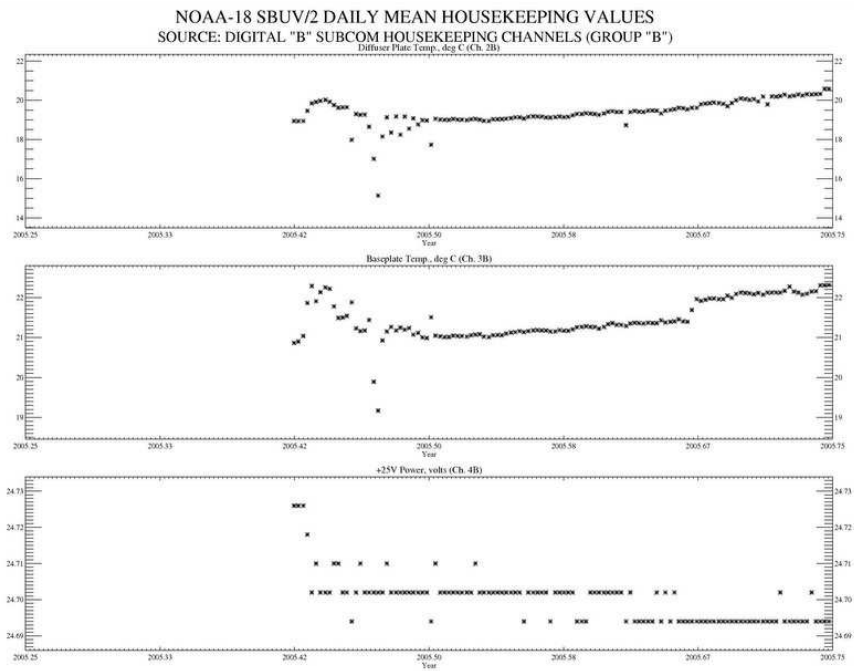


Figure 4.2: Digital B housekeeping values: (a) Diffuser plate temperature; (b) Baseplate temperature; (c) +25 V power.

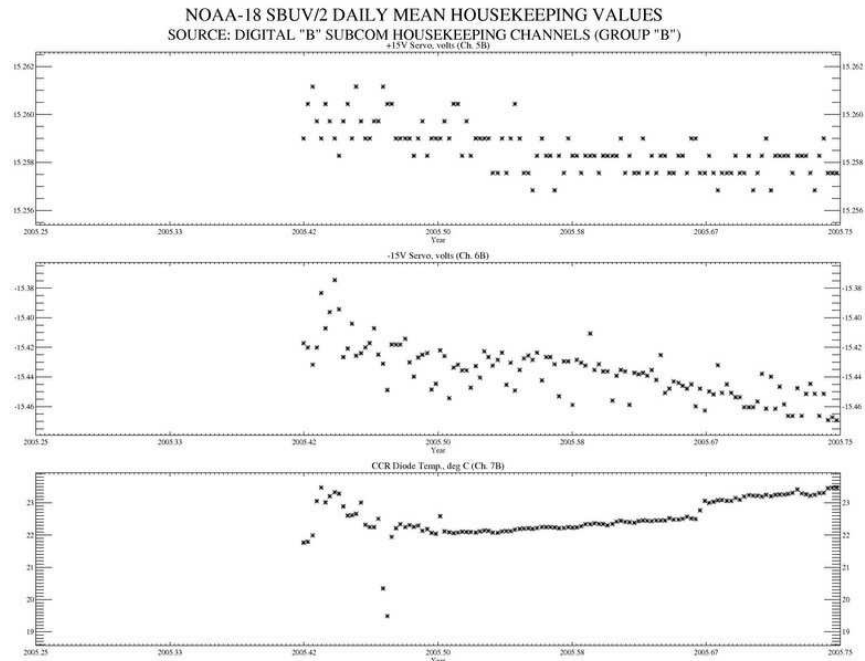


Figure 4.2: Digital B housekeeping values: (d) +15 V servo; (e) -15 V servo; (f) CCR diode temperature.

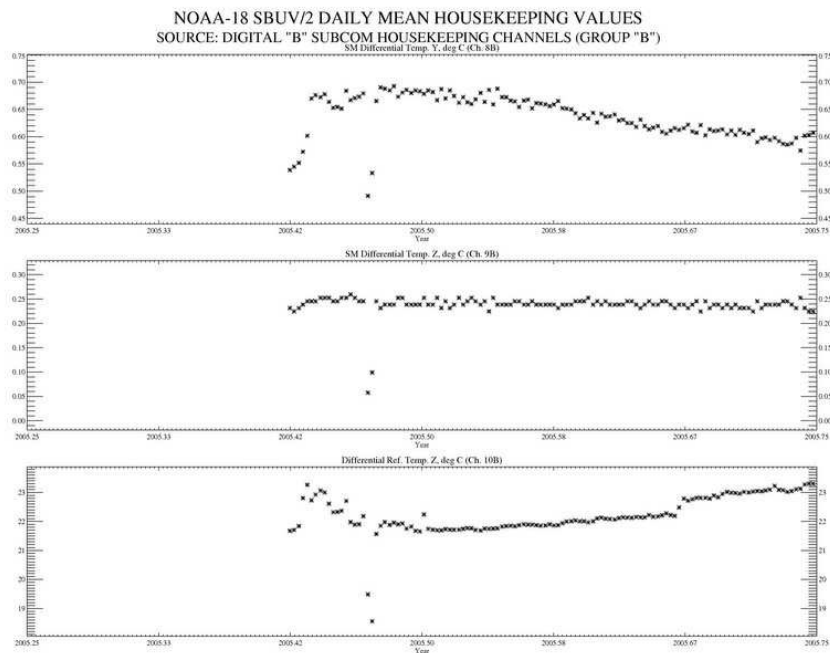


Figure 4.2: Digital B housekeeping values: (g) SM differential temperature Y; (h) SM differential temperature Z; (i) Differential reference temperature Z.

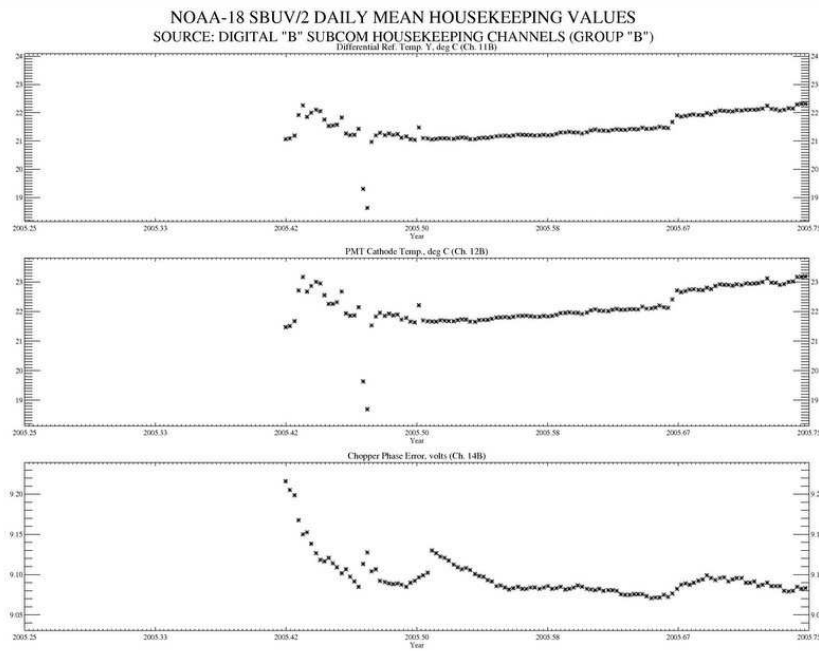


Figure 4.2: Digital B housekeeping values: (j) Differential reference temperature Y; (k) PMT cathode temperature; (l) Chopper phase error.

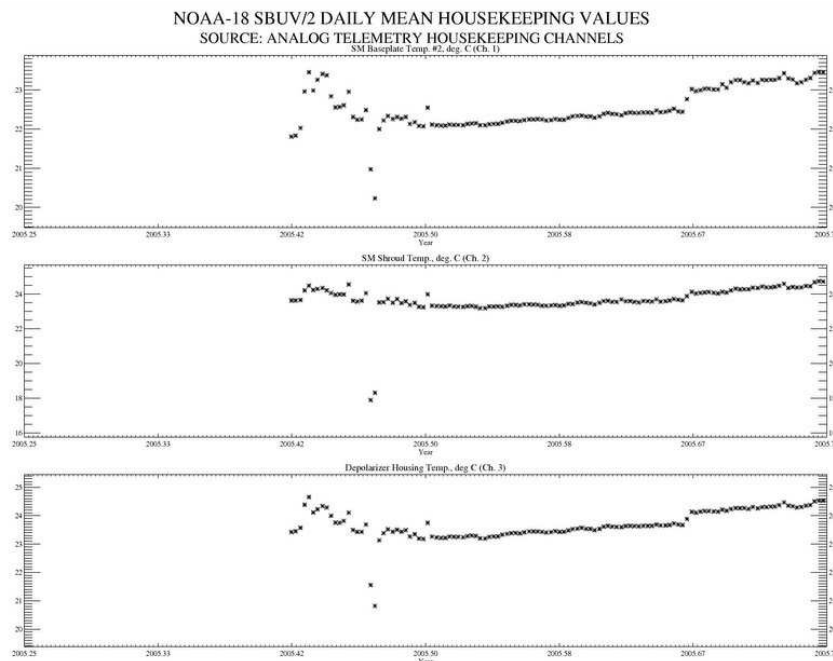


Figure 4.3: Analog housekeeping values: (a) SM baseplate temperature #2; (b) SM shroud temperature; (c) Depolarizer housing temperature.

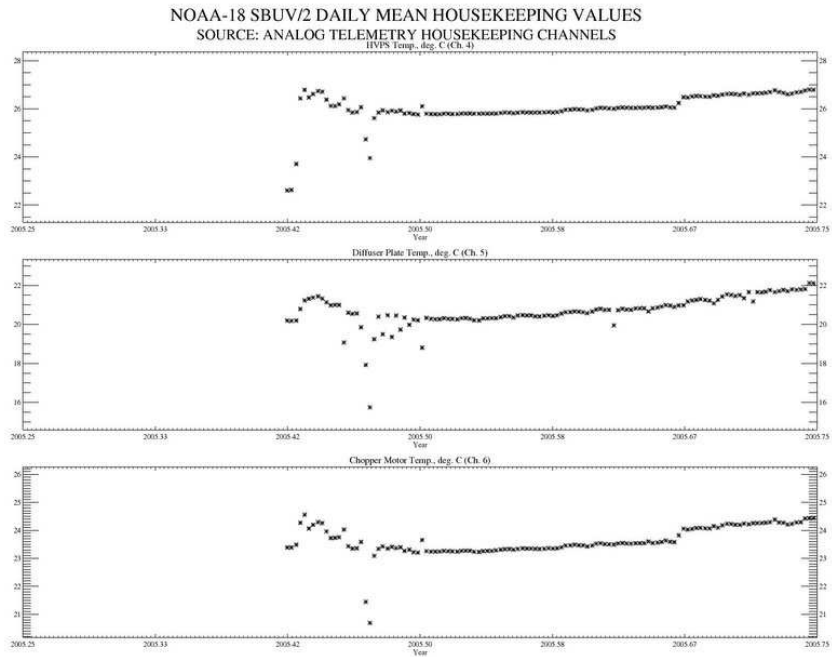


Figure 4.3: Analog housekeeping values: (d) High voltage power supply temperature; (e) Diffuser plate temperature; (f) Chopper motor temperature.

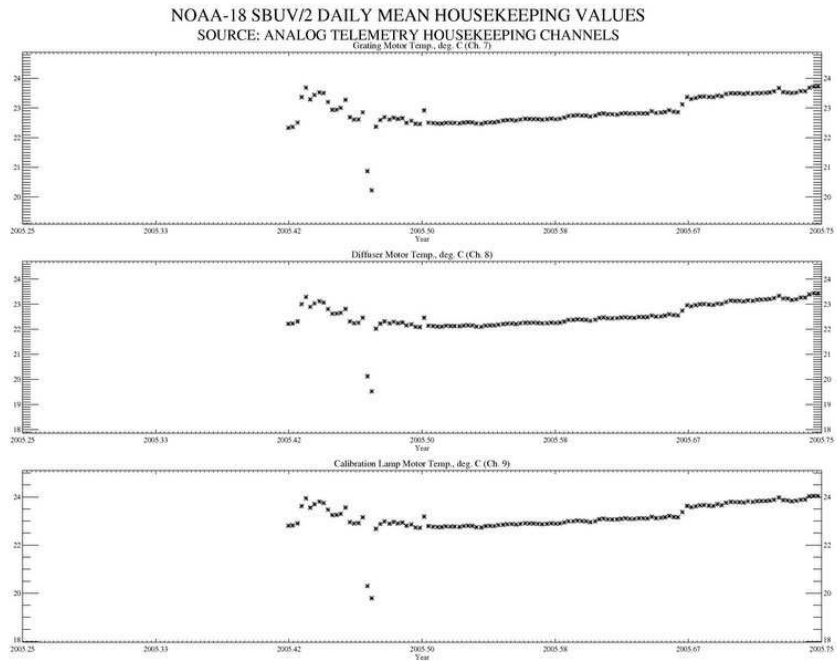


Figure 4.3: Analog housekeeping values: (g) Grating motor temperature; (h) Diffuser motor temperature; (i) Calibration lamp motor temperature.

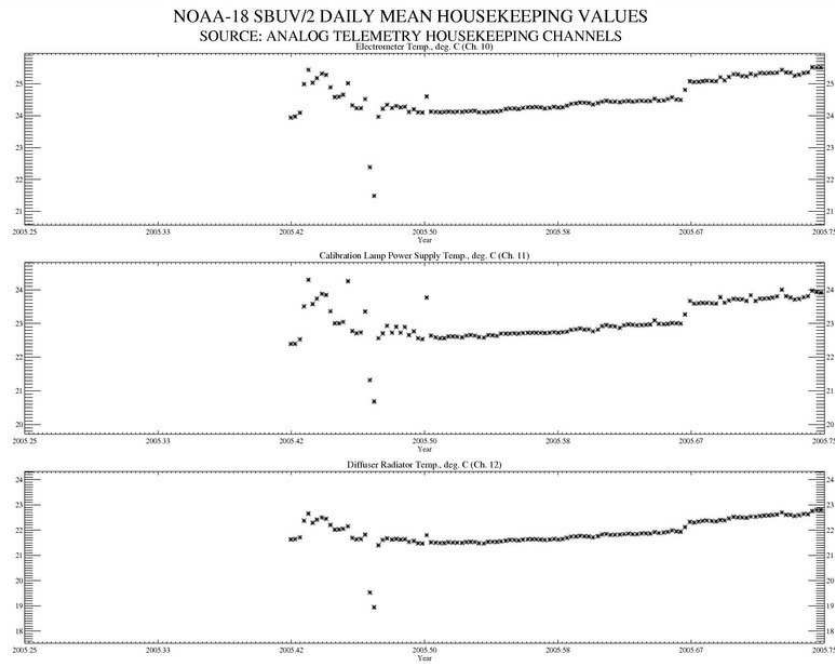


Figure 4.3: Analog housekeeping values: (j) Electrometer temperature; (k) Calibration lamp power supply temperature; (l) Diffuser radiator temperature.

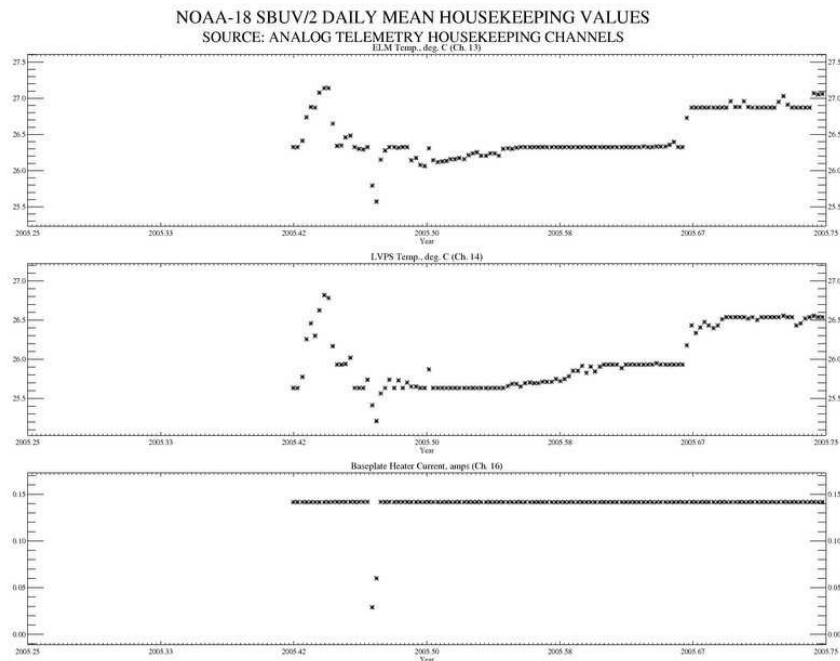


Figure 4.3: Analog housekeeping values: (m) ELM temperature; (n) Low voltage power supply temperature; (o) Baseplate heater current.

5. Electronic Offsets

During times when the input signal to the SBUV/2 instrument is very weak (*e.g.* night side of the orbit), normal electronic fluctuations could cause counter underflows that could confuse the ozone processing algorithm. This situation is avoided by setting the digital counters to a small positive bias prior to the start of sample integrations. These bias values are called the electronic offset. For previous SBUV/2 instruments, a nominal value of 64 counts was set for all PMT gain ranges and the CCR. The Range 1 offset value was increased to approximately 113 counts for the FM#7 instrument because of increased noise levels (~ 30 counts standard deviation) observed in prelaunch testing, so that a -3σ fluctuation in a dark scene measurement would still yield a positive count signal. The electronic offsets are monitored during normal operations to track spectral and temporal variations. During the A&E phase, SBUV/2 electronic offset data are examined for contamination from external sources, temporal variations, and spectral dependence.

5.1. Measurement Criteria and South Atlantic Anomaly

Selection of appropriate discrete Earth view measurements for electronic offset calculations requires consideration of weak radiance sources such as near-terminator airglow and reflected moonlight, particularly for Range 1 data. For this analysis, only data with solar zenith angles $\chi > 120^\circ$ are accepted, and the measurement date is required to be within ± 6 days of a new moon. These criteria reject data potentially contaminated by backscattered solar and lunar signals, respectively.

The SBUV/2 instrument has a light chopper and phase lock amplifier to minimize the electronic noise and bias. The chopper wheel is designed to remove biases from charged particles in the South Atlantic Anomaly (SAA) region, roughly defined by 30°N to 60°S latitude and 60°E to 180°W longitude. Figure 5.1 shows Range 1 offset data for each channel measured in 5 day periods around new moon dates from July 31 to September 8, 2005, plotted as a function of latitude in 2° bins. The increased offset values for Channel 6 at latitudes poleward of 50°S are believed to represent auroral emissions from the O I line at 297.23 nm, which can also be observed at latitudes greater than 50°N in Northern Hemisphere winter. The smallest standard deviations are seen between 0 - 50°N . The increased standard deviation values centered at about 20°S are due to noise associated with the SAA. When the SAA region is excluded from the analysis, the standard deviations at 20°S become comparable to the values in the Northern Hemisphere (Figure 5.2). Meanwhile, the average offset around 20°S remains at the same level, indicating that the chopper is functioning properly.

Significant signal increases are observed at Channel 6 (297 nm) in a narrow latitude band around 55°S within selected longitude 70°E to 160°E (Figure 5.2), possibly due to crossing a bright segment of the auroral oval ring. Similar behavior with progressively weaker amplitude is observed at Channels 9, 7, 2, and 3. The auroral ring signature at 297.5 nm is greatly reduced in the full data set (Figure 5.1) due to the increased number of samples. For the NOAA-9, NOAA-11, and NOAA-14 SBUV/2 instruments, the average of 11 channels, excluding Channel 6 due to

potential contamination, was used for the Range 1 offset calibrations. Since the identification of significant Range 1 offset drift in NOAA-16 SBUV/2 operation, night side earth view measurements at 252 nm (Channel 1) have been used for the Range 1 offset correction. This wavelength is not affected by either auroral emission or lunar contamination, and thus average offset values can be calculated every day. Including the SAA region in the Channel 1 offset calculations increases the average value by only 0.28 count (with standard error 3-4 counts). Night side offset data are also collected with the Hg lamp door closed for one orbit per week to provide measurements where no source is present. The top panel in Figure 5.3 shows the daily average of the Range 1 offset measurements at 252 nm, where diamonds represent measurements with the instrument door closed and long ticks on the date axis indicate new moon days. The Earth view measurements at 252 nm are not affected by lunar light and are in good agreement with the door-closed measurements. The daily average standard deviation is approximately 32 counts. This large Range 1 noise level was also found with the FM#6 instrument on NOAA-17, which also had a notch filter added prior to launch.

5.2. Time Dependence

Time series plots of the daily average offset values around new moon days for Range 1, Range 2, Range 3 anode, and CCR data are shown in Figures 5.4*a-d*. Only data for Channel 12 (339.9 nm) are presented as examples. No time dependent trend of the Range 1 daily averages is observed. Day-to-day variations are considered to be statistical fluctuations, since they do not exceed the daily average 2σ value. Therefore, a constant Range 1 offset is recommended. An average of all Channel 1 daily averages is 114.28 counts with a standard error of 0.20 counts. This result is consistent with the prelaunch estimate presented in *DeLand et al.* [2005], where the uncertainty represented the standard deviation from averaging multiple test results. The combined average of the 252 nm daily Range 1 offset values is listed in Table 1, where the standard error is approximately 0.2 counts. Noise levels for Range 2, Range 3 anode, and CCR data are very low (note the change of scale in Figures 5.4*b-d*), with standard deviations of 0.8 counts for the daily averages. All offsets listed here are time-independent.

5.3. Spectral Dependence

Figures 5.5-5.8 show the spectral dependence of temporally averaged electronic offset values around new moon days for each gain range and the CCR. As discussed in Section 5.1, many long wavelength channels in Range 1 are susceptible to resonant or fluorescent scattered light from atmosphere constituents such as O, O₂ and N₂. Therefore, only Channel 1 data were used to derive the Range 1 offset. The spectral variations of Range 2, Range 3 and CCR offset values are less than 0.2 counts, and are negligible. Data from all 12 channels are therefore averaged to derive these offset values.

5.4. Sweep Mode

In the sweep mode, the electronic offsets are typically calculated from discrete values, using the relationship

$$X_{\text{sweep}} = (X_{\text{discrete}} - X_{\text{nominal}})/12.5 + X_{\text{nominal}}$$

To adjust for the difference in signal integration time. X_{nominal} is a nominal value preset for the offset in each output range. Before NOAA-18, X_{nominal} was always 64 for all output ranges. Since NOAA-18 has the Range 1 offset value in discrete mode adjusted to 113.41, X_{nominal} for Range 1 must be increased accordingly. We examined the sweep mode offset with door-closed data taken on June 4-5, 2005. Only Range 1 offsets can be examined because the SBUV/2 instrument automatically selects the gain range for sweep mode data. Using global average counts over 160-175 nm, where the terrestrial radiance is also very low, we derived a Range 1 offset of 113.69 counts. The discrete mode offset average on these two days, also with door closed, was 113.22 counts. Therefore, it is sufficiently accurate to assign X_{nominal} for Range 1 equal to 113.41, the same value as in the prelaunch Range 1 offset.

The door-closed sweep mode measurements can be used to check if FM#7 has any light leak. In the short wavelength region 160-175 nm, the residual counts after applying the sweep mode offset correction were effectively zero at all solar zenith angles (SZA), as shown in Figure 5.9a. At 392-406 nm, the average residual signal was effectively zero for samples taken at and SZA > 110°, as shown in Figure 5.9b. On the dayside, when the terrestrial signal is very high, a minimal increase of ~1.8 counts at SZA < 40° was observed. Typical Earth view signals are greater than 2000 counts Range 3 at these wavelengths and solar zenith angles, so that the magnitude of the contamination is less than 10^{-6} .

5.5. Range 3 Cathode Data

The first day of NOAA-18 SBUV/2 operations following the high voltage turn-on on June 3 (day 154) used Range 3 cathode output mode with the calibration lamp door closed. Range 1 and Range 2 offset values measured during this test are consistent with the results derived in Section 5.3 during Range 3 anode measurements. Figure 5.10 shows the Range 3 cathode mode offset values for all channels derived from night side data. All channels have approximately the same noise level (5.0 counts standard deviation). Typical channel-to-channel variations are approximately 0.1 counts. There is no evidence of regular patterns in timing or spectral location, such as the regular 8-second variation observed in NOAA-16 Range 3 cathode data. Since channel-to-channel fluctuations are within the statistical uncertainty, an average of all 12 channels to create the Range 3 cathode offset value is recommended. This value is also listed in Table 5.1. Later Range 3 cathode measurements include full day tests on June 8 and July 5, and four orbits once per week beginning September 8. Analysis of these data indicates no significant change during the first four months of operation, as shown in Figure 5.11.

TABLE 5.1
Electronic Offset Values in Discrete Mode

<i>Range</i>	<i>Inflight (A&E)</i>	<i>Prelaunch</i>
1	114.28 (±0.20)	113.41(±1.61)
2	63.94 (±0.01)	63.93(±0.11)
3 (<i>anode</i>)	63.90 (±0.01)	63.87(±0.27)
3 (<i>cathode</i>)	63.95 (±0.03)	63.79(±0.49)
CCR	63.92 (±0.00)	63.93(±0.09)

* All values are in counts. Uncertainties for inflight data represent standard error values.

TABLE 5.2
Electronic Offset Values in Sweep Mode

$$X_{\text{sweep}} = (X_{\text{discrete}} - X_{\text{nominal}})/12.5 + X_{\text{nominal}}$$

<i>Range</i>	X_{nominal}
1	113.41
2	64
3 (<i>anode</i>)	64
3 (<i>cathode</i>)	64

NOAA-18 SBUV/2 Range-1 Offset (Around New Moon Days 212-251,2005)

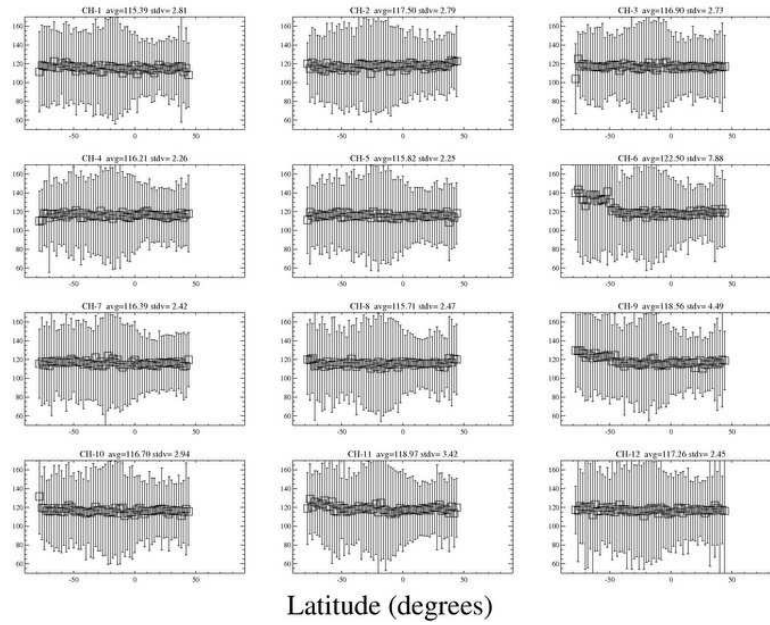


Figure 5.1: Range 1 offset: Latitude dependence.

NOAA-18 SBUV/2 Range-1 Offset (Around New Moon Days 212-251,2005)

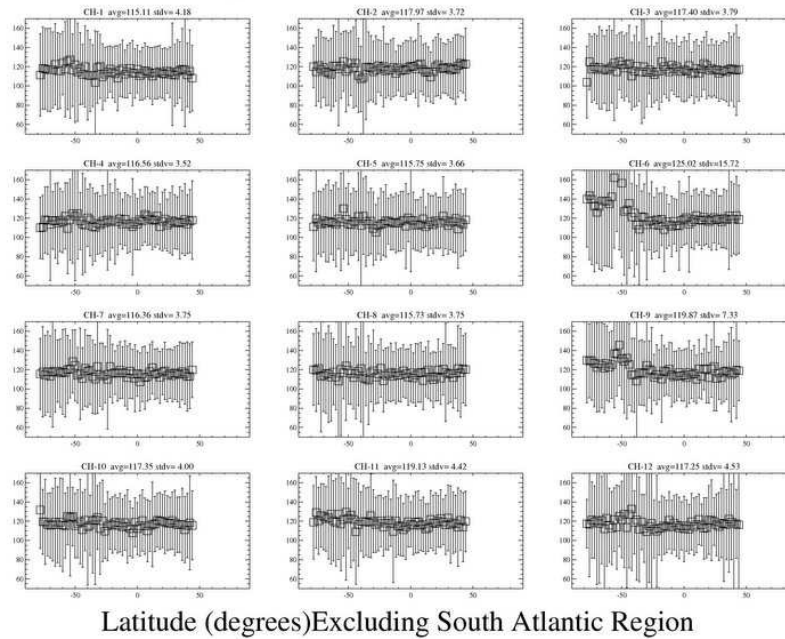


Figure 5.2: Range 1 offset: Latitude dependence (excluding South Atlantic Anomaly).

NOAA-18 SBUV/2 DAILY MEAN RANGE-1 ELECTRONIC OFFSET (SZA > 120)
 Data Coverage: JUN 1, 2005 - SEP 30, 2005; Lat=[-90,+90], Lon=[-180,+180]

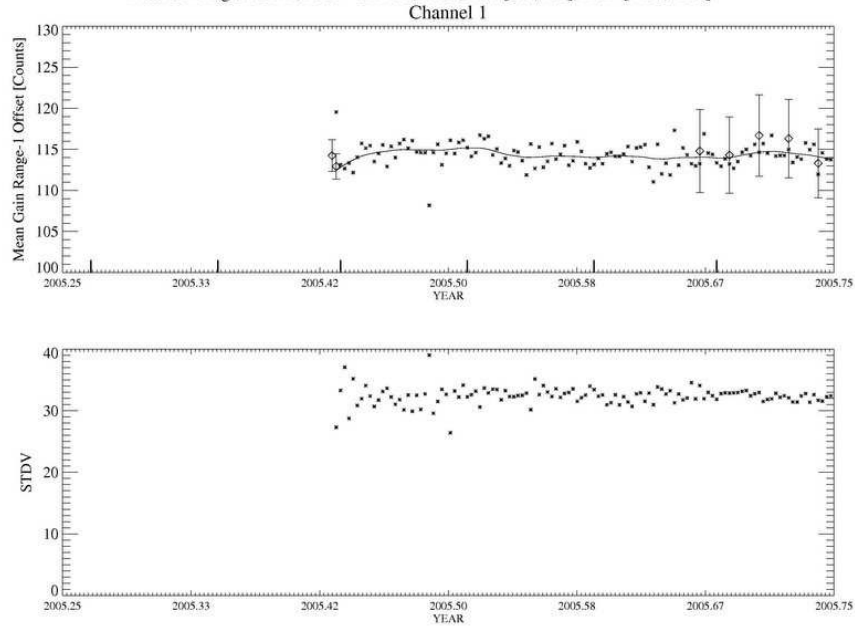


Figure 5.3: Range 1 offset data at 252 nm: (a) Daily average; (b) Standard deviation.

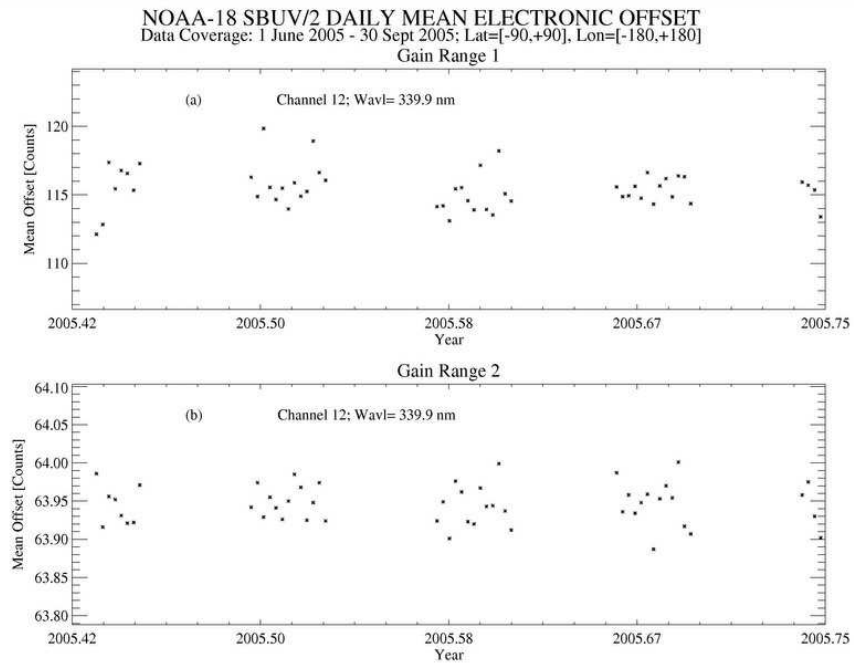


Figure 5.4: (a) Daily average Range 1 offset data (new moon dates); (b) Daily average Range 2 offset data (new moon dates).

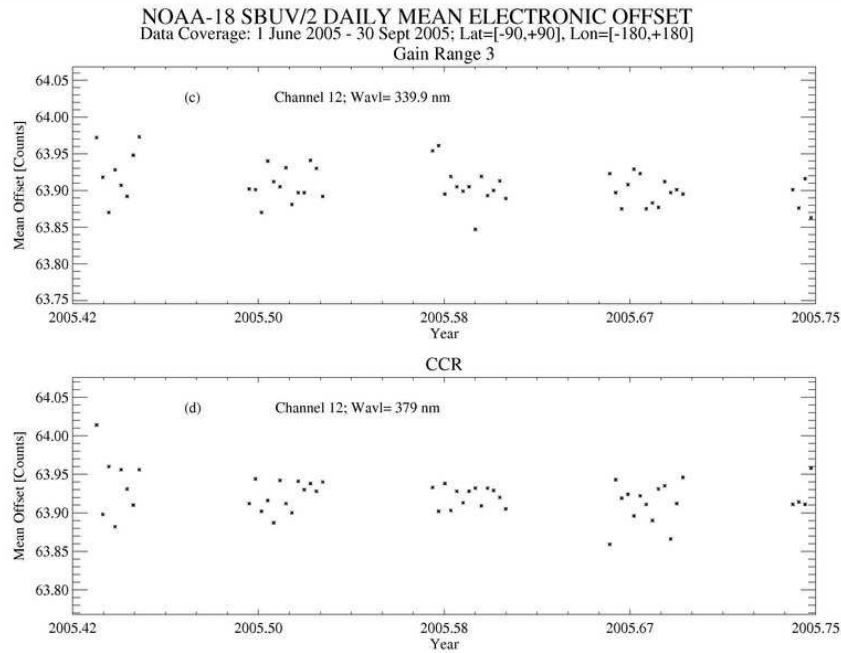


Figure 5.4: (c) Daily average Range 3 anode offset data (new moon dates); (d) Daily average CCR offset data (new moon dates).

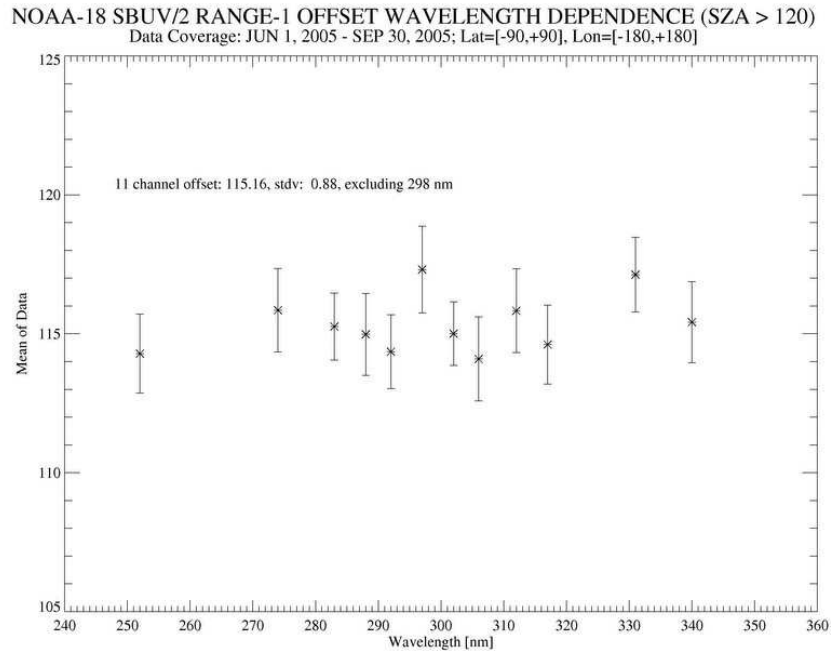


Figure 5.5: Spectral dependence of Range 1 offset, June-September 2005.

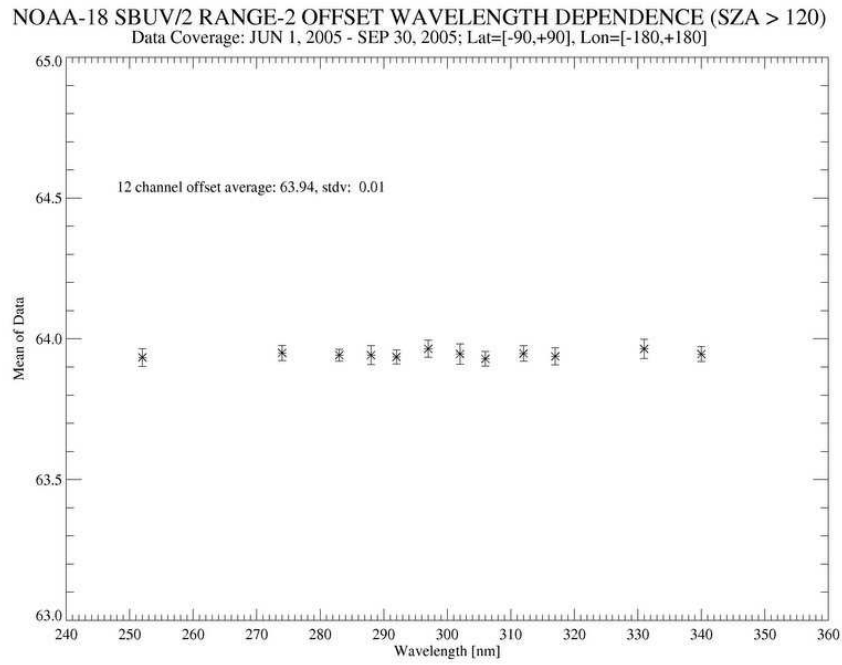


Figure 5.6: Spectral dependence of Range 2 offset, June-September 2005.

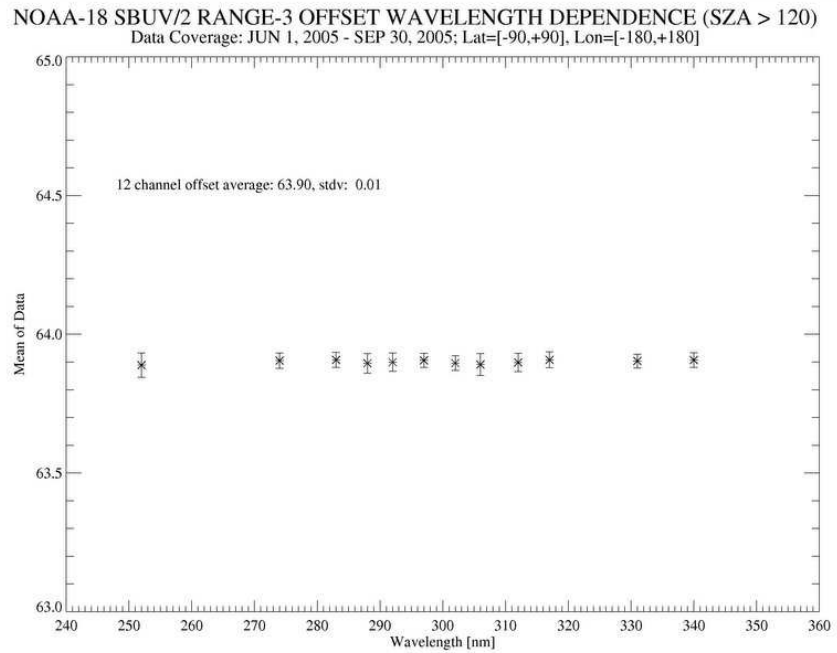


Figure 5.7: Spectral dependence of Range 3 anode offset, June-September 2005.

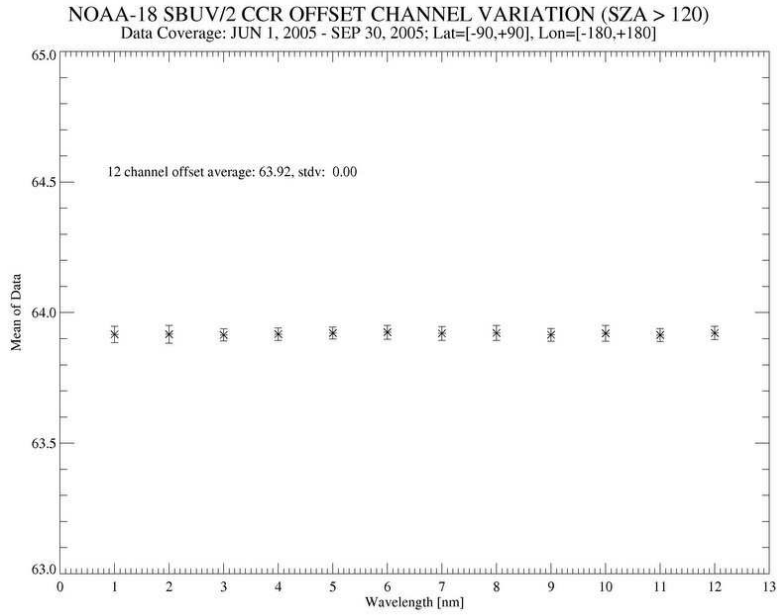


Figure 5.8: Spectral dependence of CCR offset, June-September 2005.

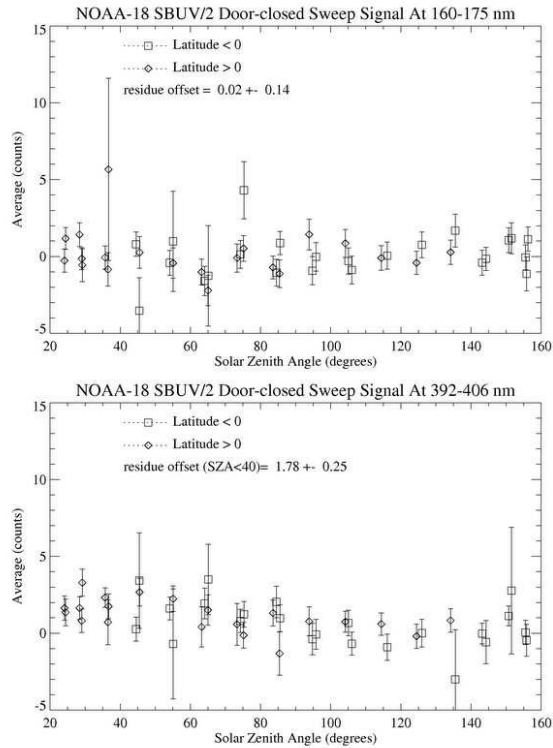


Figure 5.9: Sweep mode Range 1 offset vs. solar zenith angle for 2005 day 190: (top) 392-406 nm; (bottom) 160-175 nm.

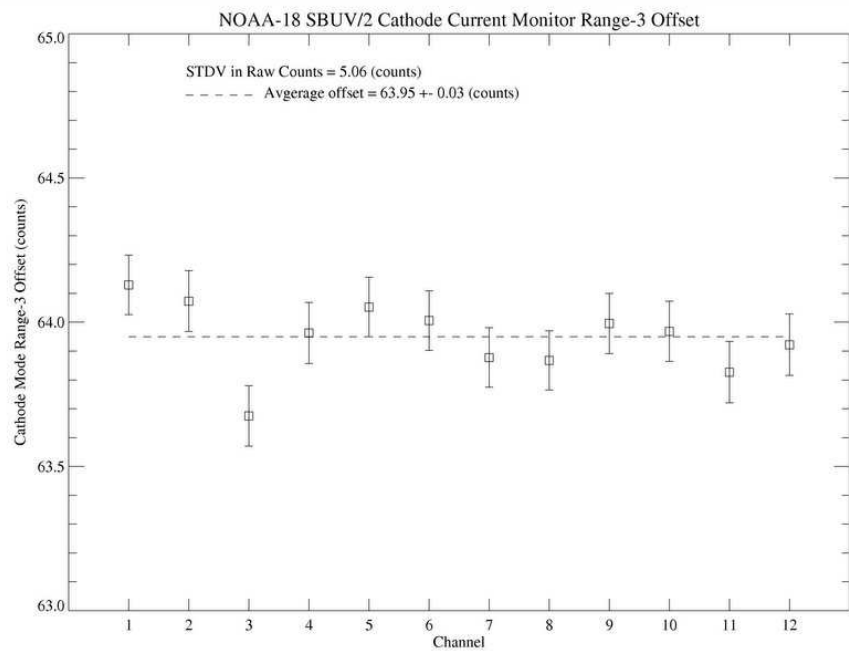


Figure 5.10: Spectral dependence of Range 3 cathode offset, 2002 days 241-242.

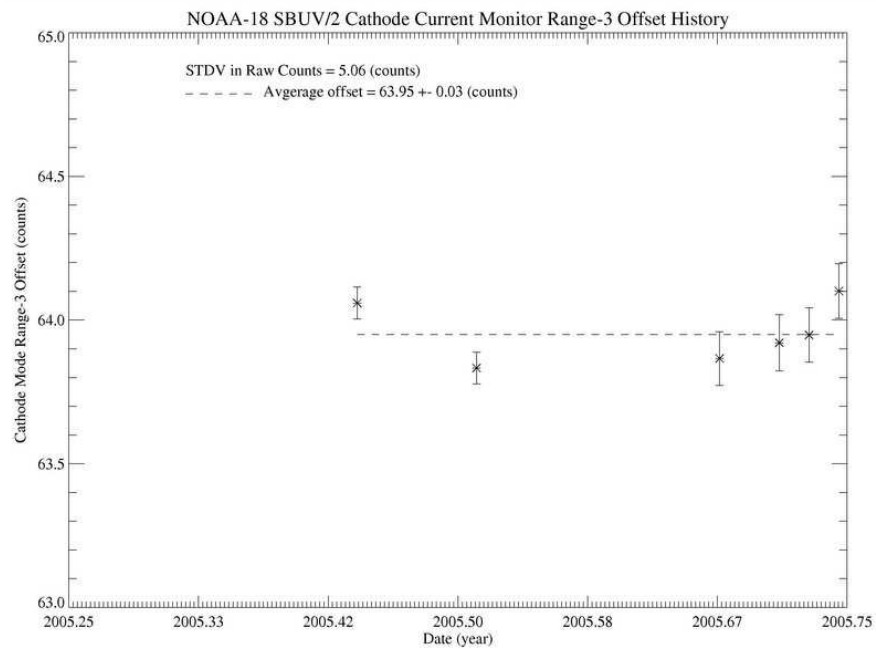


Figure 5.11: Time series of Range 3 cathode offset data.

6. Wavelength Calibration

The prelaunch wavelength calibrations were performed at Ball Aerospace in November 1995 with four hollow cathode discharge tubes (Pt-Ne, Zn-Ne, Mg-Ne and Cr-Cu-Ne) and a low pressure mercury arc lamp. An integration sphere, illuminated by each lamp, provided a depolarized uniform spectral source. A reliable wavelength calibration must be performed with narrow spectral lines that are well understood and with uniform coverage of the full spectral range. A total of 10 spectral lines, 7 from the hollow cathode discharge tubes and 3 from the mercury lamp, were used to derive the wavelength calibration. The SBUV/2 instrument also has an on-board wavelength calibration system to monitor the wavelength stability, which uses a mercury lamp. The on-board system is generally considered to provide less usable spectral lines and less uniform illumination than the laboratory system. Because of the variety and stability of the spectral sources in the laboratory, we would expect the prelaunch wavelength calibration to be more reliable than the on-board wavelength calibration. The relationship between instrument grating position and wavelength is defined by Equation 6.1, where A_0 , A_1 , and A_2 represent the Ebert coefficients.

$$\lambda = A_0 * \sin(A_1*(A_2+GPOS)) \quad [6.1]$$

There were 113 wavelength calibration measurements taken with the primary encoder during the 8 years before launch that can be used to evaluate the stability of the FM#7 wavelength scale. Most of these measurements were taken during the course of other calibration tests, and therefore only the major Hg emission lines at 185.0, 253.7, and 404.7 nm were tracked. The most significant early event was a shift of approximately -1 step during initial vibration tests in August 1996 (Figure 4.2-7, Vol. 2 [Data Book]). Subsequent shifts are typically $< \pm 0.5$ step, and there is also a variation between test fixtures. During radiometric calibration tests in 2003, the observed shift in line positions was approximately -1.4 steps. Ball Aerospace incorporated this change by revising the value of the A_2 Ebert coefficient ($\Delta A_2 = +1.4$ steps). Since this was the last wavelength calibration measurement prior to launch, these modified Ebert coefficients were recommended for NOAA-18 SBUV/2 initial on-orbit operations by *DeLand et al.* [2005]. Sections 6.1-6.4 discuss inflight measurements used to evaluate this calibration.

6.1. Sweep Mode

Extensive onboard wavelength calibrations in sweep mode were performed during the first four months in orbit. The sweep mode wavelength calibration sequence performs 10 scans over the wavelength range 160-406 nm. The first 4 scans are in diffuser view, followed by 2 scans in lamp view, 2 scans in diffuser view and 2 scans in lamp view (see Figure 11.2). Sweep mode signal levels from diffuser view measurements are 2 orders of magnitude weaker in intensity than from lamp view measurements. The Hg lamp is warming up and stabilizing during scans 1-4, and scan 10 is occasionally contaminated by backscattered light near the terminator, so scans 5-9 are typically used for wavelength calibration. In sweep mode, each data sample represents two consecutive steps of the grating drive, so that the average grating position during signal integration is approximately 0.5 steps less than the grating position at the end of the signal integra-

tion (when discrete mode grating position values are obtained). Thus, we expect the sweep mode wavelength calibration to be shifted by 0.5 steps (GPOS) in comparison with discrete mode measurements for the same wavelength. In addition, sweep mode grating position values are recorded only for every tenth sample, requiring interpolation to assign GPOS values to intervening samples. As noted in Section 4, no grating drive errors have been observed for NOAA-18 SBUV/2.

All data were processed with the corrections derived in this report for offset, thermal drift, nonlinearity and gain ratios, and converted to equivalent Range 3 counts. Figure 6.1 shows an example of the observed sweep mode line profile at 185.0 nm. The centroid of the line profile is defined as the intensity-weighted average grating position over 16 or 17 samples around the peak, depending on how the line is centered with respect to the sampled grating positions. In the prelaunch analysis, the sample with maximum intensity was defined as the center of the line profile and 15 points around the center were taken for the average. When we simulated the prelaunch calculation algorithm using inflight data, the results of the two algorithms agreed to better than 0.05 GPOS. Even though the grating position with the intensity maximum in a spectral scan is often not the center of the line profile, the bias in the centroid calculation can be negligibly small as long as the background is negligible relative to the line peak intensity and the full line profile (32 or more grating steps) is covered for the average. We also determined line center positions using linear regression fits to 4 data points on each side of the profile. Two or three points near the peak are excluded from the fitting since they deviate from an ideal triangle model.

The centroids of the primary Hg lamp lines were very stable during the first four months of inflight measurements. Figures 6.2-6.4 show time history plots of the sweep mode line center positions from lamp view measurements derived using the centroid method (×) and linear regression method (□). The linear regression is more sensitive to noise during the line profile scan, which resulted in an 0.2 step increase in peak position for the 185 nm line in September 2005 (Figure 6.2). Note that the brighter lines at 253.7 and 404.8 nm (Figures 6.3, 6.4) do not show this change. Table 6.1 lists the differences between the centroid and regression peak positions for the six strongest emission lines. The results calculated with the two methods typically agree to within ± 0.1 steps. Since there is no noticeable drift, averages of all measurements will be used for the wavelength calibration in orbit.

The sweep mode centroid values from prelaunch tests in November 1995 (corrected for air-to-vacuum wavelength changes) and the reference wavelength calibration values are also shown in Figures 6.2-6.4. We identified an error in Table 4.1-2, Vol. 2 [[Data Book](#)]. The average centroids in laboratory tests 12-19 in July 1996 were computed and compared with the values listed in Table 4.1-2. We found a difference of -2.560 steps for the 184.9 nm line, compared to much smaller differences of -0.277 steps for the 253.7 nm line and -0.269 steps for the 404.8 nm line. Therefore, we revised the reference value at 184.9 nm using the average centroid from tests 12-19, with a correction of -0.272 steps for drift and differences in the spectral sources. The results of this comparison yielded a shift of $+0.82(\pm 0.08)$ steps for centroids derived from on-orbit data relative to the recommended prelaunch wavelength calibration.

6.2. 4-step Discrete Mode

At the end of each sweep mode wavelength calibration sequence, a series of lamp view discrete mode scans over the 253.7 nm line are executed, with the grating drive moving 4 steps between samples. Figure 6.5 shows an example of the spectral line profiles measured on September 7, 2005. The centroid was calculated as the intensity-weighted average grating position using 11 samples around the peak from GPOS = 443 to GPOS = 483. Inclusion of the sample at GPOS = 439 would shift the calculated centroid by $\Delta\text{GPOS} = -0.03$. The peak position also can be characterized by fitting two straight lines to 3 data points on each side of the peak, respectively. The peak grating position derived using this method is only about 0.01 GPOS smaller than the centroid calculation result.

Figure 6.6 shows a time series of the 4-step discrete mode measurement results during the first four months in orbit. The error bar in each measurement is the standard deviation of 9 scans, which is substantially smaller than the day-to-day variations. A small dip of -0.2 steps on June 20, 2005, was correlated with the accidental shutdown of the calibration lamp heater. Excluding this point on June 20 and the day after, the day-to-day variation is less than 0.02 GPOS. Thus, the wavelength scale is very stable during the first four months.

6.3. 2-step Discrete Mode

The mercury lamp spectral lines listed in Table 6.1 were also measured in the 2-step discrete mode for wavelength calibration. Each calibration sequence had about 60 scans grouped in both lamp view and diffuser view. Each spectral line profile was scanned with a 2-step grating position increment and a total of 12 points around the peak. Details of the discrete calibration sequence are illustrated in Figure 11.7. About 20 scans were selected from each viewing condition after the lamp warmup period.

The spectral coverage of the 2-step discrete scans is not sufficient to use the intensity-weighted method to calculate the line center position. Therefore, the line peak position is estimated using two straight lines fitted respectively to 4 data points on the 2 sides of the line profile. Figure 6.7 show an example of the measured spectral line profiles. As with the sweep mode analysis, the centermost samples are excluded from the regression fits. The third column of Table 6.2 lists the derived centroids that are equal to the fitted peak positions plus the difference between the centroid and the fitted peak position in the sweep mode.

The second column of Table 6.2 lists prelaunch centroid values from position mode data taken in November 1995, adjusted for the 2003 calibration shift ($\Delta A_2 = +1.4$ steps) and air-to-vacuum wavelength differences. The average centroid shift for the on-orbit measurements is $+0.94(\pm 0.12)$ steps, consistent with the sweep mode results from Section 6.1. We therefore recommend a further wavelength calibration adjustment of $\Delta A_2 = -0.9$ steps for NOAA-18 inflight operations. The revised Ebert coefficients for discrete and sweep mode measurements are listed in Table 6.3. The exact wavelengths calculated from these coefficients for ozone, Mg II solar, and Mg II OOB measurements are listed in Table 6.4.

6.4. Validation of Inflight Ebert Coefficients

The orbital measurements of the onboard Hg lamp spectral lines can also be used to derive the wavelength calibration. The centroids in both sweep and discrete modes are separately fit using the following equation, which is inverted from Equation 6.1:

$$GPOS = \arcsin(\lambda/a_0)/a_1 - a_2 \quad [6.2]$$

A nonlinear regression procedure, CURVEFIT in the IDL program library, is used for calculation of the line center grating position. Each centroid or the peak position of the six mercury lines is weighted according to its standard deviation.

In order to evaluate the collective effect of the differences between Ebert coefficient values, we calculated reference wavelengths for all four sets of coefficients (discrete and sweep, prelaunch and inflight), using the line center positions observed during inflight wavelength calibrations. The prelaunch Ebert coefficients in November 1995 were adjusted by a net change of $\Delta A_2 = +0.5$ steps to reflect inflight results. Figure 6.8 shows differences between the calculated and reference wavelengths for sweep mode coefficients. Most residual differences are ± 0.02 nm or less, corresponding to a grating position offset of 0.28 steps. The largest residual is 0.055 nm (= -0.72 steps) for the 185 nm line with the adjusted prelaunch Ebert coefficients. If this value is excluded, the average residual based on the adjusted prelaunch coefficients is 0.007 nm. Discrete mode results are shown in Figure 6.9, and are very similar to the sweep mode results. The largest residual value is +0.023 nm at the 185 nm line, and the average residual value excluding this case is only -0.006 nm.

6.5. Wavelength Scale Comparison Between Lamp View and Diffuser View

We examined any differences in the wavelength calibration between lamp view and diffuser view data. The Hg lamp centroids derived from these operational modes are listed in Table 6.5 and Table 6.6. Most of the results are in excellent agreement. The maximum observed differences are -0.17 steps at 185.0 nm in sweep mode, and +0.24 steps at 253.7 nm in discrete mode. We do not make any wavelength calibration correction for the choice of mercury lamp position.

6.6. Instrument Bandpass

The width of the instrument slit function is required in the SBUV/2 forward model calculation for ozone processing. Slit function widths are determined for each spectral line during the prelaunch wavelength calibration. The full width of the bandpass at half maximum intensity (FWHM) is derived from linear interpolation of measurements. Table 6.7 lists the results as reported in Table 4.1-7, Vol. 2 [Data Book], which were used to calculate a prelaunch bandpass value in *DeLand et al.* [2005]. We derived the slit function width from inflight sweep mode data for the Hg lamp lines, and obtained the results listed in Table 6.8. The wings of the line profile were interpolated and subtracted from the line profile. In the FWHM calculation, the peak intensity is defined as the maximum of the cubic spline interpolated profile, and the half maximum is

then determined from fitted straight lines on each side of the spectral line profile. Also listed in the same table are the bottom widths of fitted triangles. The FWHM values in lamp view, which have better signal-to-noise ratios than in diffuser view, show a monotonic decrease as wavelength increases. The on-orbit bandpass values in Table 6.8 are larger than the prelaunch values at 185.0, 253.7 and 404.7 nm with the same set of Hg lamp lines. It is possible that the optical alignment changed slightly since the reference measurements in 1995. The differences may also come from analysis method differences in defining the spectral background and peak and other calibration issues. At other middle range wavelengths, the prelaunch FWHM values which used the hollow cathode discharge lamps are considerably larger than the inflight data. We recommend using the average of inflight lamp view FWHM values (= 1.133 nm) for NOAA-18 SBUV/2 operational ozone processing.

TABLE 6.1
Sweep Mode Hg Lamp Line Centers: Inflight

<i>Wavelength</i> [nm]	<i>Line Position*</i> Prelaunch [centroid]	<i>Line Position</i> Inflight [centroid]	<i>Difference</i> inflt.-pre. [centroid]	<i>Line Position</i> Inflight [regression]	<i>Difference</i> Inflight [cent. – reg.]
184.950	1371.41	1372.16	0.75	1372.22	-0.06
253.733	463.16	464.07	0.91	464.03	0.04
289.449	—	-17.92	—	-17.99	0.07
296.819	—	-118.25	—	-118.36	0.12
334.249	—	-634.35	—	-634.46	0.11
404.776	-1640.98	-1640.17	0.81	-1639.95	-0.22

* The centroids are based on the recommended prelaunch wavelength calibration, where the centroids determined in the November 1995 reference calibration are shifted by -1.4 steps, then corrected for vacuum wavelength shifts.

TABLE 6.2
2-step Discrete Mode Hg Lamp Line Centers: Inflight

<i>Wavelength</i> [nm]	<i>Line Position*</i> [prelaunch, centroid]	<i>Line Position**</i> [inflight, centroid]	<i>Difference</i> [inflt. – pre.]
184.95	1370.85	1371.699	0.85
253.73	462.57	463.649	1.08
289.44	—	-18.195	—
296.81	—	-118.544	—
334.24	—	-634.636	—
404.77	-1641.64	-1640.734	0.90

* The centroids are based on the recommended prelaunch wavelength calibration, where the centroids determined in the November 1995 reference calibration are shifted by -1.4 steps, then corrected for vacuum wavelength shifts.

** The inflight centroid is equal to the peak position corrected for the difference between centroid and peak position in sweep mode.

TABLE 6.3
Ebert Coefficients for Wavelength Calibration

<i>Coefficient</i>	<i>Prelaunch</i>		<i>Inflight</i>	
	<i>Discrete</i>	<i>Sweep</i>	<i>Discrete</i>	<i>Sweep</i>
A ₀	820.067	820.067	820.067	820.067
A ₁	-9.583708×10 ⁻⁵	-9.582718×10 ⁻⁵	-9.583708×10⁻⁵	-9.582718×10⁻⁵
A ₂	-3744.76	-3745.73	-3745.66	-3746.63

TABLE 6.4
Recommended Operational and Test Grating Positions and Wavelengths

<i>Channel</i>	<i>OZONE Grating Position</i>	<i>Calculated Wavelength [nm]</i>	<i>Mg II Solar Grating Position</i>	<i>Calculated Wavelength [nm]</i>	<i>Mg II OOBR Grating Position</i>	<i>Calculated Wavelength [nm]</i>
1	486	252.039	152	276.885	150	277.033
2	195	273.702	150	277.033	110	279.990
3	67	283.164	134	278.217	68	283.090
4	5	287.732	126	278.808	150	277.033
5	-58	292.364	112	279.842	110	279.990
6	-130	297.643	110	279.990	68	283.090
7	-190	302.032	108	280.138	150	277.033
8	-243	305.901	98	280.876	110	279.990
9	-336	312.671	92	281.319	68	283.090
10	-404	317.604	84	281.910	150	277.033
11	-594	331.318	68	283.090	110	279.990
12	-714	339.923	66	283.238	68	283.090
CCR	—	378.62	—	378.62	—	378.62

TABLE 6.5
Lamp View vs. Diffuser View: Discrete Mode

<i>Reference Wavelength [nm]</i>	<i>Lamp View Peak</i>	<i>Diffuser View Peak</i>	<i>Difference [steps]</i>
184.950	1371.76(± 0.01)	1371.61(± 0.02)	-0.15(± 0.02)
253.728	463.61(± 0.01)	463.85(± 0.02)	0.24(± 0.02)
289.444	-18.27(± 0.02)	-18.19(± 0.23)	0.08(± 0.23)
296.814	-118.65(± 0.01)	-118.60(± 0.03)	0.05(± 0.03)
334.244	-634.75(± 0.02)	-634.6(± 0.14)	0.10(± 0.14)
404.770	-1640.51(± 0.02)	-1640.64(± 0.02)	-0.13(± 0.03)

TABLE 6.6
Lamp View vs. Diffuser View: Sweep Mode

<i>Reference Wavelength [nm]</i>	<i>Lamp View Centroids</i>	<i>Diffuser View Centroids</i>	<i>Difference [steps]</i>
184.950	1372.16(± 0.05)	1371.99(± 0.06)	-0.17(± 0.08)
253.728	464.07(± 0.04)	463.96(± 0.04)	-0.11(± 0.06)
289.444	-17.92(± 0.04)	-18.06(± 0.8)	-0.14(± 0.80)
296.814	-118.25(± 0.05)	-118.2(± 0.05)	0.05(± 0.07)
334.244	-634.35(± 0.05)	-634.24(± 0.31)	0.11(± 0.31)
404.770	-1640.17(± 0.04)	-1640.14(± 0.05)	0.03(± 0.06)

TABLE 6.7
Spectral Resolution in Discrete Mode
Based on Prelaunch Wavelength Calibration

<i>Wavelength</i> [nm]	<i>FWHM</i> [nm]
184.900	1.14
253.666	1.04
285.228	1.18
299.812	1.17
306.487	1.16
307.606	1.24
324.771	1.15
327.413	1.15
404.676	1.09
<i>average</i>	1.147(\pm 0.056)

TABLE 6.8
Spectral Resolution in Sweep Mode Based on A&E Tests

<i>Wavelength</i> [nm]	<i>Lamp View</i>		<i>Diffuser View</i>	
	<i>Triangle</i> [nm]	<i>FWHM</i> [nm]	<i>Triangle</i> [nm]	<i>FWHM</i> [nm]
184.950	2.1852(\pm 0.0088)	1.1844(\pm 0.0041)	2.1833(\pm 0.0066)	1.1755(\pm 0.0035)
253.733	2.1401(\pm 0.0014)	1.1422(\pm 0.0047)	2.1715(\pm 0.0081)	1.1474(\pm 0.0056)
289.444	2.1183(\pm 0.0062)	1.1212(\pm 0.0054)	2.1818(\pm 0.0830)	1.0917(\pm 0.0369)
296.814	2.1264(\pm 0.0019)	1.1185(\pm 0.0017)	2.1256(\pm 0.0086)	1.1202(\pm 0.0056)
334.244	2.1045(\pm 0.0043)	1.1187(\pm 0.0029)	2.2324(\pm 0.4451)	1.1123(\pm 0.0559)
404.776	2.0534(\pm 0.0045)	1.1125(\pm 0.0037)	2.0483(\pm 0.0058)	1.1134(\pm 0.0029)
Average	2.1264(\pm 0.0433)	1.1329 (\pm 0.0272)	2.1571(\pm 0.0632)	1.1267(\pm 0.0299)

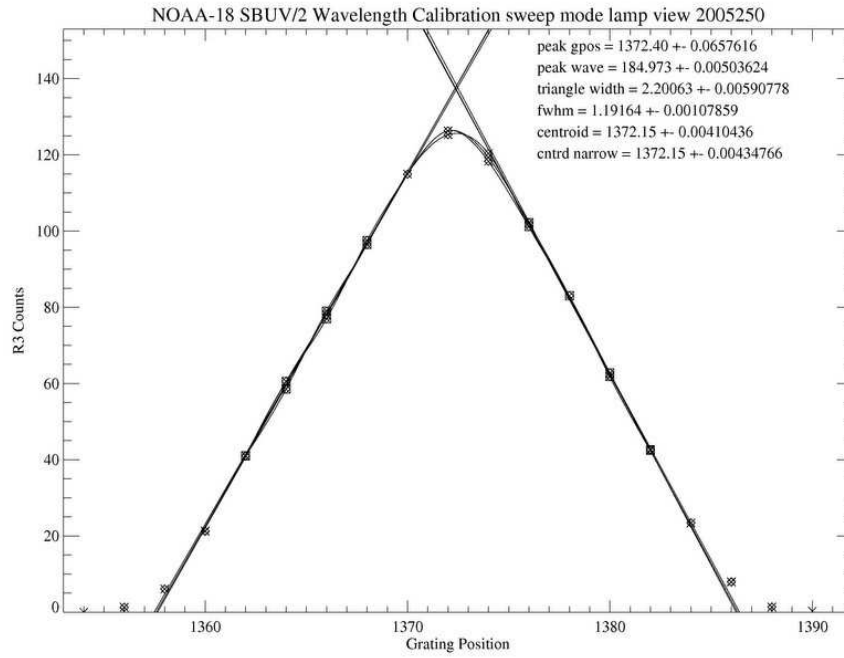


Figure 6.1: Mercury lamp sweep mode line profile at 185.0 nm.

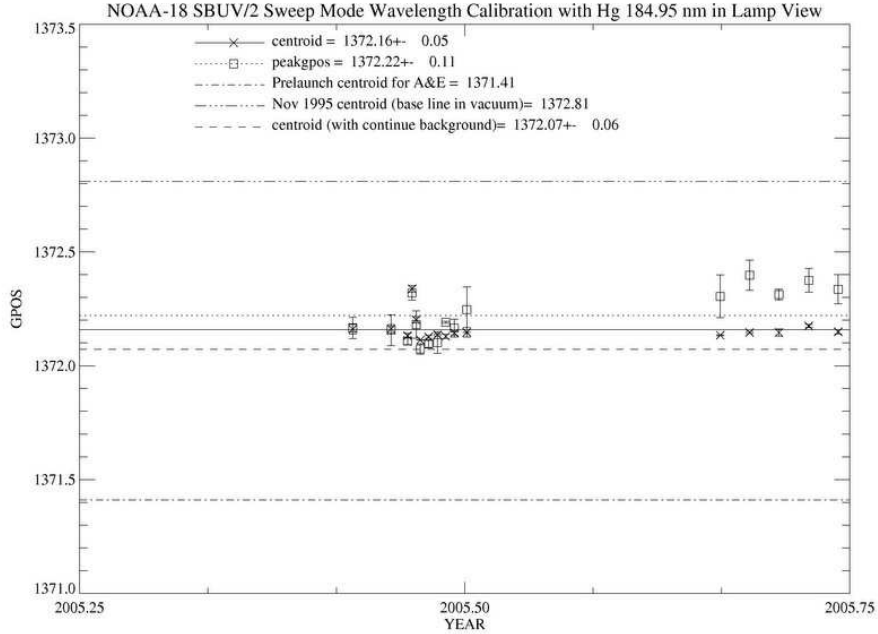


Figure 6.2: Sweep mode line center time dependence at 185.0 nm.

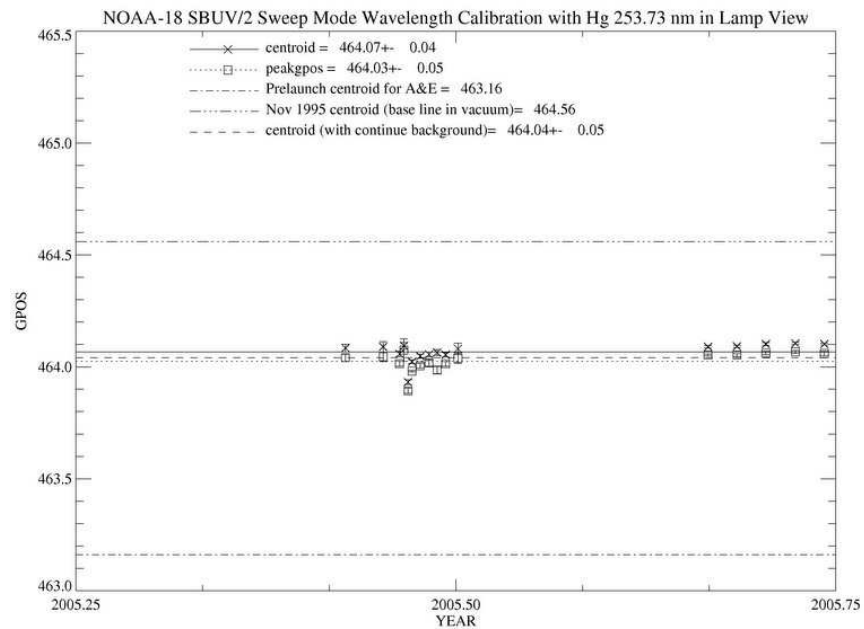


Figure 6.3: Sweep mode line center time dependence at 253.7 nm.

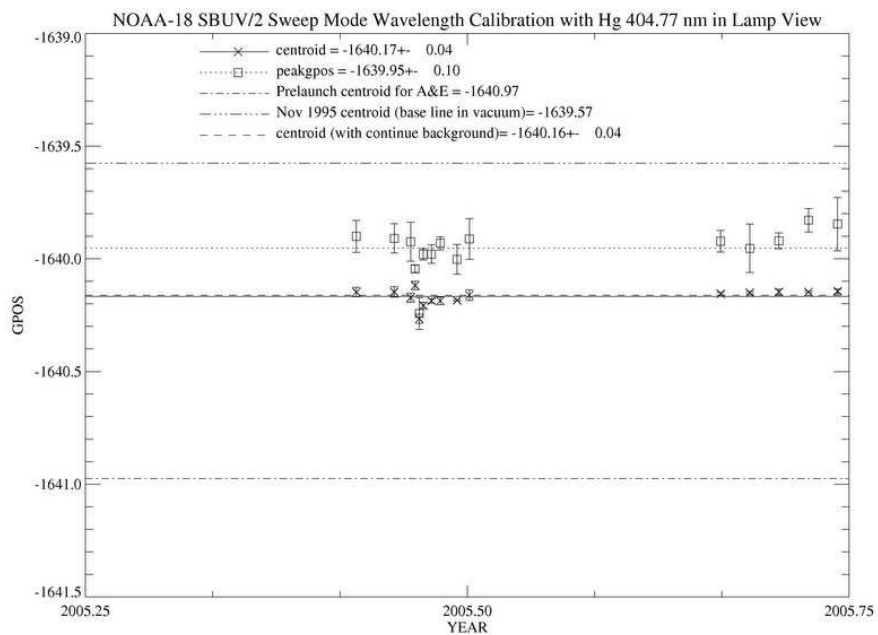


Figure 6.4: Sweep mode line center time dependence at 404.8 nm.

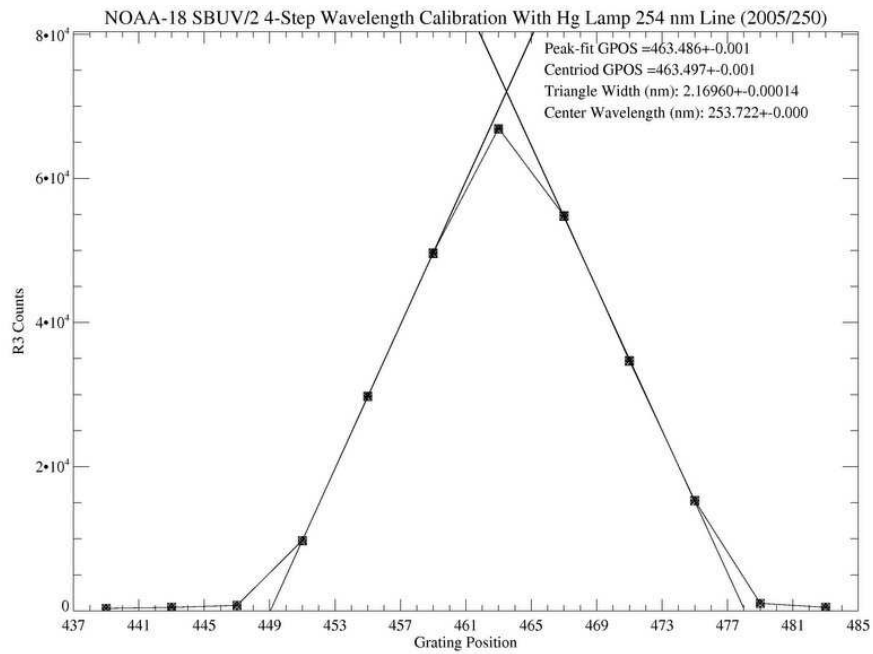


Figure 6.5: Discrete mode line profile at 253.7 nm (4-step sampling).

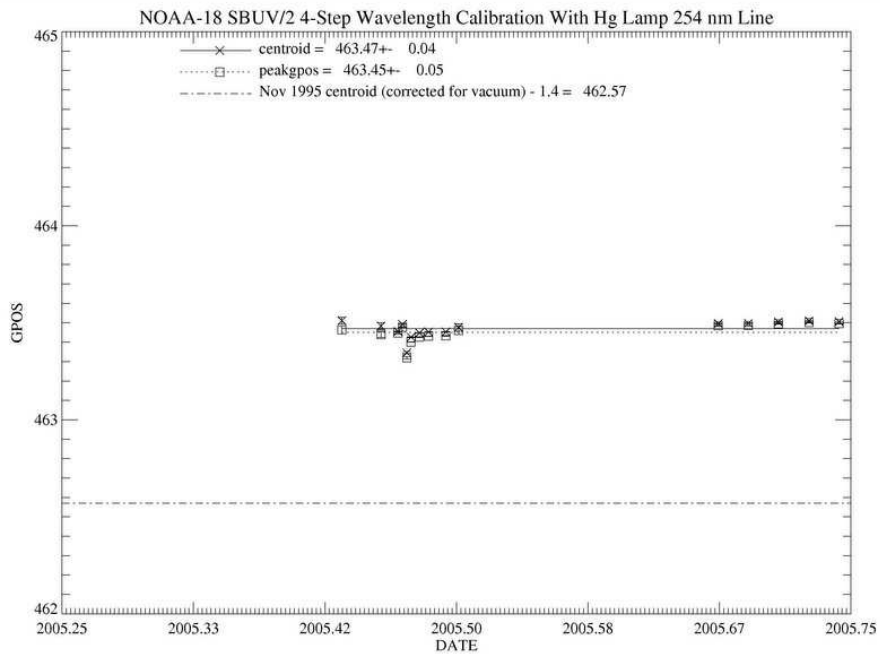


Figure 6.6: Discrete mode (4-step sampling) line center time dependence at 253.7 nm.

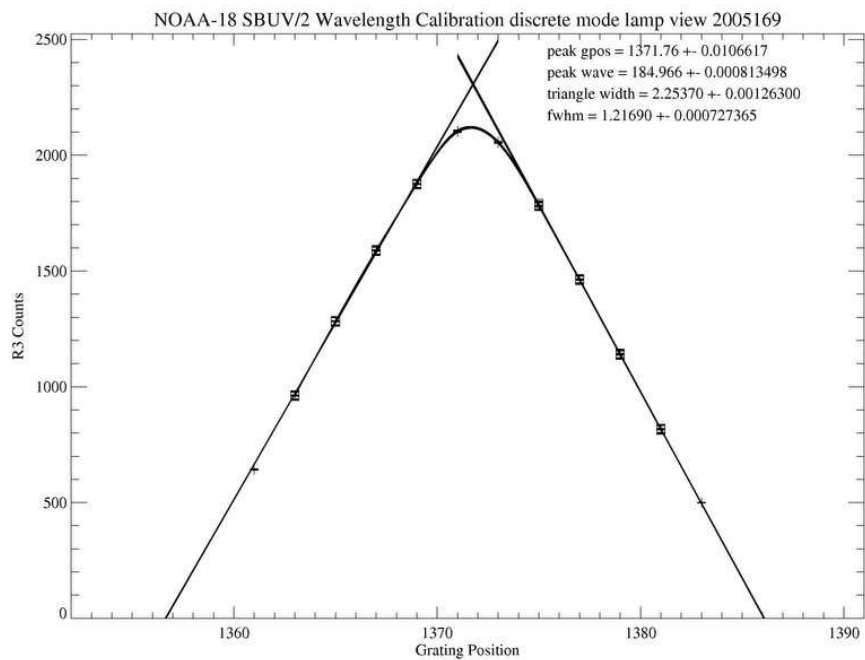


Figure 6.7: Discrete mode line profile at 185.0 nm (2-step sampling).

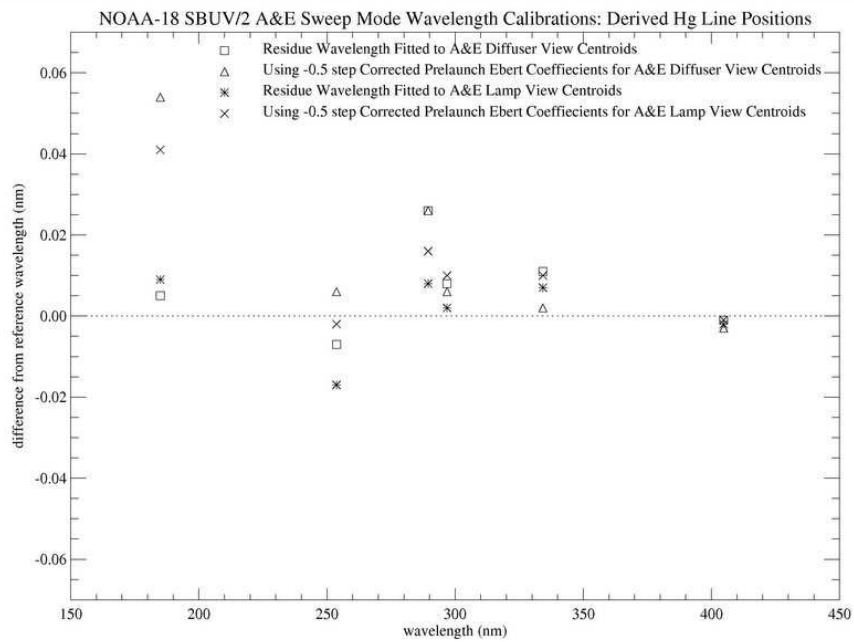


Figure 6.8: Calculated Hg line positions: Sweep mode Ebert coefficients.

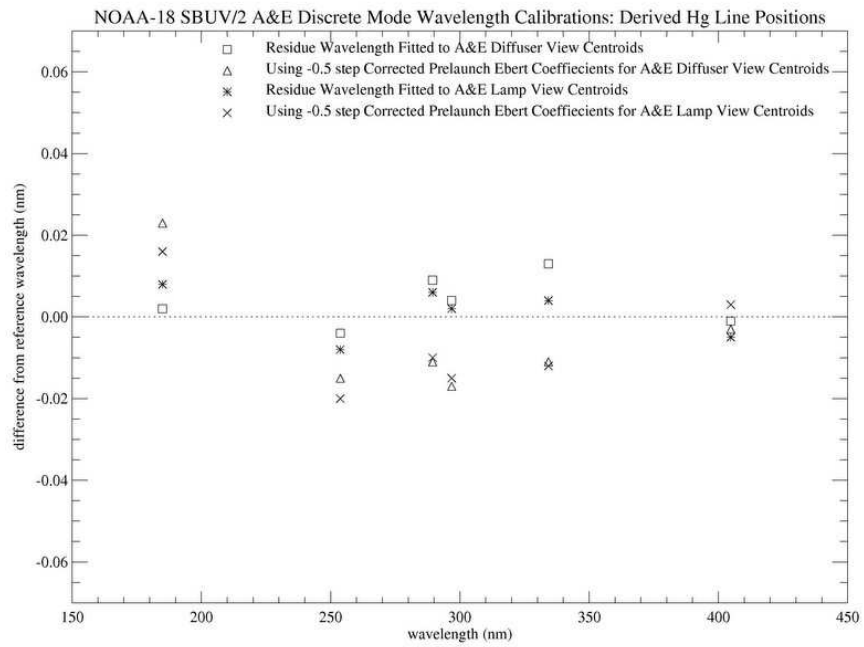


Figure 6.9: Calculated Hg line positions: Discrete mode Ebert coefficients.

7. Goniometric Calibration

7.1. Prelaunch Characterization

The SBUV/2 instrument views the Sun using a reflecting diffuser plate to direct solar illumination into the nadir-viewing aperture and fill the field of view. Solar measurements are made at high incidence angles on the diffuser ($\theta \approx 55\text{-}80^\circ$). The diffuser has an approximately Lambertian ($\cos\theta$) response, so that the observed signal from a constant source varies by a factor of 2.0-3.0 during a typical inflight measurement sequence. Ball Aerospace performs prelaunch laboratory calibrations to characterize this goniometric response as a function of elevation angle [α] and azimuth angle [β]. Data are taken on a regular grid ($\Delta\alpha = 2^\circ$, $\Delta\beta = 5^\circ$), then normalized to a reference orientation of $\alpha = 0^\circ$, $\beta_{\text{inst}} = 34^\circ$. These values are chosen because they are the closest measurement positions to the angles used for radiometric calibration measurements. Goniometric measurements are made at two wavelengths (254, 405 nm) using a mercury lamp, and at four wavelengths (270, 300, 350, 406 nm) using a FEL lamp. An example of the raw FEL data at 350 nm is shown in Figure 7.1, where the data are expressed as the inverse of the measured response to illustrate the correction needed for solar irradiance processing. A $\cos\theta$ variation was removed before plotting the data. The measurement angles have been converted to spacecraft-centered coordinates for convenience, where $\beta_{\text{S/C}} = \beta_{\text{inst}} + \beta_{\text{ref}}$, and $\beta_{\text{ref}} = 26.04^\circ$. DeLand *et al.* [2005] presented the derivation of the prelaunch goniometric correction function $G_{\text{fit}}(\alpha, \beta)$ for the FM#7 instrument. The coefficients for this fit are listed in Table 7.1.

7.2. On-Orbit Validation

On-orbit measurements showed a residual elevation-dependent error after applying the prelaunch goniometric correction, reaching a magnitude of -1% at $\alpha = 20^\circ$. An example of this error is shown in Figure 7.2 (*middle panel*). A linear correction function was derived by fitting the CCR data from all position solar tests (see Section 7.3) and averaging the fit coefficients (Equation 7.5). The correction coefficients for operational data are listed in Table 7.2. Because the A&E measurements only cover a short period of time, azimuth-dependent errors could not be evaluated yet. The NOAA-18 satellite is expected to have a stable orbit, with less than 30 minutes total drift in Equator-crossing time during the first 6 years of operations. Thus, refinements to the prelaunch goniometric correction should remain valid for many years to come.

7.3. Wavelength Dependence

Position mode solar irradiance measurements are taken over a wide range of wavelengths during A&E activities. Figure 7.3 shows the observed data at 339.9 nm, processed with the prelaunch goniometric correction and normalized at $\alpha = 1.5^\circ$. After applying the elevation-dependent correction of Equation 7.5 to all position mode data, a significant wavelength-dependent variation is observed. Figure 7.4 shows elevation angle-dependent drifts at $\alpha = 20^\circ$ of $+0.2\%$ at 400 nm (*triangle*), $+1.2$ at 299.9 nm (*asterisk*), $+2.5\%$ at 252.0 nm (*diamond*), and $+7\%$ at 195.0 nm (*cross*).

Because the position mode data are taken during a relatively short period of time, there is very little variation in azimuth angle among the measurements. We therefore derived a correction for goniometric wavelength dependence as a function of λ and incidence angle θ , where the incidence angle is calculated from the spacecraft-centered elevation and azimuth. For previous SBUV/2 instruments, the wavelength-dependent correction was parameterized with a Taylor series expansion in λ and θ . However, expansions up to 3rd order did not yield adequately small residuals when compared with the FM#7 data. We therefore calculated linear fits to the monochromator/CCR ratio at each position mode wavelength to characterize the incidence angle dependence, then fit the slope and Y-intercept coefficients with 4th order functions (Tables 7.3 and 7.4). These functions accurately track the individual values, as shown in Figures 7.5 and 7.6. The final form of the wavelength-dependent goniometric correction is given in Equation 7.6. The accuracy of the combined corrections is shown by the monochromator sweep scan ratio in the top panel of Figure 7.7, showing scan-to-scan differences less than 1% down to 170 nm.

TABLE 7.1
Standard Goniometry Fit Coefficients

<i>Coefficient</i>	<i>Term</i>	<i>Value</i>
C ₁	—	3.82539e+00
C ₂	α	-2.23533e-03
C ₃	β	-9.28729e-02
C ₄	α^2	1.40158e-04
C ₅	$\alpha\beta$	-5.34266e-04
C ₆	β^2	8.12729e-04
C ₇	α^3	-1.16810e-05
C ₈	$\alpha^2\beta$	-2.77685e-05
C ₉	$\alpha\beta^2$	2.04199e-05
C ₁₀	β^3	-1.67272e-06
C ₁₁	α^4	1.57725e-07
C ₁₂	$\alpha^3\beta$	1.36089e-08
C ₁₃	$\alpha^2\beta^2$	2.36358e-07
C ₁₄	$\alpha\beta^3$	-1.72822e-07
C ₁₅	β^4	1.48272e-08

TABLE 7.2
Goniometric Elevation Correction Coefficients

<i>Coefficient</i>	<i>Term</i>	<i>Value</i>
F ₁	—	1.0014E+00
F ₂	α	-6.889E-04

TABLE 7.3
Wavelength-Dependent Goniometric Correction: *Y-Intercept*

<i>Coefficient</i>	<i>Term</i>	<i>Value</i>
D ₁	—	1.0032E+00
D ₂	λ	-3.5201E-04
D ₃	λ^2	2.7830E-06
D ₄	λ^3	-7.6441E-09
D ₅	λ^4	7.0778E-12

TABLE 7.4
Wavelength-Dependent Goniometric Correction: *Slope*

<i>Coefficient</i>	<i>Term</i>	<i>Value</i>
E ₁	—	8.0942E-02
E ₂	λ	-9.3602E-04
E ₃	λ^2	4.1471E-06
E ₄	λ^3	-8.2442E-09
E ₅	λ^4	6.1627E-12

$$G_{\text{corr}}(\alpha, \beta, \theta, \lambda) = [G_{\text{fit}}(\alpha, \beta) * G_{\text{norm}}(\alpha_{\text{ref}}, \beta_{\text{ref}}) * S_1(\alpha)] / [G_{\text{wav}}(\theta, \lambda) * G_{\text{elev}}(\alpha)] \quad (7.1)$$

$$\alpha_{\text{ref}} = 1.544^\circ \quad \beta_{\text{ref}} = 59.792^\circ$$

$$G_{\text{fit}}(\alpha, \beta) = c_1 + c_2\alpha + c_3\beta + c_4\alpha^2 + c_5\alpha\beta + c_6\beta^2 + c_7\alpha^3 + c_8\alpha^2\beta + c_9\alpha\beta^2 + c_{10}\beta^3 + c_{11}\alpha^4 + c_{12}\alpha^3\beta + c_{13}\alpha^2\beta^2 + c_{14}\alpha\beta^3 + c_{15}\beta^4 \quad (7.2)$$

$$G_{\text{norm}}(\alpha_{\text{ref}}, \beta_{\text{ref}}) = \frac{1}{G_{\text{fit}}(\alpha_{\text{ref}}, \beta_{\text{ref}}) * S_1(\alpha_{\text{ref}})} \quad (7.3)$$

$$S_1(\alpha) = \cos(53^\circ) / \cos(53^\circ + \alpha) \quad (7.4)$$

$$G_{\text{elev}}(\alpha) = f_1 + f_2\alpha \quad (7.5)$$

$$G_{\text{wav}}(\theta, \lambda) = d(\lambda) + e(\lambda) * \theta \quad (7.6)$$

$$d(\lambda) = d_1 + d_2\lambda + d_3\lambda^2 + d_4\lambda^3 + d_5\lambda^4$$

$$e(\lambda) = e_1 + e_2\lambda + e_3\lambda^2 + e_4\lambda^3 + e_5\lambda^4$$

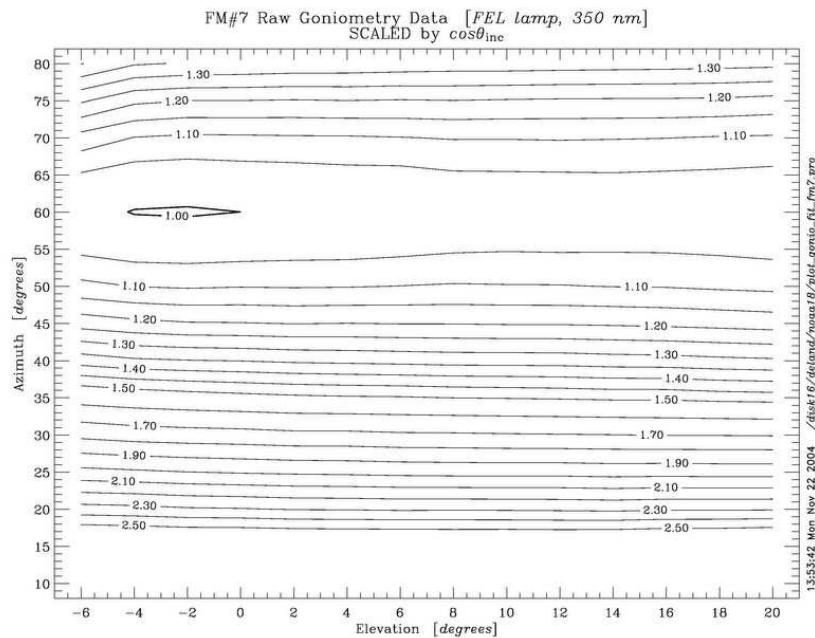


Figure 7.1: FM#7 prelaunch goniometry data at 350 nm using FEL lamp (incidence angle dependence removed).

NOAA-18 SBUV/2: Date = 2005/171

 $\beta_0 = 67.52^\circ$

V1 processing [sequence 2]

Diff. deg. corr.: none

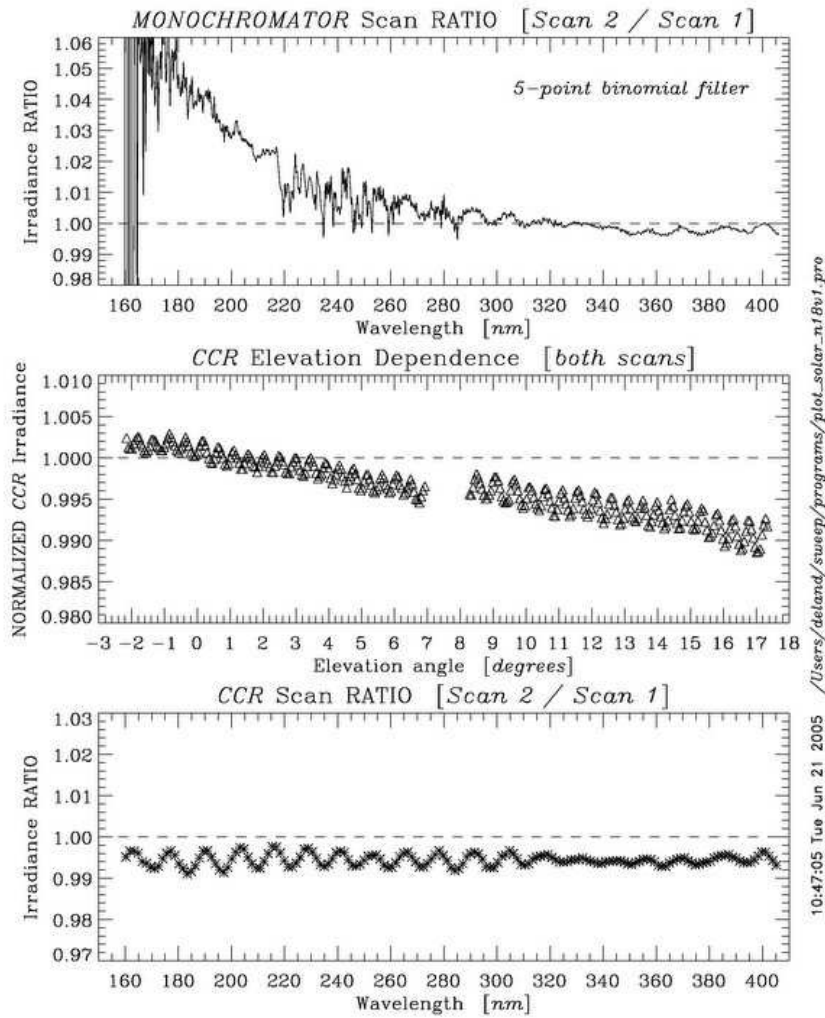


Figure 7.2: Sweep mode solar data processed with prelaunch goniometry: (*top*) Monochromator elevation dependence; (*middle*) CCR elevation dependence; (*bottom*) CCR scan ratio.

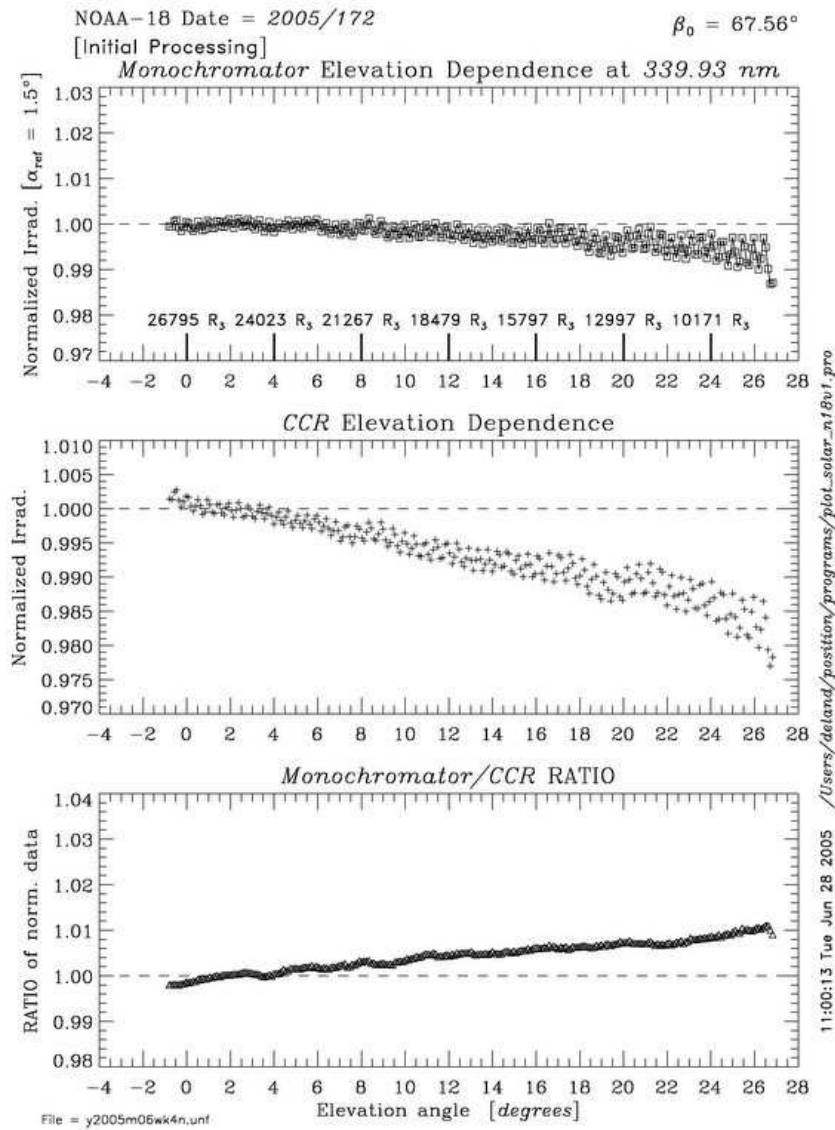


Figure 7.3: Elevation and wavelength dependence: Position mode, 340 nm.

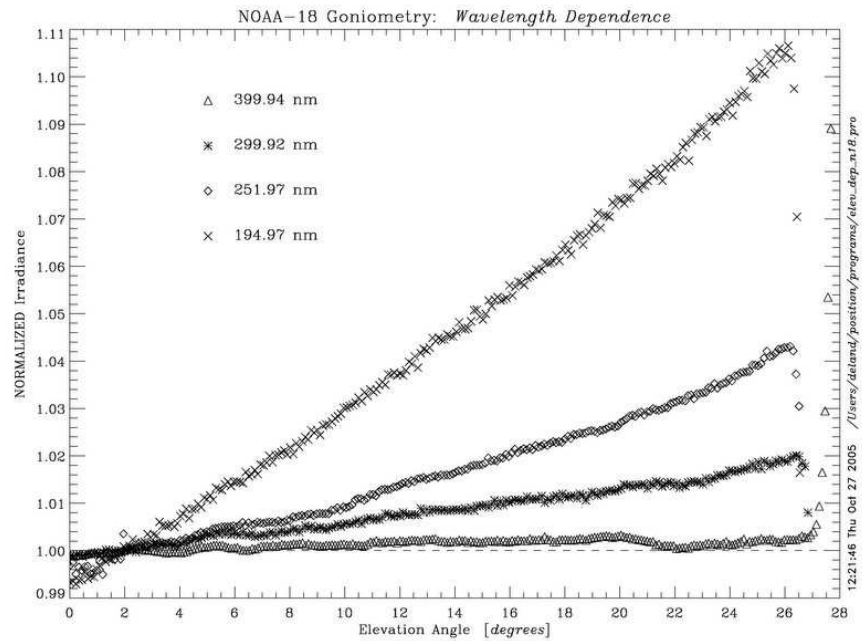


Figure 7.4: Wavelength dependence error of prelaunch goniometry.

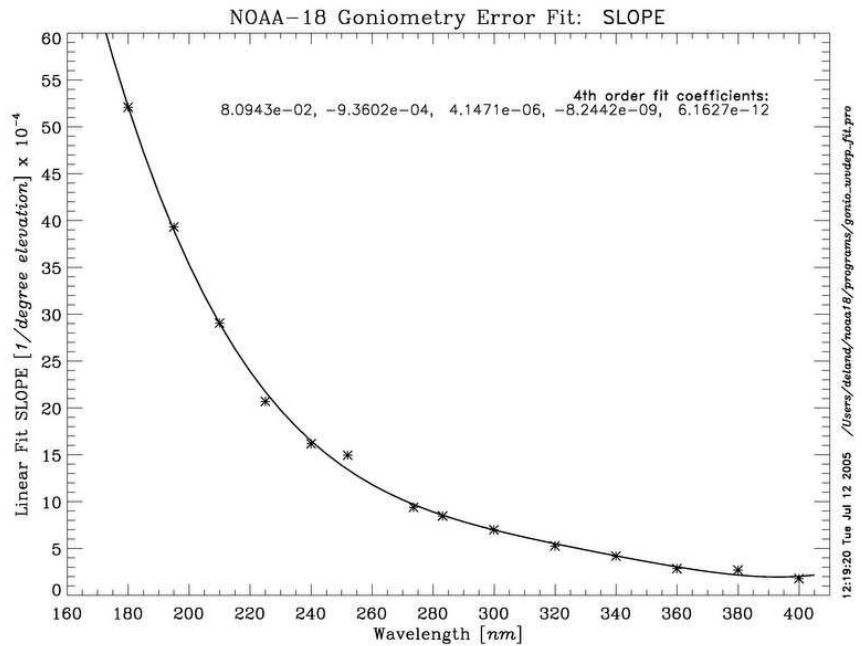


Figure 7.5: Goniometry wavelength dependence correction: Slope.

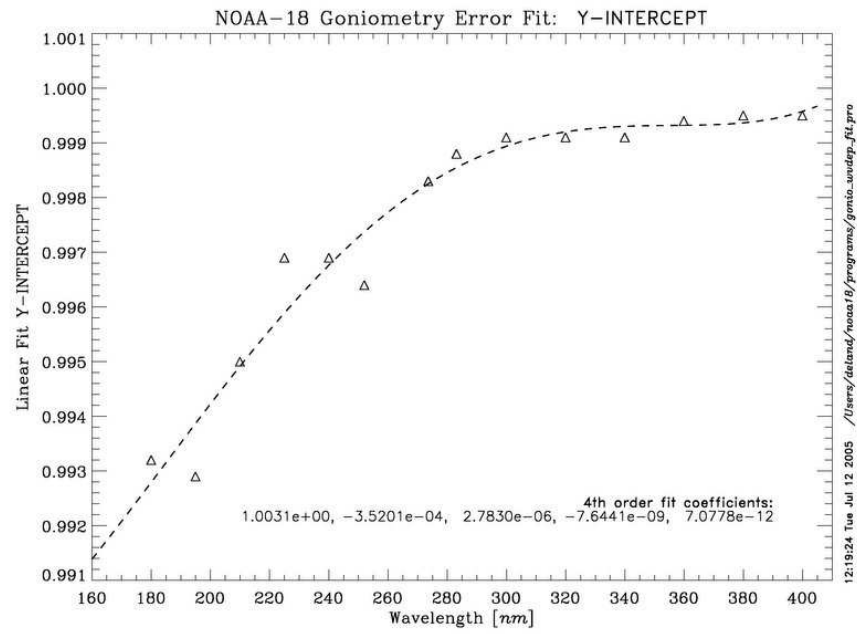


Figure 7.6: Goniometry wavelength dependence correction: Y-intercept.

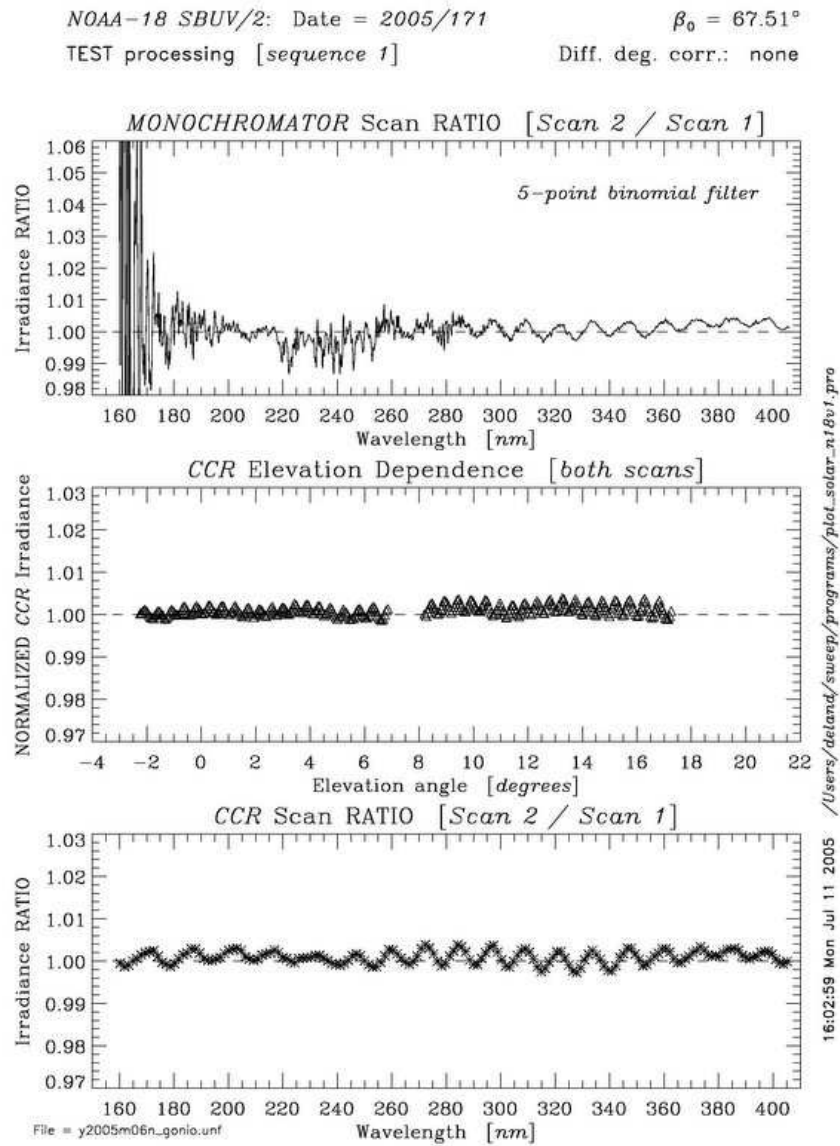


Figure 7.7: Sweep mode solar data: All goniometric corrections applied.

8. Thermal Response

Prelaunch tests were conducted in September-October 1998 to characterize the sensitivity of the FM#7 radiometric response to photomultiplier tube (PMT) temperature variations. The SBUV/2 instrument was placed in temperature controlled vacuum chamber and an FEL lamp outside the chamber was focused onto a diffuser at the sensor module entrance slit through a fused silica window. Measurements were taken at temperature levels of 21°C, -3.6°C, 8.7°C, 31°C and 20.7°C in a sequence. The first and last measurements at 21.0°C and 20.7°C were used to monitor and correct the source irradiance drift during the entire sequence. The measured counts were normalized at 20°C. The normalized counts between 8.7°C and 31°C are fitted with linear functions of temperature, as shown in Figure 8.1 (Range 2) and Figure 8.2 (Range 3 cathode). SSAI reprocessed the laboratory data and derived PMT temperature sensitivity coefficients in November 2004. Since the normal on-orbit temperatures are approximately 20°C (see Section 4), we excluded the data at -3.6°C from the analysis rather than using a more complex function. This step changed the thermal response coefficients by approximately $-0.0003 / ^\circ\text{C}$ in the anode outputs, and by $-0.0006 / ^\circ\text{C}$ in the Range 3 cathode output.

The PMT temperature sensitivity coefficients derived from the reprocessed data are plotted in Figure 8.3. Range 2 measurements were repeated with both Range 3 anode mode and Range 3 cathode mode, and the two sets of data were consistent with each other. Range 3 anode measurements covered a wavelength range from 318 nm to 406 nm, and they agreed very well with the results in Range 2 where the two data sets overlapped. The thermal sensitivity of the SBUV/2 instrument is primarily related to the PMT, while the amplifier thermal effect that would cause differences between Range 2 and Range 3 anode data is often negligible. Therefore, all of the Range 2 measurements and the Range 3 anode mode measurements were fitted together with a 4th order polynomial to provide a temperature coefficient function for all anode outputs including Range 1 in the wavelength range between 252 nm and 406 nm. Discrete mode measurements were not made at wavelengths below 252 nm. However, sweep mode data (Figure 6-1, Vol. 2 [[Data Book](#)]) suggest that the thermal response between 200-250 nm is basically flat. We recommend using the calculated 252 nm temperature sensitivity coefficient for all measurements at shorter wavelengths.

The thermal sensitivity test for Range 3 cathode mode covered the wavelength range 340-406 nm, whereas Earth view signals are observed in this mode down to 300 nm. The spectral dependence of the cathode temperature sensitivity shown in Figure 8.3 (*diamonds*) is consistent with the anode data, since both outputs share the same PMT cathode temperature response. The average Range 3 cathode temperature sensitivity (*dot-dashed line*) is lower because the anode output includes additional thermal response from the PMT dynodes. The recommended thermal correction for Range 3 cathode data therefore uses the same spectral dependence as the anode function, adjusted in absolute value to match the laboratory data at long wavelengths. PMT temperature correction coefficients for all gain ranges are listed in Table 8.1.

TABLE 8.1
PMT Temperature Dependence Correction

<i>Operating Mode</i>	<i>Wavelength Range</i>	C₀	C₁	C₂	C₃	C₄
Anode [Range 1, 2, 3]	$\lambda < 252$ nm	-2.7269e-03	0.0	0.0	0.0	0.0
	252-406 nm	-9.0312e-02	9.5413e-04	-3.7719e-06	6.3979e-09	-3.8954e-12
Cathode [Range 3]	$\lambda < 252$ nm	-1.0497e-03	0.0	0.0	0.0	0.0
	252-406 nm	-8.8635e-02	9.5413e-04	-3.7719e-06	6.3979e-09	-3.8954e-12
CCR	378.6 nm	-2.1657e-03	0.0	0.0	0.0	0.0

$$X_{\text{PMT}} = C_0 + C_1 * \lambda + C_2 * \lambda^2 + C_3 * \lambda^3$$

$$\text{Correction factor} = 1.0 + (X_{\text{PMT}} * (20^\circ\text{C} - T_{\text{PMT}}))$$

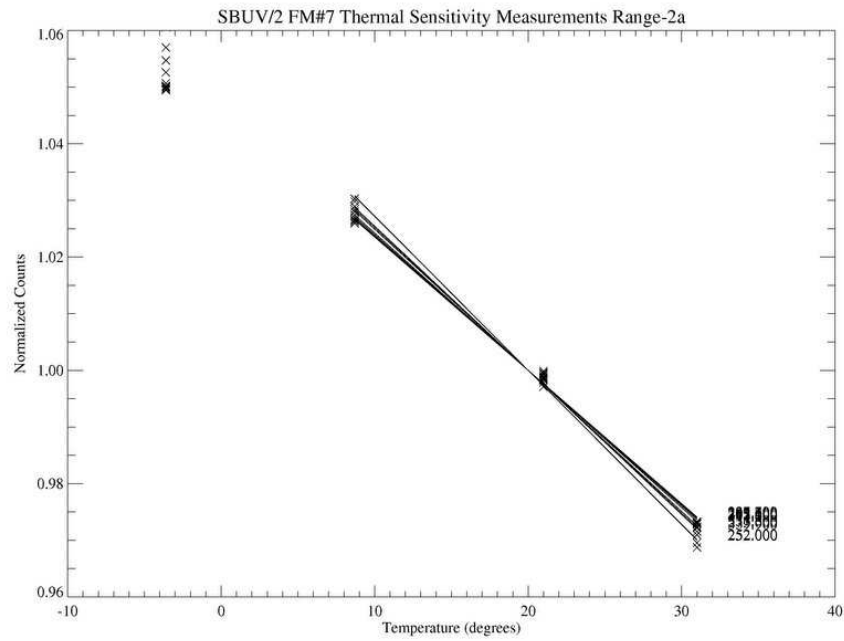


Figure 8.1: FM#7 thermal sensitivity: Response change for Range 2 data, normalized to 20°C.

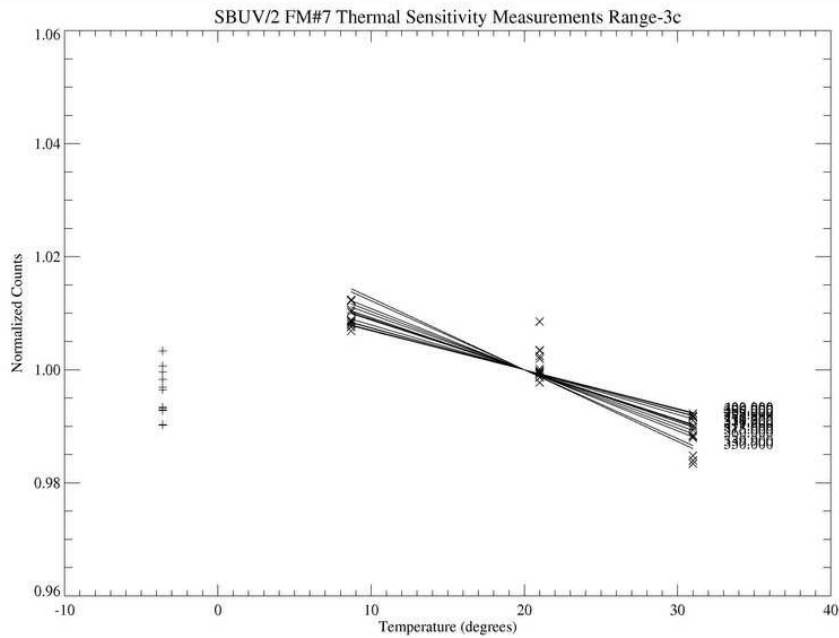


Figure 8.2: FM#7 thermal sensitivity: Response change for Range 3 cathode data, normalized to 20°C.

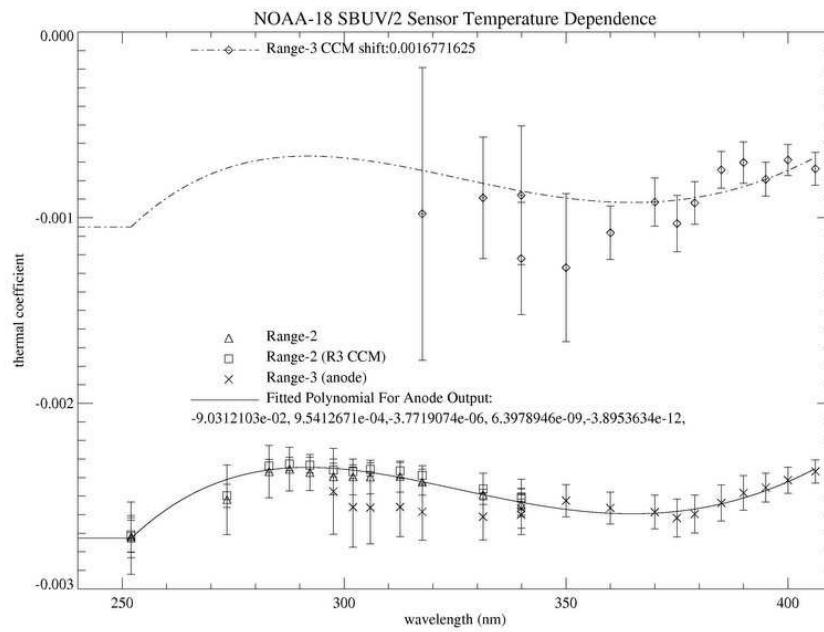


Figure 8.3: FM#7 thermal sensitivity: Spectral dependence of radiometric calibration change for 1°C increase in PMT temperature.

9. Interrange Ratios

The SBUV/2 instrument is required to observe signals which span six orders of magnitudes in intensity with better than 1% linearity. This is accomplished, in part, by the use of three gain ranges, each accommodating a range of two orders of magnitude in signal intensity. Range 1 is the most sensitive of the three gain ranges, while Range 3 is the least sensitive. In order to process data with a single radiometric sensitivity calibration, the data are converted to a common gain range using “interrange (gain) ratio” values. When discrete mode samples are observed with low counts in Range 2 (or Range 3), the simultaneous reading in Range 1 (or Range 2) may be also valid. After correcting the raw counts in each sample for calibration, the ratio of the corrected counts gives a direct measure of the interrangeratio between Range 1 and Range 2, denoted by IRR_{12} . A comparable quantity, IRR_{23} , is defined for Range 2 and Range 3 data.

NOAA-18 SBUV/2 has the capability of reading the Range 3 signal from either the anode output or the cathode current monitor of the photomultiplier tube (PMT). The Range 3 anode mode is expected to be used in routine ozone monitoring operation because it has less noise than Range 3 cathode data for total ozone wavelengths. This puts all three output ranges in common with the PMT gain. Thus, the PMT gain is canceled in gain ratios derived from this operating mode. The Range 3 output from the cathode current monitor is sampled before the electron multiplier (dynode) of the PMT. The interrangeratio between Ranges 2 and 3 in Range 3 cathode mode (IRR_{23C}) therefore characterizes the multiplication of photoelectron current from the cathode to the anode (PMT gain), including a constant factor associated with the electronics. IRR_{23C} has a significant wavelength dependence (~5% over total ozone wavelengths) and on-orbit time dependence (e.g. -10% for NOAA-16 SBUV/2 in the first year). When NOAA-18 operates in Range 3 anode mode, the SBUV/2 ozone retrieval algorithm does not require separate calibration of the monochromator PMT gain throughput. Nevertheless, the PMT gain change will directly affect the observed NOAA-18 SBUV/2 solar irradiance data, which are used to determine the time-dependent instrument characterization. $IRR_{23C}(t)$ represents the largest single component of the overall throughput change. For previous SBUV/2 instruments, derivation of albedo correction factor (ACF) values was simplified by first removing a smooth characterization of $IRR_{23}(t)$. In the event that the NOAA-18 SBUV/2 solar irradiance measurement is not available, independent information on changes in the PMT gain will be an essential item for accurate ozone retrieval calibration.

Data selection for interrangeratio analysis has typically limited the signal in the less sensitive gain range to lie between 350-750 counts for the anode outputs after adjustments for the electronic offset, the thermal response and the nonlinearity. The lower limit of 350 counts is chosen to reduce the uncertainty introduced by digitization and increasing non-linearity effects. The upper limit is chosen to avoid saturation in the more sensitive range. Data values exceeding 65,535 counts cause the 16-bit counter to roll over, but can still be used for the analysis if the instrument response is not saturated. Accepting these overflow values increases the number of samples at low solar zenith angles (SZA). For the NOAA-18 SBUV/2 IRR_{23C} analysis, the Range 3 data window was reduced to 150-400 counts because of the increase in PMT gain. Further discussion is presented in Section 9.3.

9.1. IRR_{12}

The data from Range 1 and Range 2 counters both come from the PMT anode and the preamplifier. The difference between Range 1 and Range 2 is due to the different electronic gains after branching into two different assemblies of the secondary amplifier, the voltage-frequency converter and the counter. The interranger ratio of Range 1 to Range 2 (IRR_{12}) is an electronic gain factor only. Thus, we expect little or no spectral or temporal dependence for IRR_{12} . Figure 9.1 shows the normalized time dependence of IRR_{12} measured with Channel 3 (283.16 nm). There was an increase less than 0.02% in the first four months, which is negligible. Figure 9.2 shows examples of measured IRR_{12} at other wavelengths relative to Channel 3, which are constant to better than $\pm 0.1\%$. This confirms that IRR_{12} is constant over time, as expected.

NOAA-18 IRR_{12} values measured for all ozone wavelengths on 2005 day 156 are shown in Figure 9.3 (*squares*). Also shown in the same figure are averages for the first four months (*crosses*), which are about 0.006% higher than the first day values. The value at 273.7 nm is about 0.02% higher than the values at longer wavelengths, which occur later in the scan sequence. Similar wavelength-dependent behavior was seen for NOAA-11, NOAA-16 and NOAA-17 SBUV/2, but not for NOAA-14. Valid IRR_{12} samples are obtained over a wide range of solar zenith angles, depending on the wavelength selected. Measurements for the seven longest wavelength channels were taken at SZA between 85-95°, while the four short wavelength channels were measured at SZA between 27-80°. There are no physical reasons to believe IRR_{12} is wavelength dependent. We believe that the behavior shown in Figure 9.3 is caused by instrumental effects experienced at high SZA as the signal strength changes rapidly. We therefore calculated IRR_{12} using only samples at SZA < 85°, which effectively limits the analysis to channels 1-4. This restriction is consistent with the current limit of the SBUV/2 ozone retrieval. The average IRR_{12} value calculated from all A&E data for these channels is **100.386**(± 0.007), which is consistent with the pre-launch value of 100.37.

9.2. IRR_{23} : Range 3 Anode Mode

The difference between the Range 2 and Range 3 anode outputs is only in the electronic amplifiers and digitizers, similar to Range 1 and Range 2. Thus, the gain ratio of Range 2 to Range 3 anode mode (IRR_{23A}) is expected to also be wavelength independent and very stable. No pre-launch calibration results for IRR_{23A} were reported in the Data Book. At SSAI's request, Ball Aerospace provided data taken during non-linearity tests in 1995 for further analysis. After correcting the data for non-linearity, derived IRR_{23A} values at all discrete ozone wavelengths agreed within the uncertainty at each wavelength. We therefore recommended a value of $IRR_{23A} = 99.998$ for the prelaunch calibration [*DeLand et al.*, 2005]. At the same time, we cautioned that IRR_{23A} might be changed after the electronics modifications in 1998.

This cautionary note was confirmed by inflight measurements. The initial on-orbit value for IRR_{23A} averaged over channels 8-12 was 92.47, a decrease of -7.5% from the prelaunch value. This change is consistent with the radiometric calibration changes observed after 1998. Figure

9.4 shows the channel-to-channel variation of IRR_{23A} values at total ozone wavelengths, with squares representing initial values on 2005 day 156 and crosses representing averages over the first four months. The error bars are the standard deviations in the averages. While the statistical noise is small, the maximum channel-to-channel variation is almost 0.38%. To examine any possible periodic oscillation in the sensor electronics, which exists in NOAA-16 SBUV/2 Range 3 cathode output, measurements in earth view position mode for different wavelengths were used to derive IRR_{23A} . The results are plotted in Figure 9.5 as a function of sample position with statistical standard errors. Data points without error bars had only a single measurement. The average of standard deviations for all valid measurements is 0.24, which is comparable with the channel-to-channel variation. Thus, no conclusion can be drawn from the position mode measurement due to poor statistics. Therefore, we recommend the average value of IRR_{23A} derived from all channels for the NOAA-18 ozone data processing.

Figure 9.6 shows normalized daily averages of IRR_{23} measured on-orbit with Channel 8 (305.9 nm) over the first four months. The day-to-day variation is less than 0.01% (standard deviation), which is no larger than the statistical noise in the daily average. The smoothed daily average (*solid curve*) shows less than 0.07% drift, which is negligible. Figure 9.7 shows that there are no significant temporal changes in the channel-to-channel differences relative to Channel 8, as expected.

Figure 9.8 shows monthly IRR_{23A} values plotted as a function of solar zenith angle, where negative values represent Southern Hemisphere data and positive values indicate Northern Hemisphere data. As an afternoon satellite, NOAA-18 emerges from the night in the Southern Hemisphere, where the sensor signal level immediately increases by several orders in magnitude within 1-2 minutes. IRR_{23A} values for individual channels in August 2005 are observed to vary by up to $\sim 0.5\%$ at $SZA > 60^\circ$ (*top panel*). Northern Hemisphere IRR_{23A} data show a rapid increase of $\sim 1\%$ for $SZA > 80^\circ$ (*right side*). September 2005 data show almost identical behavior (*bottom panel*). Both Range 2 and Range 3 counts in IRR_{23A} data are taken from the PMT anode, so these results cannot be explained by the PMT hysteresis phenomenon observed with NOAA-9 SBUV/2. Since we do not have a plausible mechanism for either channel-to-channel or SZA-dependent variations in IRR_{23A} , no correction will be attempted at this time. We derived a constant value of $IRR_{23A} = 92.397(\pm 0.25)$ for operational use.

9.3. IRR_{23} : Range 3 Cathode Mode

Previous SBUV/2 instruments have shown that the behavior of IRR_{23C} can be decomposed into two factors: wavelength-dependent “Day 1” values $IRR_{23C}(\lambda, t_0)$, and a wavelength-independent drift factor, $D(t)$. Prelaunch tests to determine $IRR_{23C}(\lambda)$ were performed in March 1996, and the data are listed in Tables 4.3-1 and 4.3-2, Vol. 2 [Data Book]. Two sets of data were taken over the wavelength range 210-405 nm, with input signals corresponding to approximately 40,000 counts and 70,000 counts Range 2, respectively. SSAI calculated a 4th order wavelength-dependent fit to these data, shown in Figure 9.9. After the FM#7 electronics modifications in 1998, the magnitude of IRR_{23C} decreased by approximately 10%. If the electronic modification in 1998 did not change the voltage across the cathode and the first dynode, the wavelength dependence of the PMT gain should remain the same. New IRR_{23C} wavelength dependence tests

were conducted in March 2003, using a different experimental fixture than the 1995 test. As a result, the high count test only covered the wavelength range 313-405 nm, while the low count test covered the range 292-405 nm. SSAI reprocessed the data with updated nonlinearity corrections, as discussed in Section 10. The magnitude of IRR_{23C} in 2003 is approximately 12% lower than in 1996, but the spectral dependence is very similar in the overlap region. We therefore adopted the wavelength dependence derived from the 1996 tests and scaled it to the data in 2003 to determine $IRR_{23C}(\lambda)$. The calculated values of IRR_{23C} for the ozone wavelengths at the start of solar irradiance measurements (2005 day 171) are listed in Table 9.2.

Inflight measurements in Range 3 cathode mode were first performed for approximately 24 hours on 2005 days 158-159, and repeated on days 186-187. When the operational schedule started on September 1, Range 3 cathode data are collected for four orbits once per week (Table 3.1). The average IRR_{23C} values derived from these data are shown in Figure 9.10, where a full day of the measurements in Earth view represents approximately 450 samples at 306 nm and 32 samples at 340 nm. A weighted least square fit is used to scale the prelaunch calibration polynomial to match the inflight measurements. The initial measurement of inflight IRR_{23C} was approximately 1.5% lower than the prelaunch calibration. The time dependence of IRR_{23C} during the first four months of operation is plotted in Figure 9.11. The current drift rate is approximately $-6.8(\pm 1.3)\%$ per year, roughly half of the drift rate observed from the first on-orbit tests.

Interrange Ratio IRR₁₂

$$\text{IRR}_{12} = 100.386$$

Interrange Ratio IRR₂₃: Range 3 anode mode

$$\text{IRR}_{23A} = 92.397$$

TABLE 9.1**Wavelength Dependence Fit Coefficients for IRR₂₃C (Range 3 cathode mode)**

<i>Coefficient</i>	<i>Value</i>
c_0	2.51215e+02
c_1	-1.34029e+00
c_2	9.34999e-03
c_3	-2.46479e-05
c_4	2.20736e-08

$$\text{IRR}_{23C}(\lambda, t_0) = c_0 + c_1 * \lambda + c_2 * \lambda^2 + c_3 * \lambda^3 + c_4 * \lambda^4$$

TABLE 9.2**IRR₂₃C Values at Ozone Wavelengths**

<i>Channel</i>	<i>Grating Position</i>	<i>Wavelength [nm]</i>	<i>IRR₂₃C Prelaunch</i>	<i>IRR₂₃C 2005/171</i>
1	486	252.039	201.804	197.803
2	195	273.702	203.309	199.278
3	67	283.164	203.686	199.648
4	5	287.732	203.806	199.765
5	-58	292.364	203.886	199.844
6	-130	297.643	203.928	199.885
7	-190	302.032	203.924	199.881
8	-243	305.901	203.892	199.849
9	-336	312.671	203.772	199.732
10	-404	317.604	203.637	199.600
11	-594	331.318	203.073	199.046
12	-714	339.923	202.597	198.580

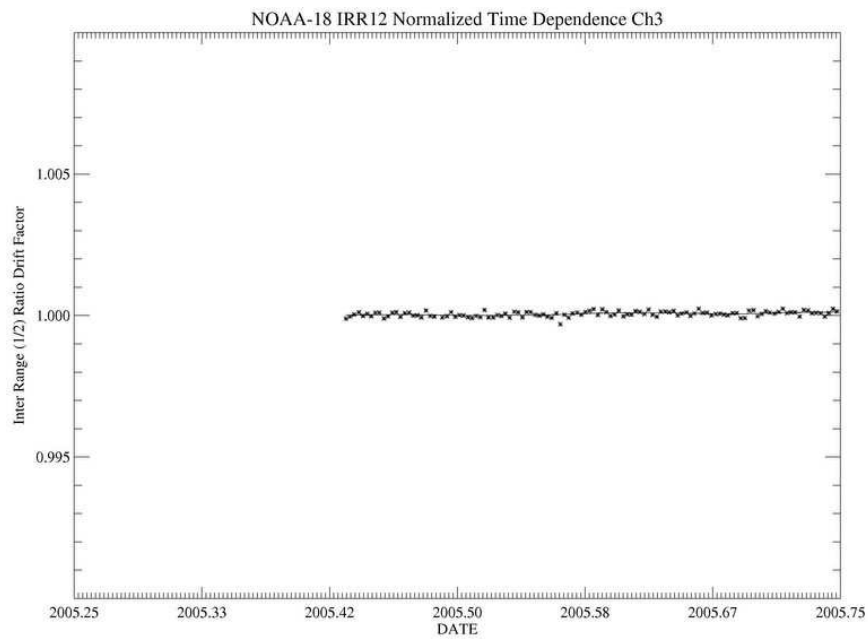


Figure 9.1: Time series of normalized IRR_{12} data at 283.2 nm.

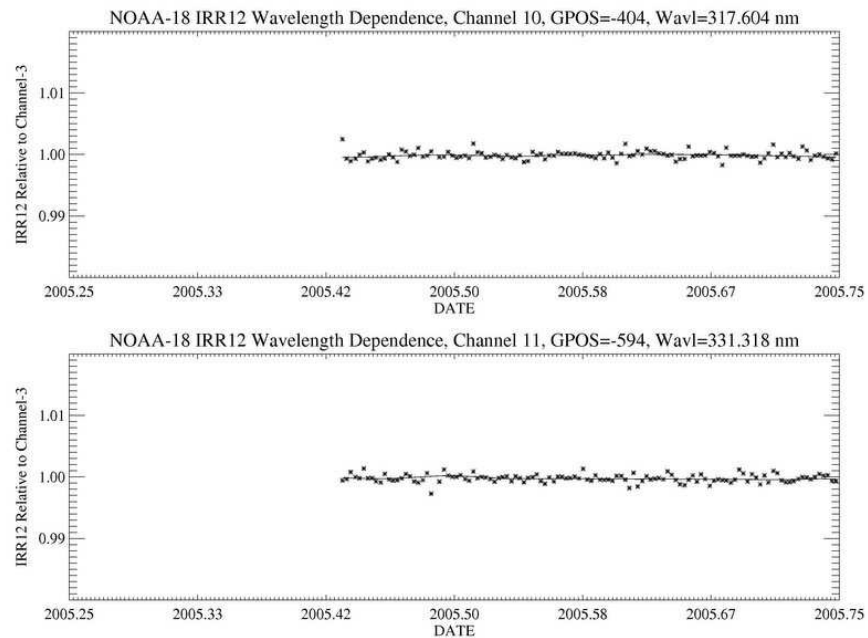


Figure 9.2: IRR_{12} spectral dependence vs. time: (*top*) 317.6 nm/283.2 nm; (*bottom*) 331.3 nm/283.2 nm.

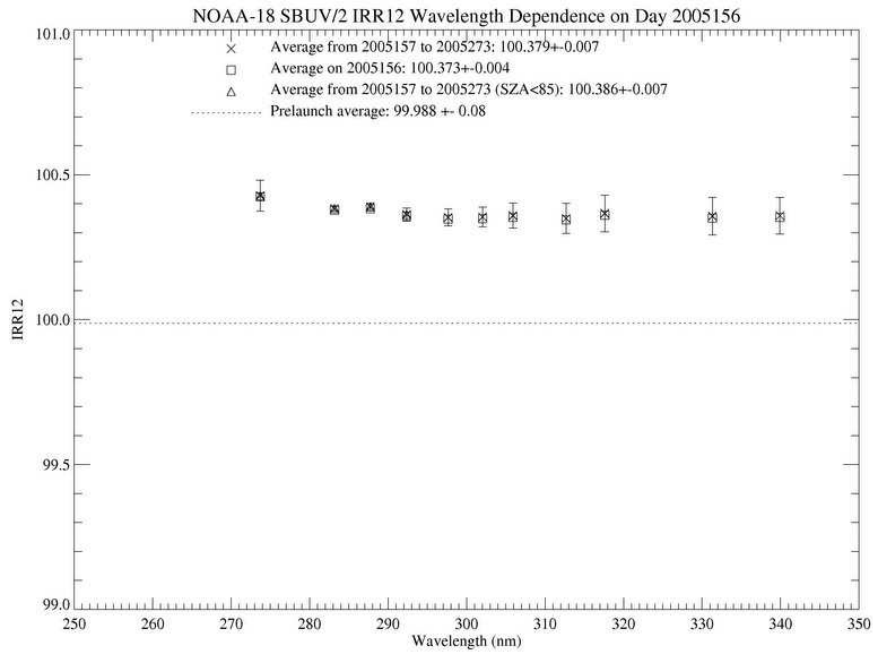


Figure 9.3: IRR₁₂ spectral dependence for first day of ozone measurements.

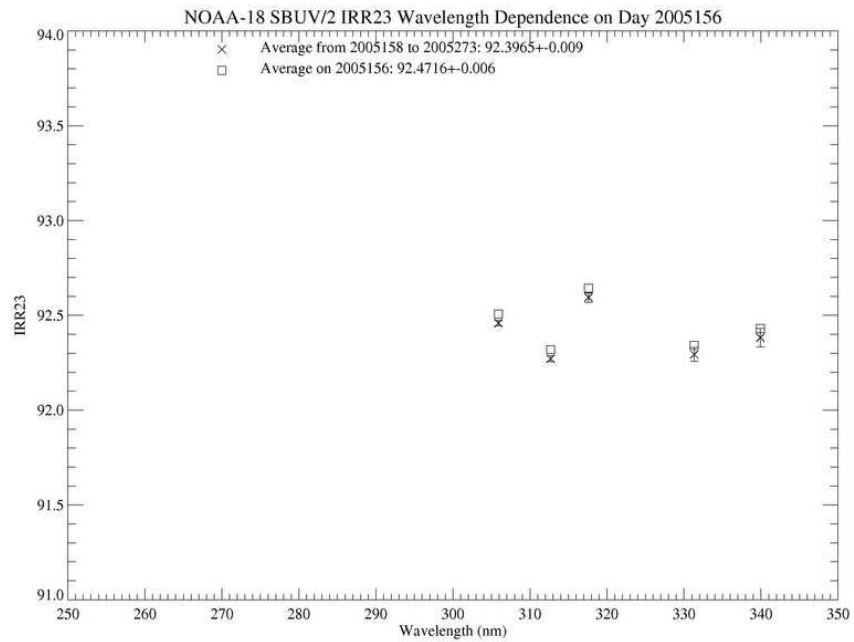


Figure 9.4: IRR_{23A} spectral dependence for first day of ozone measurements.

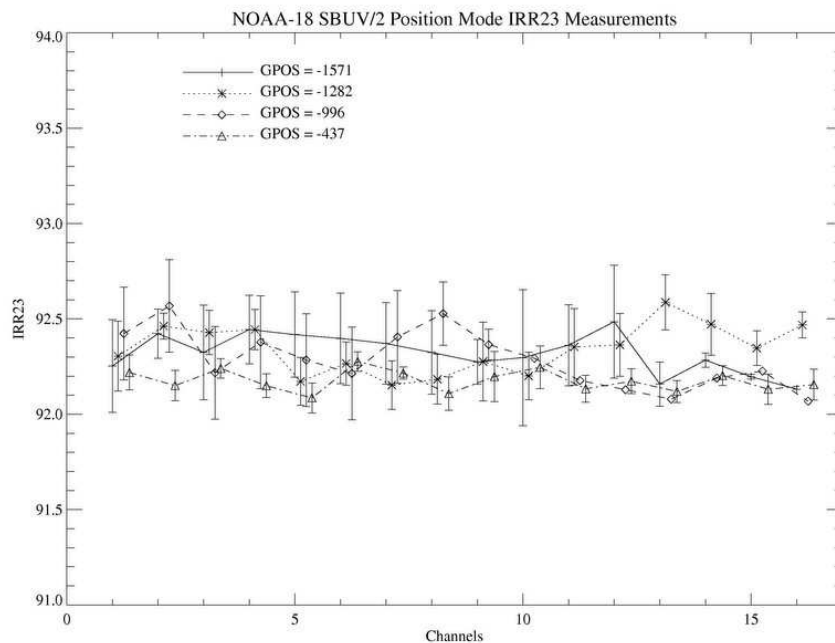


Figure 9.5: Position mode Earth view IRR₂₃A data vs. scan position: 400.0, 380.0, 360.0, 320.0 nm.

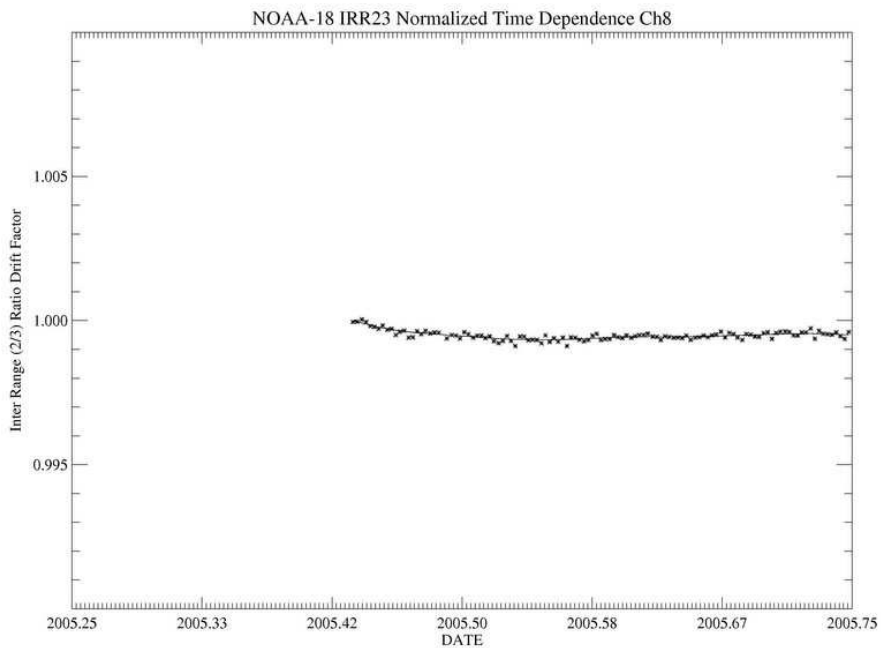


Figure 9.6: Time series of normalized IRR₂₃A (Range 3 anode) data at 305.8 nm.

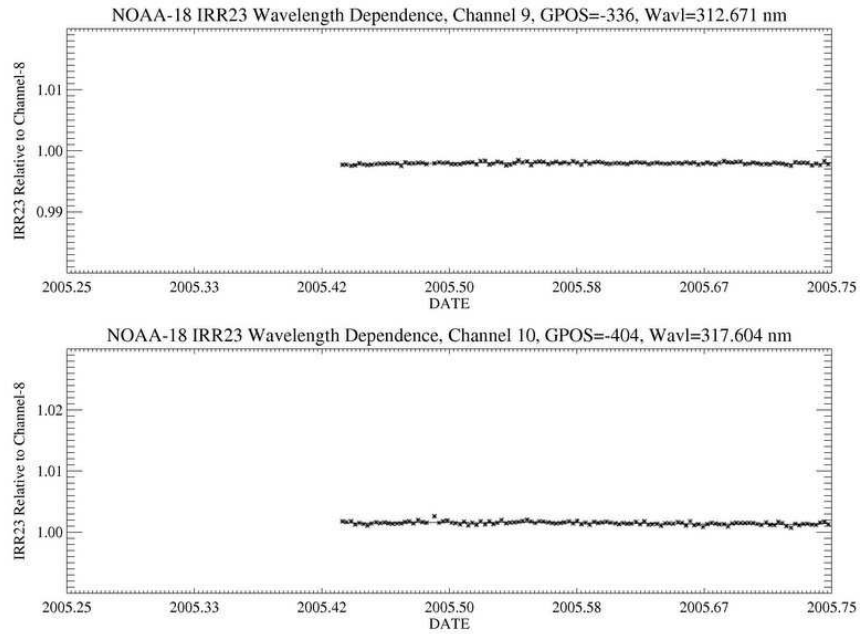


Figure 9.7: IRR₂₃A spectral dependence vs. time: (top) 312.5 nm/305.8 nm; (bottom) 317.5 nm/305.8 nm.

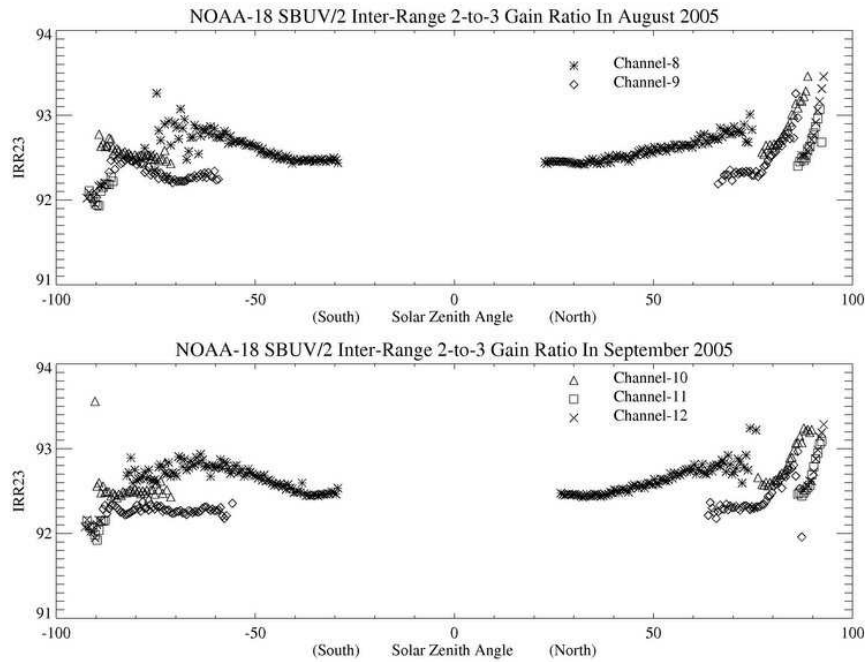


Figure 9.8: Monthly average IRR₂₃A values vs. solar zenith angle: (top) August 2005; (bottom) September 2005.

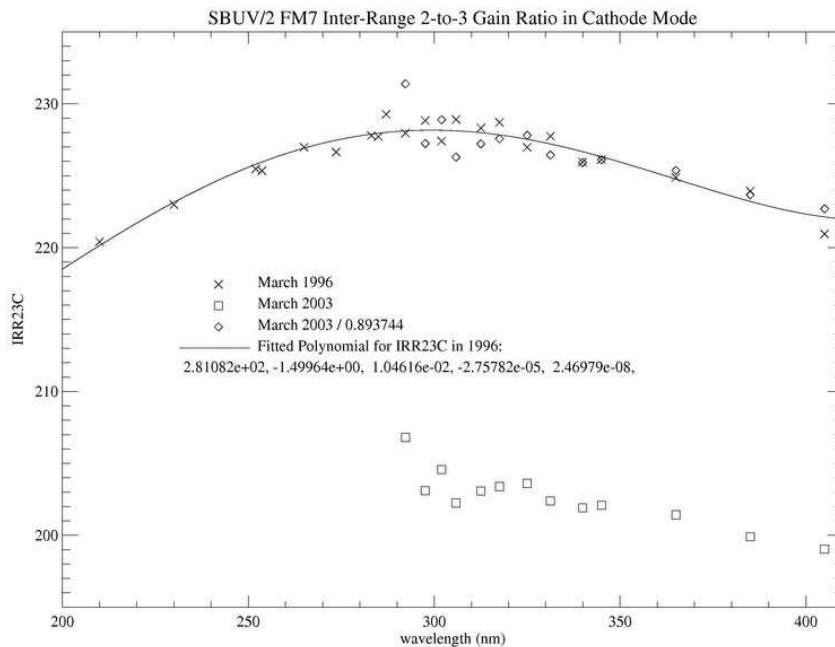


Figure 9.9: Spectral dependence of IRR₂₃C (Range 3 cathode) prelaunch data.

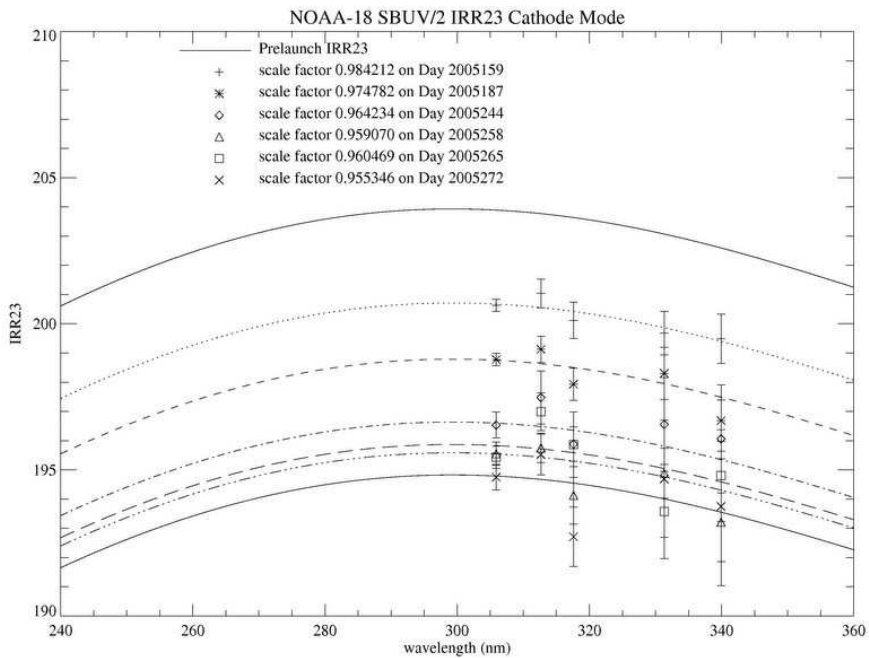


Figure 9.10: IRR₂₃C inflight spectral dependence for June-September 2005.

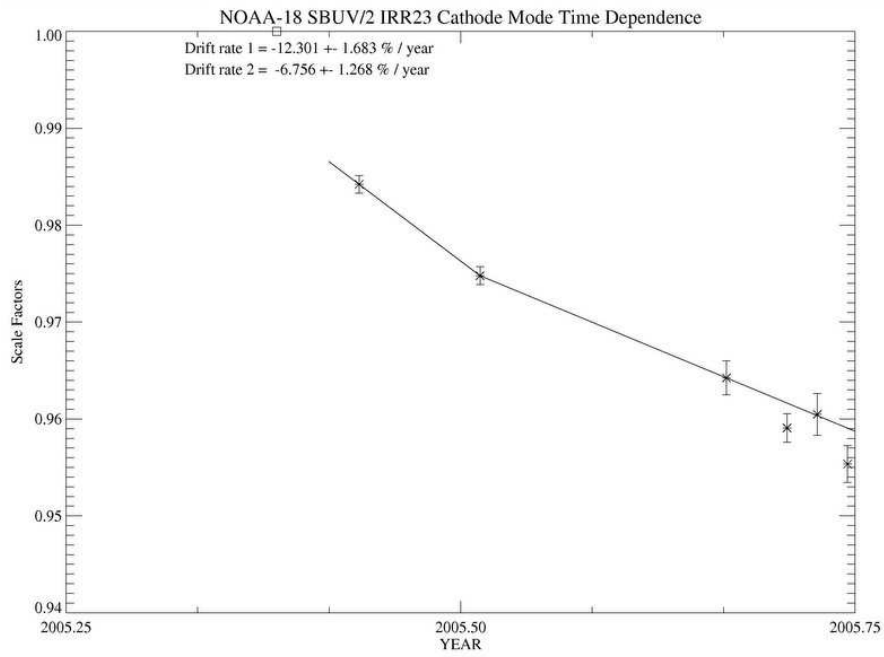


Figure 9.11: IRR₂₃C time dependence at 312.6 nm for June-September 2005.

10. Nonlinearity Correction

Measurements of SBUV/2 FM#7 nonlinearity were made for all three gain ranges in November 1995. Measurements were made using both anode and cathode Range 3 signals. These data are presented in Data Book Section 1 of Vol. 2. The coefficients for polynomial fits to each gain range calculated by Ball Aerospace are listed in radiometric calibration tables in Section 8, Vol. 2 [e.g. Table 8.2.2-1a]. Note that the prelaunch linearity tests were done before the instrument modifications in 1998, which actually changed the characterizations. SSAI staff reprocessed the prelaunch nonlinearity correction data and analyzed orbital data to characterize any changes after 1998 for better accuracy.

The prelaunch calibration used a set of neutral density filters and calibrated apertures to vary the signal level. Differences in the observed response from the nominal change due to aperture size change are considered to represent nonlinear behavior. The results are then normalized to a fiducial value for each range. A paper by *Pitz* [1979] explains this method further. Measurements with the same neutral density filter were first normalized at 15,000 counts, based on a linear interpolation of 3 measurements around 15,000 counts. After the normalization, all measurements were combined together. A detailed discussion on the importance to choose a high-count level in the normalization procedure to reduce the calibration uncertainty was presented in the NOAA-16 SBUV/2 A&E report [*DeLand and Huang*, 2001]. Ball Aerospace has adopted this normalization scheme for the FM#7 prelaunch calibration.

We evaluated the prelaunch nonlinearity measurements to validate the functional fits. FM#7 had two runs of the same calibration procedure for the Range 3 anode output and cathode output, respectively. However, only results from the Range 3 anode run were included for the Range 1 and Range 2 nonlinearity analysis in the Data Book. Since there is no expected physical difference in the Range 1 and Range 2 output between Range 3 cathode and anode measurements, we can combine the data from both runs. As shown in Figures 10.1 and 10.2, the nonlinearity measurements from both runs fully agree with each other at high signal level (counts > 1000). Below 1000 counts, the measurement accuracy is limited by the digitizer resolution and the difference between the two runs is consistent with the digitizer uncertainty. Therefore, inclusion of both Range 3 cathode and anode runs for the Range 1 and Range 2 calibrations will reduce the noise and provide some estimate of the calibration uncertainties.

10.1. Range 1 Measurements

Figure 10.1 shows that measurements with Range 1 signal levels between 2000 and 90,000 counts in both runs tracked each other very well. At low counts (< 1000), the noise level increased to 1%, which was consistent with expected uncertainty largely due to the digitizer uncertainty, the Range 1 offset noise and scattered light. An average over all measurements below 1000 counts is 0.03%. Data values below 1000 counts Range 1 are rarely observed in discrete ozone measurements, and should be even less frequent for NOAA-18 SBUV/2 because of the increase in instrument sensitivity. We calculated a 3rd order polynomial fit to the combined data from both runs as a function of raw counts to emphasize the instrument behavior in the data re-

gion most commonly used on-orbit. This method effectively averages all low count samples together, resulting in a value near zero. No measurable nonlinearity is found below ~60,000 counts, increasing to -0.6% at ~90,000 counts. The fitted function follows this deviation very well. Since operational ozone processing switches to Range 2 data at Range 1 signal levels of 55,000-60,000 counts, this nonlinearity at very high counts will have no direct impact. The finding of a negligible nonlinearity in Range 1 is consistent with the commonly known fact that the PMT and electronic amplifiers working at low signal level usually have good linearity.

10.2. Range 2 Measurements in 1995

Range 2 nonlinearity data from 12 prelaunch runs are very consistent with each other, as shown in Figure 10.2. Data with neutral density filter #4 (NDF#4) in Range 3 cathode mode (*squares with diagonal tick*) were discarded because they exceeded a 3σ discrepancy from the average. The remaining data were renormalized at 550 counts, where measurements valid in both Range 1 and Range 2 for interranging ratio analysis will have a minimal nonlinearity correction in either range. The Range 2 nonlinearity error below 63,000 counts is less than 0.3%. The raw data show evidence of saturation above 83,000 counts, so we derived a revised fit as a 1st order function of $\log_{10}[\text{net counts}]$ only for signal levels less than 63,000 counts. An additional 2nd order term was derived for use with high count data (Figure 10.2, *inset plot*).

10.3. Range 2 Measurements in 2003 and On-orbit

Later prelaunch calibration data suggested that the FM#7 modifications in 1998 might have changed the Range 2 linearity characterization. Range 3 cathode data collected in 2003 shows that derived $\text{IRR}_{23\text{C}}$ values at high Range 2 counts (~70,000) were approximately 1.5% higher than the average value using low counts (<45,000), as shown in Figure 10.3. However, we could not make a definite judgment from these data as to whether the discrepancy was caused by a problem with Range 2 nonlinearity at high counts or from Range 3 cathode nonlinearity at low counts.

NOAA-18 SBUV/2 collected two orbits of data in position mode at 380 nm on 2005 day 156. The monochromator and CCR were looking at the same scene at almost identical wavelengths, so the observed response should be very similar. Figure 10.4 shows ratios of simultaneous Range 2 monochromator counts to CCR counts, corrected with the 1995 nonlinearity calibration and normalized between 20,000-40,000 counts. An upward drift is observed beginning at 45,000 counts Range 2, reaching $2(\pm 0.5)\%$ at 80,000 counts. The CCR Range 3 count values below 20,000 counts Range 2 are too noisy for useful analysis. Since the CCR linearity is well-established from prelaunch tests with previous SBUV/2 instruments, we interpret these results as an error in the Range 2 nonlinearity correction. Figure 10.5 shows similar behavior for comparisons between Range 2 and Range 3 anode data. We therefore derived a linear fit to correct Range 2 data above 45,000 counts. This function is listed in Table 10.1.

10.4. Range 3 Measurements in Anode Mode

The prelaunch Range 3 anode nonlinearity calibration data are generally very consistent between different runs, although the results with NDF#3 are slightly offset at lower counts (Figure 10.6). We normalized the laboratory data at 550 counts to ensure consistent behavior in the data range used for calculating IRR_{23A}. The calculated 3rd order polynomial fit is ~0.3% lower than the function provided by Ball, but has the same shape as a function of signal level. The absolute shift does not affect other prelaunch calibration results because Range 3 data are not normally observed, except for Hg lamp measurements at 254 nm (see Section 11.5.3).

Figure 10.7 shows the inflight IRR_{23A} data as a function of Range 2 counts, using the updated Range 2 nonlinearity correction discussed in Section 10.3 and the prelaunch Range 3 nonlinearity calibration. The variation is approximately $\pm 0.1\%$ between 30,000-80,000 counts in Range 2 (or between 325-850 counts in Range 3), indicating that the nonlinearity corrections in both Range 2 and Range 3 are reasonably accurate. An offset of +0.3% below 30,000 counts Range 2 corresponds to less than 325 counts Range 3, which is not used operationally. Previous measurements indicate that the Range 2 correction is valid in this region. To validate the nonlinearity calibration at high Range 3 count values, we compare Range 3 counts at 380 nm with CCR values in position mode (Figure 10.8). The solid line is a smooth fit with a 3000 count window. Variations from unity are less than $\pm 0.2\%$ below 20,000 counts, and show a small positive bias between 20,000-35,000 counts. We do not have additional information to evaluate the Range 3 anode nonlinearity correction, so we recommend using the function listed in Table 10.1.

10.5. Range 3 Measurements in Cathode Mode

Prelaunch Range 3 cathode nonlinearity calibration data are shown in Figure 10.9. Measurements using NDF#3 have larger differences from the average below 2000 counts, and measurements using NDF#4 at low signal levels were shown to be problematic in Section 10.2. Data from NDF#2 are only available below 300 counts. We therefore calculated a 3rd order fit for Range 3 cathode nonlinearity using only data from the NDF#5 and NDF#6 runs, normalizing at 300 counts for consistency with IRR_{23C} measurements. The count rate dependence is almost identical to the prelaunch function, but is ~0.4% lower in absolute value due to the choice of data normalization.

TABLE 10.1
Nonlinearity Correction Functions

Range	X	C₀	C₁	C₂	C₃
1	Net_counts	-2.60907e-03	-1.44378e-06	1.43247e-10	-2.35604e-15
2	Log ₁₀ [Net_counts]	-3.12808e-01	1.14148e-01	—	—
3A	Log ₁₀ [Net_counts]	-3.06384e+00	2.70097e+00	-7.94773e-01	7.92365e-02
3C	Log ₁₀ [Net_counts]	1.70323e+00	-1.59804e+00	4.69316e-01	-4.10845e-02

$$NL = C_0 + C_1 * X + C_2 * X^2 + C_3 * X^3$$

$$\text{Nonlinearity correction} = 1.0 / (1.0 + (NL/100))$$

For Range 2:

$$\text{count_true} = \text{cnt_pre} / (1.0 + 6.4693e-07 * (\text{cnt_pre} - 45,000)) \quad [\text{cnt_pre} > 45000]$$

cnt_pre = net counts after applying prelaunch nonlinearity calibration.

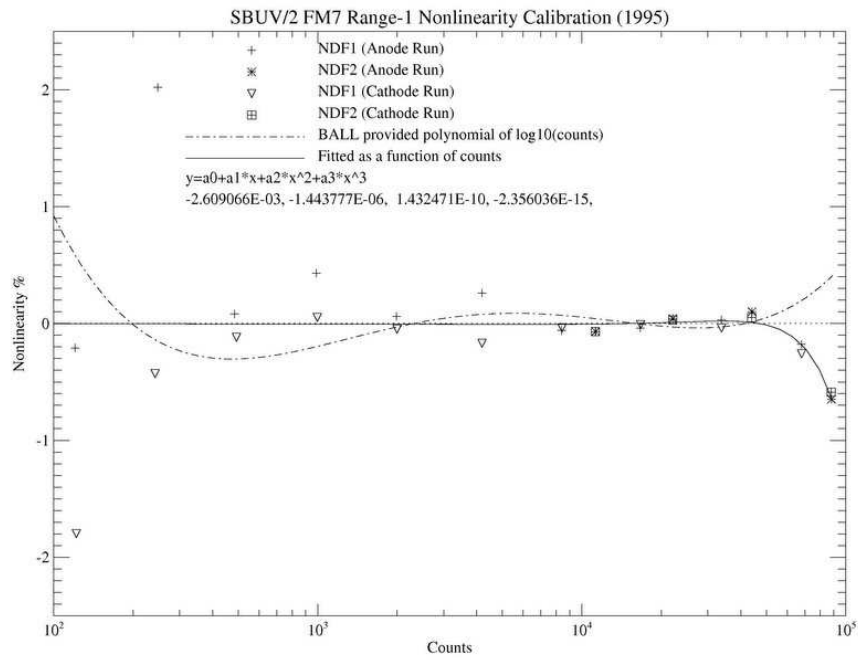


Figure 10.1: Prelaunch Range 1 non-linearity test data.

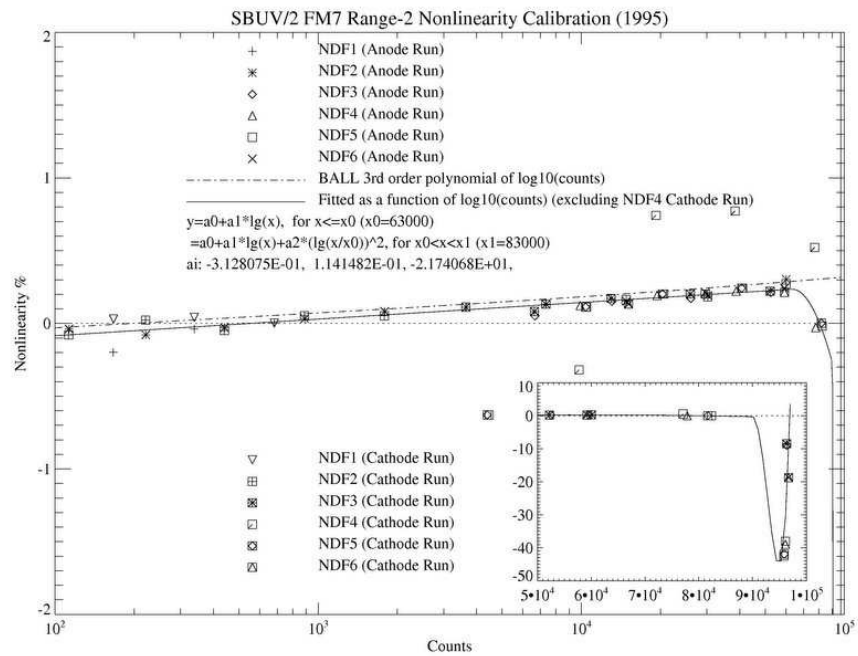


Figure 10.2: Prelaunch Range 2 non-linearity test data.

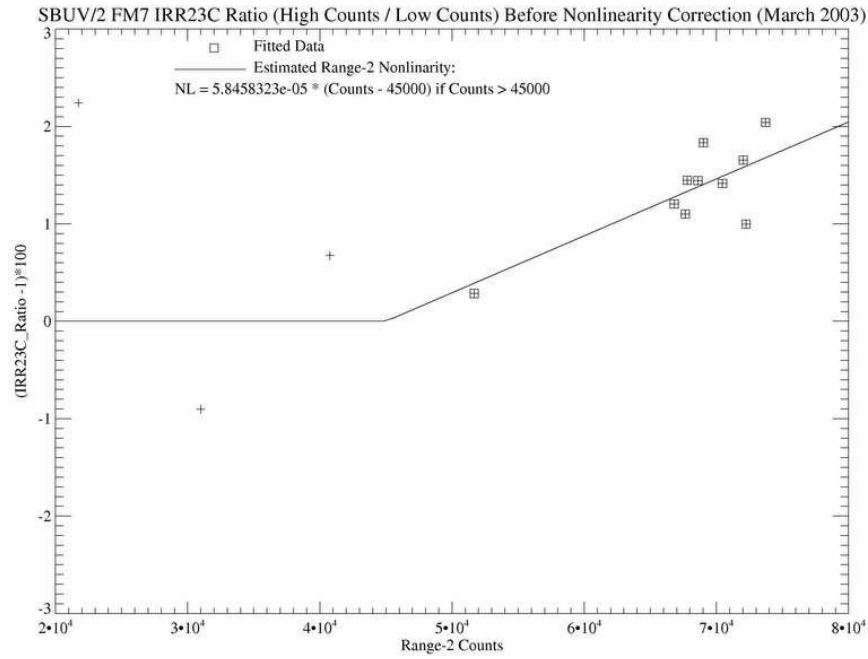


Figure 10.3: IRR_{23C} dependence on Range 2 counts using prelaunch nonlinearity correction.

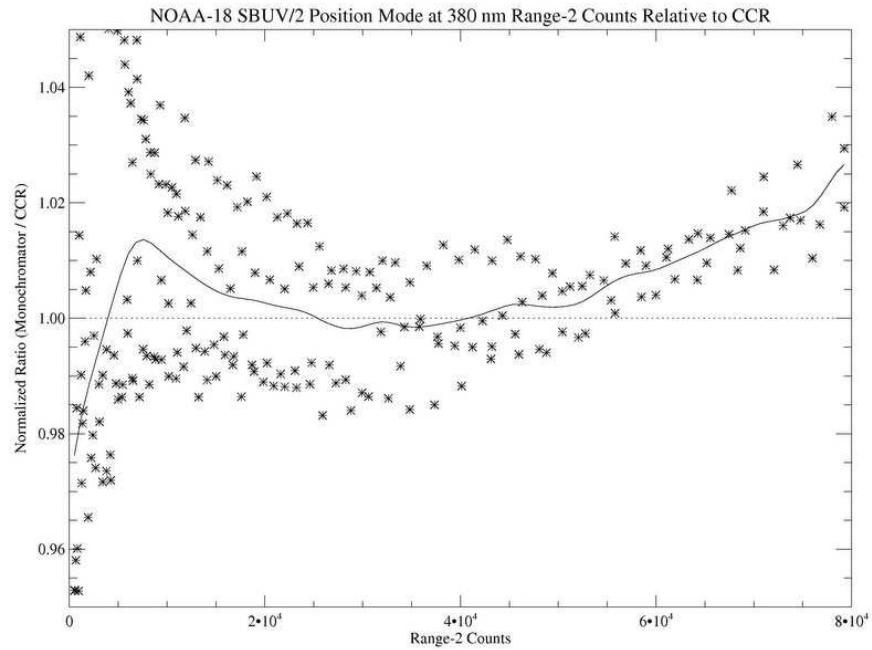


Figure 10.4: Ratio of inflight position mode measurements at 380 nm (Range 2 counts) to coincident CCR data, corrected with the prelaunch Range 2 nonlinearity calibration.

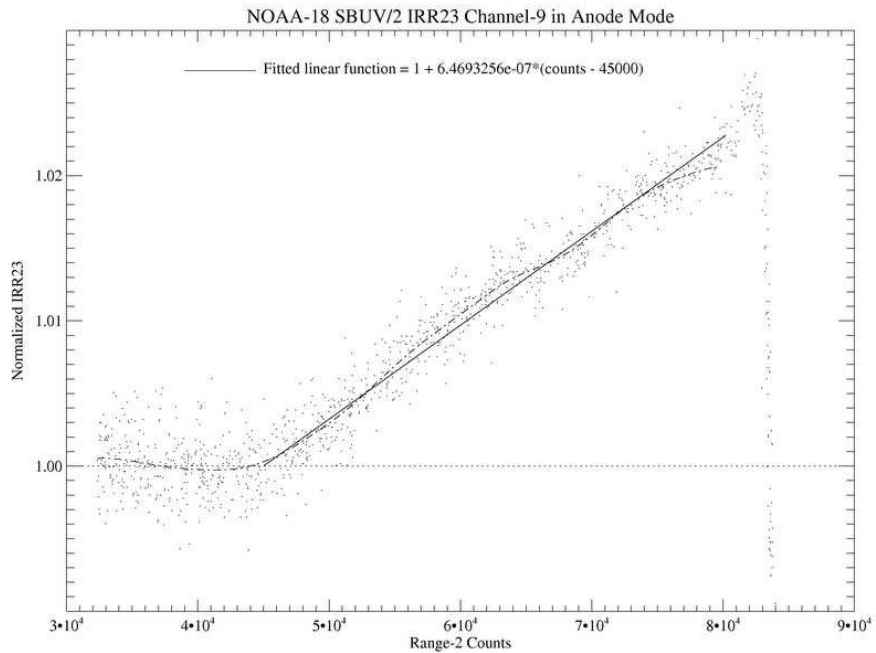


Figure 10.5: Inflight IRR₂₃A measurements at 312.6 nm as a function of Range 2 counts, corrected with the prelaunch Range 2 nonlinearity calibration and normalized below 45,000 counts. A linear fit to the high count Range 2 nonlinearity error is also shown.

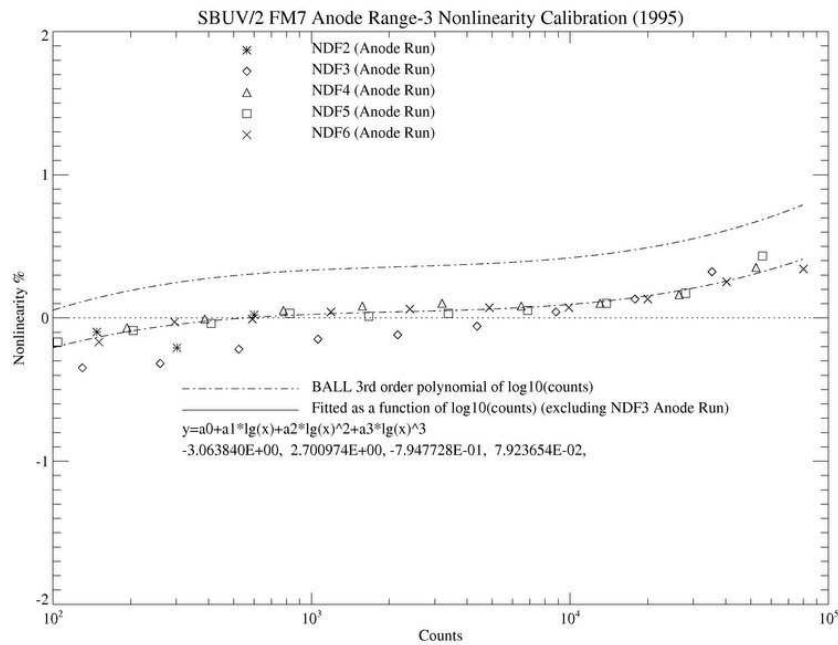


Figure 10.6: Prelaunch Range 3 anode non-linearity test data + Ball, SSAI fits.

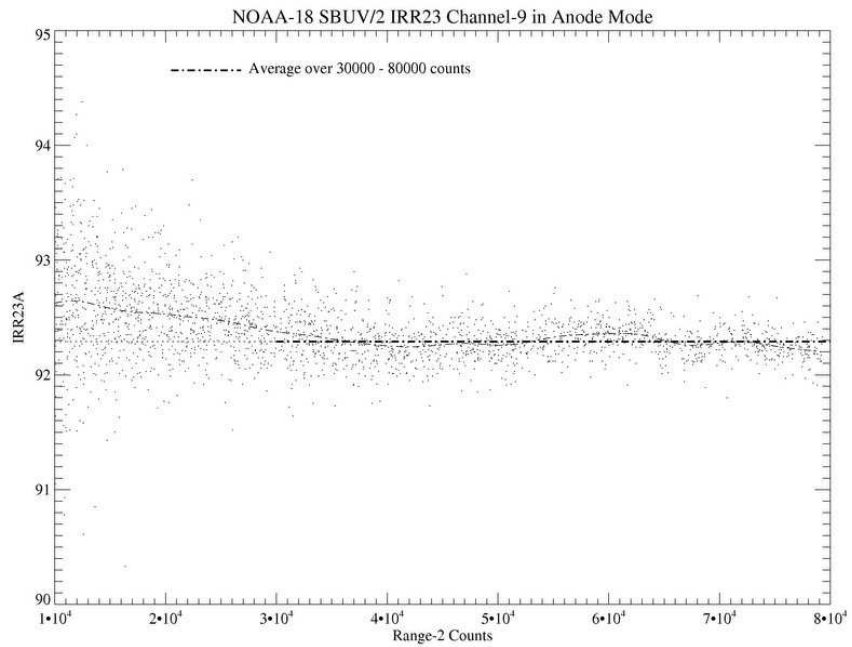


Figure 10.7: Inflight IRR_{23A} measurements at 312.6 nm as a function of Range 2 counts, corrected with the revised Range 2 nonlinearity calibration.

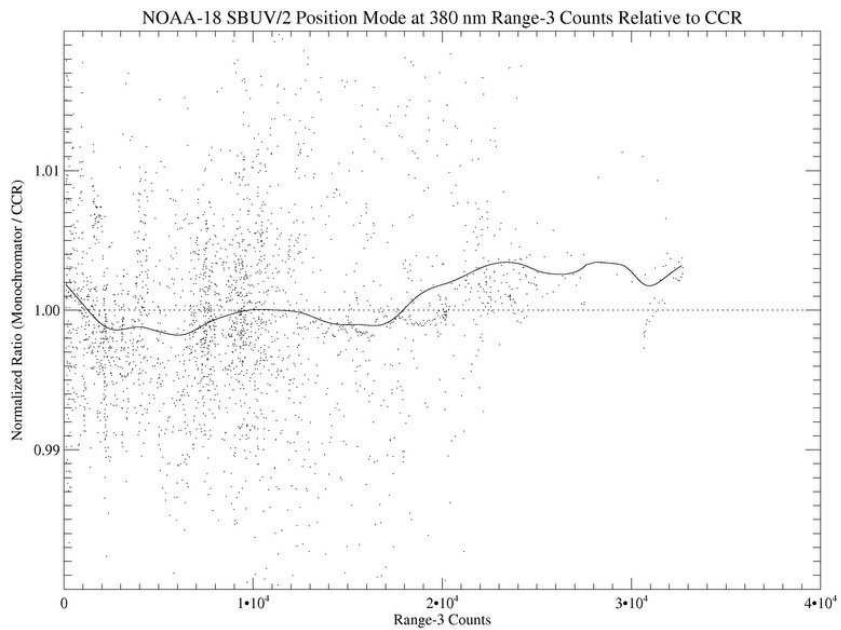


Figure 10.8: Ratio of inflight position mode measurements at 380 nm (Range 3 counts) to coincident CCR data, corrected with the prelaunch Range 3 nonlinearity calibration.

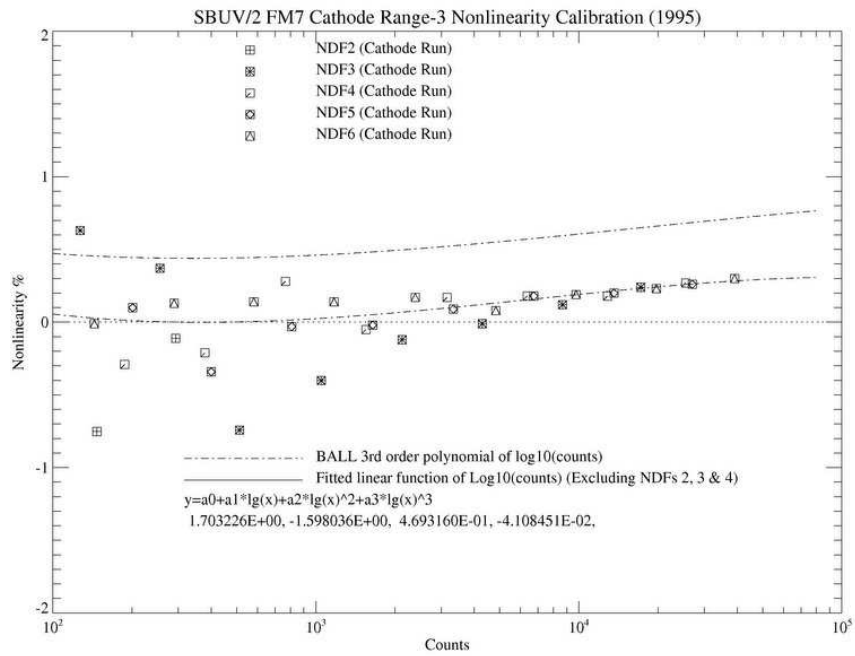


Figure 10.9: Prelaunch Range 3 cathode non-linearity test data + Ball, SSAI fits.

11. Diffuser Reflectivity Characterization

11.1. Introduction

In the BUV technique, the ratio of earth radiance to solar irradiance (defined as the geometrical albedo, $\alpha = I / F$) is the fundamental quantity in ozone retrieval. Whereas backscattered radiance is directly viewed by the spectrometer, the measured solar irradiance is reflected from a diffuser plate. Most instrument changes, with the exception of the diffuser reflectivity, are common to both radiance and irradiance measurements, and thus cancel out in the albedo. Thus, properly characterizing time dependent changes in the reflectivity is the single most important part of our long-term calibration process.

All SBUV/2 instruments have an on-board calibration system to monitor diffuser relative reflectance as a function of time and wavelength. The on-board calibration system uses a Hg lamp as the spectral source. Measurements are made in two configurations, lamp view and diffuser view. Figure 11.1 illustrates the two configurations. In the lamp view, the Hg lamp is placed in front of the entrance slit of the spectrometer. In the diffuser view, the spectrometer faces the solar diffuser and light from the lamp is reflected off the diffuser into the entrance slit. The diffuser reflectivity is defined as the ratio of the signal measured in the diffuser view to that measured in the lamp view. This on-board reflectivity measurement does not provide the bidirectional reflectance distribution function (BRDF) of the diffuser, nor does it fully simulate the diffuser reflection of the solar light [Jaross *et al.*, 1998]. The angular dependence of the reflectivity (part of the BRDF) is characterized in the goniometric calibration (see Section 7), and is assumed to be time-independent. While the illumination of the diffuser plate by the mercury lamp in the calibration is not identical to that provided by the solar irradiance, we assume that the measured relative diffuser reflectivity changes are consistent with the reflectivity changes in the solar viewing geometry.

During June 2005 and the first week in July 2005, we performed a total of 24 runs of the standard diffuser reflectivity calibration sequence immediately before and after the diffuser decontamination procedure and the first solar exposure. NOAA-18 SBUV/2 began regular weekly diffuser reflectivity calibrations on August 31, 2005. Discrete mode reflectivity calibrations were also performed from June 14 to October 2, 2005. The initial orbital measurements of the relative diffuser reflectivity are compared with the prelaunch calibration data to determine any changes from laboratory to orbit.

11.2. Sweep Mode Data

11.2.1. Measurement Sequence

The sweep mode diffuser reflectivity calibration is a preprogrammed measurement sequence that executes with a single command. This is the standard reflectivity monitoring procedure for all SBUV/2 instruments. Figure 11.2 shows the nominal reflectivity sequence, which consists of ten consecutive spectral scans. Six scans are taken in the diffuser view mode, and four scans in the

lamp view mode. Each spectral scan takes 192 seconds, starting at 406 nm and ending at 160 nm. Nominally, each sequence should take place over the night side with the start and finish of the 32 minute sequence scheduled to avoid daylight contamination. In practice, we select scans with solar zenith angles larger than 120°.

Figure 11.3a shows the Hg lamp spectrum from the lamp (direct) view in sweep mode. Ten emission lines are identified in this figure. Six of the lines (185.0, 253.7, 296.8, 312.6, 365.1, 404.7 nm) have consistently high signal-to-noise ratios, and are designated as “strong” lines. Data from these lines are the primary source for the reflectivity analysis. Figure 11.3b shows the corresponding spectrum in the diffuser view. The increased relative continuum noise level is caused by the approximate factor of 50 decrease in signal intensity. Because of the increased noise, certain lines (265.3, 289.4, 302.1, 334.2 nm) have poor signal-to-noise ratios and are designated as “weak” lines. Data from these lines are generally not suitable for the reflectivity calibration. Figure 11.4 shows examples of typical emission line profiles at 253.7 and 404.8 nm in lamp and diffuser view. The ‘x’ symbols show data points recorded at 2 step intervals. Note that the actual grating position readout in the sweep mode occurs only at the end of every 10 samples, which are marked with long ticks on the grating position axis. This means that no direct information is available regarding the grating position values or errors at all other locations.

11.2.2. Reflectivity Calculation

Before computing the spectral line intensity, all raw measurements are corrected for the electronic offset, PMT temperature, and non-linearity. The corrected counts in Range 1 and Range 2 are then converted to equivalent values in Range 3 using the interranger ratio values IRR_{12} and IRR_{23} from Section 9. The line intensity is calculated by summing the corrected counts over either 14 or 15 points around the center of a line profile, as shown by the solid curves in Figure 11.4. The choice of the number of data points in the summation depends on how the peak location is centered in the sweep scan. The summation covers a range of data points slightly narrower than the full line profile in order to minimize background light contamination. This is also consistent with the data reduction in the prelaunch diffuser reflectivity monitoring.

Figure 11.5 shows a typical example of the spectral line intensities evolving during 10 consecutive scans in a calibration sequence in September 2005, where ‘+’ represents diffuser view data and ‘*’ represents lamp view data. In order to plot all data in the same figure, the diffuser view line intensities are normalized to the average intensity from scans 7 and 8, and the lamp view line intensities are normalized to the average of scans 6 and 9. During a normal calibration sequence, the lamp is warming up during the first 4 scans. We use only scans 7 and 8 for the diffuser view measurements, and use only scans 6 and 9 for the lamp view measurements. We use linear interpolation of the line intensity to minimize the impact of the lamp drift. Therefore, all reflectivity values are calculated using the following formula:

$$R = \frac{I_7 + I_8}{I_6 + I_9} \quad [11.1]$$

where I_7 and I_8 are the line intensities at scans 7 and 8 in diffuser view, and I_6 and I_9 are the line intensities at scans 6 and 9 in lamp view. Tests were performed to include other scans for the reflectivity calculation, such as $R = [(I_4 + I_7)/(I_5 + I_6) + (I_7 + I_8)/(I_6 + I_9)]/2$. No improvement was found due to large uncertainty during scan 4. Figure 11.6 shows absolute diffuser reflectivity values at 254 nm and 406 nm calculated using Equation 11.1. The symbols ‘×’ and ‘*’ indicate different lamp polarity states. Further discussion of this effect is presented in Section 11.4.

11.2.3. Statistical Uncertainty

The statistical uncertainty for a reflectivity measurement includes the signal fluctuations, instrument noise, lamp source intensity drift (*i.e.* stability), repeatability between measurements, and grating position error effects. It is difficult to determine the measurement noise directly from the line intensity with only two scans. However, we can define a noise profile of percentage changes between two measurements of the same spectral profile in the same view, weighted by intensity,

$$N(\lambda_i) = 100 \times [f_2(\lambda_i)/f_1(\lambda_i) - 1] \times \rho(\lambda_i) \quad [11.2]$$

where f_1 and f_2 are the two line profile measurements, and ρ is the normalized spectral line intensity profile. If two profiles are identical at every data point, $N(\lambda_i)$ would be zero everywhere. The noise in the line intensity measurements is defined as the standard deviation of $N(\lambda_i)$ multiplied by the square-root of the number of data points for the line intensity. This definition makes the estimated noise level statistically meaningful with about 16 measurements in a line profile. The noise level in lamp view is less than 0.2%, which is negligible. The average noise level in diffuser view is less than 0.5% for the strong lines, and less than 2% for the weak lines.

The statistical uncertainty for the reflectivity is derived using the following formula,

$$\sigma = \sqrt{\sigma_L^2 + \Delta_L^2 + \sigma_D^2 + \Delta_D^2} \quad [11.3]$$

where σ_L and σ_D represent the estimated noise in the line intensity measurements, Δ_L and Δ_D are uncertainties due to the lamp source intensity drifts, and subscripts L and D correspond to lamp view and diffuser view, respectively. Δ_L and Δ_D are equal to the standard deviations of the line intensities in scans 6 and 9 for the lamp view and scans 7 and 8 in the diffuser view, respectively. The uncertainty due to grating drive error is missing from the above equation because no grating drive errors have been recorded.

11.3. Discrete Mode Data

The discrete mode calibration sequence was originally designed to check the wavelength calibration, as well as a backup to the sweep mode calibration sequence. Six spectral lines at 185.0, 253.7, 289.5, 296.8, 334.3 and 404.8 nm were selected. Each line profile was repeatedly scanned in the SBUV/2 discrete mode in both diffuser view and lamp view. The discrete mode calibration tests were performed between June 14 and October 2, 2005. We use these data to validate the sweep mode reflectivity calibration.

11.3.1. Discrete Mode Measurement Sequence

Figure 11.7 illustrates the discrete mode diffuser reflectivity calibration sequence. Only one spectral line profile is scanned in each discrete mode sequence. The complete calibration sequence has approximately 60 scans and lasts about 32 minutes. As with the standard sweep mode diffuser reflectivity monitoring operation, the discrete mode operation is performed on the night side of an orbit. The discrete mode calibration sequence is constructed so as to approximate the standard sweep mode sequence. It begins with 24 scans in diffuser view, then alternates between lamp and diffuser views three times with 12 scans each. These 4 groups of scans are approximately equal in timing and function to those in a sweep mode sequence. As indicated in Figure 11.7, some mixed view modes may occur at times during transition from the lamp view to diffuser view. These scans in the mixed modes are rejected from the reflectivity calculation.

Because of the much longer total integration time for a single line profile, the signal-to-noise ratio for discrete mode data is generally much better than for sweep mode data. Note also the difference in data sampling. The grating in the discrete mode is locked at a designated position to get each data sample, while the grating in the sweep mode is moved 2 steps for a single data point. Each grating position in the discrete mode is actually measured by the grating position decoder, while only one grating position at the end of every 20 steps in a sweep mode scan is actually read from the instrument. NOAA-18 SBUV/2 has shown no grating position errors in discrete mode to date. Differences between discrete mode and sweep mode reflectivity measurements do not affect the results, as shown for NOAA-14 SBUV/2 [DeLand *et al.*, 1998].

11.3.2. Reflectivity Calculation in Discrete Mode

In discrete mode, each scan has 12 samples. By using a sample separation of two grating steps, a single discrete scan covers a large part of the emission line profiles (about 1.8 times the FWHM). Figure 11.8 shows the measured 253.7 nm and 404.8 nm line profiles. The peak positions in discrete mode are slightly shifted in comparison with sweep mode data due to differences in data sampling and grating position readout methods as mentioned above. After applying the same corrections for the detector characteristics as were used for the sweep mode measurements, all 12 samples were summed to give the integrated line intensity.

Figures 11.9 and 11.10 illustrate the line intensity drift for two calibration sequences at 253.7 nm and 404.8 nm, respectively. Data from both diffuser view and lamp view are plotted together to show the overall lamp behavior. The line intensities are normalized to minimize the difference between the interpolated values in lamp view and the measured values in diffuser view. After a significant decrease during initial lamp warming up time, the line intensity at 405 nm still drifted about 1% during the scans used for the reflectivity calculation. In addition, the time dependence of the drift was not linear during the measurement sequence. Therefore, the line intensity measurements in diffuser view in the last 8 (or 10) scans of the first group and the middle 8 (or 10) scans of the third group were fitted with a cubic function (*dot-dash line*) to provide interpolated line intensity values in diffuser view that correspond to the lamp view measurements in the second group of scans. The first diffuser reflectivity value is then derived as the ratio of the interpo-

lated line intensity in diffuser view to the measured line intensity in lamp view. In the lamp view (*asterisks*), the line intensity is normalized to the last available scan. Cubic interpolation is used in this instance to estimate the lamp view line intensities for the third group of scans (*solid line*), and the second diffuser reflectivity value is derived as the average of the measured line intensities in diffuser view to the interpolated line intensities in lamp view. The deviation between the two derived reflectivity values are less than 0.1% for strong lines, which is better than the sweep mode results using linear interpolation. Finally, the two derived reflectivities are averaged to give a daily value.

11.3.3. Statistical Uncertainty in Discrete Mode

The statistical uncertainty for a discrete reflectivity measurement also includes signal fluctuations, instrument noise and lamp intensity drift. The uncertainty due to the line intensity drift was estimated using the maximum deviation of the line intensity from the average value used for the line intensity interpolation. Scan-to-scan measurement noise was estimated from the standard deviation of the measured line intensities from the fitted or interpolated values in the same view configuration, divided by the square root of the number of measurements. No uncertainty is associated with the grating position error because there has been no grating position drive error. The total statistical uncertainty in the calculated reflectivity is expressed as:

$$\sigma = \sqrt{\Delta_1^2 + \sum_{i=1}^3 \sigma_{1i}^2 + \Delta_2^2 + \sum_{i=1}^3 \sigma_{2i}^2} \quad [11.4]$$

where Δ_1 and Δ_2 are respectively the line intensity drift for the first and second derived reflectivities, σ_{1i} and σ_{2i} are respectively the standard errors due to the noise and the summations are taken over three groups involved in each derived reflectivity. As shown in Figures 11.9 and 11.10, the lamp source drifts dominated the estimated uncertainties, representing ~70% of the uncertainty at 404.8 nm.

11.4. Lamp Polarity Effect

The power supply to the Hg lamp reverses polarity each time the lamp is turned on. This feature was added for FM#5 and all subsequent SBUV/2 instruments to improve long-term lamp stability by varying the position of the Hg lamp arc. Figure 11.11 shows the impact on the 254 nm line intensity for lamp view and diffuser view data. Note that the Hg lamp intensity decreases by approximately 26% through September 2005, comparable to the NOAA-16 and NOAA-17 SBUV/2 lamp changes during early operations. The two symbols in Figure 11.11 represent the different polarities, assigned arbitrarily since there is no telemetry information about the polarity state. The polarity for each lamp usage was assigned according to the Hg lamp operation history. The polarity effect shows up in the derived reflectivity data (*e.g.* Figure 11.6). There is no physical reason why the true diffuser reflectivity would change in conjunction with mercury lamp polarity changes. Therefore, we believe that this effect is an artifact in the reflectivity data. There is no reason to prefer one polarity state over the other, so we use an average reflectivity between the two polarities.

We fit the data with a functional form that includes a polarity term. The fitting function can be written as:

$$f_{\lambda}(x) = R_{\lambda} + a_{p\lambda}p(x) \quad [11.5]$$

where x is the time, $p(x)$ is equal to ± 1 depending on the polarity state at the measurement time, $a_{p\lambda}$ is the correction for the polarity, and R_{λ} is the reflectivity after the polarity correction. We choose a constant reflectivity for this analysis since we have not accumulated sufficient measurements to determine any time-dependent reflectivity changes. Table 11.1 lists the derived polarity corrections for strong lines, based on fitting Equation 11.5 to the first 11 days of measurement. The average polarity correction is $a_{p\lambda} = -0.31\%$, which is slightly larger than the results for NOAA-16 and NOAA-17 ($a_{p\lambda} = -0.20\%$ and -0.27% , respectively) but significantly smaller than NOAA-14 ($a_{p\lambda} = -0.50\%$). Figure 11.12 shows the reflectivity measurements with the polarity effect removed.

11.5. Diffuser Reflectivity Stability

11.5.1. Reflectivity Changes after Diffuser Decontamination

The diffuser decontamination procedure, consisting of heating the diffuser plate during the dark portion of two consecutive orbits, was performed on June 19, 2005. Diffuser reflectivity measurements were performed once immediately before the procedure and twice after the procedure. The first solar irradiance measurements were made on June 21, interleaved with more diffuser reflectivity calibrations. However, the onboard mercury lamp heater was accidentally turned off immediately after the decontamination procedure. The lamp spectral intensity in the following three calibration sequences was clearly unstable. The measured line intensities were up to $\pm 20\%$ different from the regular intensity level, as shown by the low values for 254 nm in Figure 11.11. Diffuser reflectivities derived from these three sequences were also significantly different from previous values, and were also discarded. As a result, we do not have valid measurements immediately following the decontamination procedure to evaluate possible diffuser reflectivity changes.

However, the decontamination procedure has not been observed to cause any significant change for diffuser reflectivity in previous SBUV/2 instruments. We show in Section 11.5.3 that the average change in diffuser reflectivity after solar exposure relative to the measurements before decontamination is only about 0.3%. Figure 11.13 shows the diffuser plate temperature and the diffuser heater current for 2005 day 170. The diffuser heater was operated on the night side during the first two orbits of the day. The peak diffuser plate temperature during each orbital thermal cycle increased from $\sim 28^{\circ}\text{C}$ to $\sim 37^{\circ}\text{C}$. This is only slightly higher than the maximum diffuser temperature observed at the Northern Hemisphere terminator from normal solar heating, which occurs 13-14 times each day. Thus, while the decontamination procedure may hold the diffuser plate at an elevated temperature for a longer time than usual, it does not appear to represent a significant thermal event.

11.5.2. Reflectivity Changes after Initial Solar Exposure

Figures 11.14 and 11.15 show the measured diffuser reflectivity data at 253.7 nm and 404.8 nm through September 2005. Symbols ‘×’ and ‘*’ indicate the lamp polarities, which have been corrected as discussed in Section 11.4. NOAA-18 SBUV/2 began regular weekly diffuser reflectivity calibrations in August 31, 2005. It is still too early to evaluate long-term trends. In reports for previous SBUV/2 instruments, we tried to report diffuser reflectivity changes after the first solar exposure in orbit. The reported changes were often small and comparable to measurement uncertainties. In the present report for NOAA-18, we do not have valid diffuser reflectivity measurements immediately after the first solar exposure, as discussed in the previous section. Therefore, the initial solar exposure is now defined as a total of 18 solar exposures between June 19 and June 29. The average of four diffuser reflectivity measurements between June 14-18 is taken as the pre-exposure condition, and the average of five measurements between June 29-July 2 is taken as the post-exposure condition. Table 11.2 lists the reflectivity values and changes resulting from the initial solar exposure. Figure 11.16 shows that there were no significant reflectivity changes at wavelengths longer than 300 nm, and that only –0.5% changes were observed at short wavelengths (< 254 nm).

11.5.3. Comparison with Prelaunch Calibrations

Extensive prelaunch diffuser reflectivity calibrations were performed in 1996 to obtain a base line for monitoring the diffuser reflectivity stability and to determine difference of the reflectivity measurements between in air and in vacuum. Among more than 100 follow-up diffuser reflectivity calibration sequences, the most important ones are based on the prelaunch calibration performed in April 2003 after the diffuser cleaning. The prelaunch reflectivity values are listed in Table 11.3, Vol. 1 [[Data Book](#)]. The prelaunch values listed in Table 11.3 in this report are averages over eight reflectivity calibration sequences on the primary test fixture (PTF) in April 2003, when the last radiometric calibrations were performed. The 185 nm data were corrected for absorption in air using results from 1996 vacuum calibration tests. Ball Aerospace processed the prelaunch reflectivity data with nominal interrange ratio values ($IRR_{12} = IRR_{23} = 100$) rather than the observed values, which were discussed in Section 9. No corrections were applied for nonlinearity, as well. In order to estimate necessary corrections to the reported prelaunch values, we processed the first sequence of diffuser reflectivity calibration in orbit with the nominal calibration as used by Ball Aerospace, and compared the results to reflectivity data processed with updated calibration parameters as derived in this report. Table 11.3 lists the estimated correction to the original prelaunch values for each strong line (*column 3*), as well as revised prelaunch reflectivity values (*column 4*). Figure 11.17 shows that the initial diffuser reflectivity values observed on-orbit are slightly higher than the revised prelaunch data at 313 nm and 365 nm, and slightly lower than the prelaunch values at other wavelengths. Table 11.3 lists reflectivity changes relative to the revised prelaunch values for the first inflight measurement (*column 5*) and for the average of all measurements during the A&E period (*column 6*). All strong line reflectivity changes are less than $\pm 1\%$ except for the 185 nm line. No changes were made in the albedo calibration for analysis of the initial solar irradiance data.

TABLE 11.1
Hg Lamp Polarity Correction: On-Orbit Data

<i>Wavelength [nm]</i>	<i>Polarity Correction</i>
185.00	-0.30(±0.09)%
253.71	-0.37(±0.07)%
296.82	-0.31(±0.11)%
313.13	-0.22(±0.14)%
365.24	-0.27(±0.10)%
404.81	-0.26(±0.10)%

TABLE 11.2
Inflight Diffuser Reflectivity Changes After All A&E Solar Exposures

<i>Wavelength [nm]</i>	<i>Before Solar Exposure</i>	<i>After Solar Exposure</i>	<i>Reflectivity Change</i>
185.00	0.012810(±0.000031)	0.012756(±0.000016)	-0.42(±0.27)%
253.72	0.017183(±0.000024)	0.017100(±0.000019)	-0.48(±0.18)%
296.84	0.018408(±0.000068)	0.018376(±0.000034)	-0.17(±0.41)%
313.13	0.018613(±0.000077)	0.018597(±0.000041)	-0.08(±0.47)%
365.24	0.019236(±0.000040)	0.019231(±0.000030)	-0.03(±0.26)%
404.81	0.019324(±0.000060)	0.019316(±0.000024)	-0.04(±0.33)%

TABLE 11.3
Prelaunch Diffuser Reflectivity Calibration

<i>Wave-length [nm]</i>	<i>Reflectivity Before Correction</i>	<i>Correc-tion Factor</i>	<i>Reflectivity After Correction</i>	<i>Initial Change On-orbit</i>	<i>Average Change during A&E Period</i>
185.00	0.01209(±0.00009)	0.92845	0.01303	-1.64(±0.71)%	-1.88(±0.71)%
253.72	0.01699(±0.00004)	0.98611	0.01723	-0.35(±0.30)%	-0.55(±0.26)%
296.84	0.01861(±0.00006)	1.00257	0.01856	-0.68(±0.40)%	-0.83(±0.37)%
313.13	0.01760(±0.00006)	0.95121	0.01851	0.52(±0.38)%	0.49(±0.38)%
365.24	0.01819(±0.00006)	0.94938	0.01916	0.41(±0.38)%	0.38(±0.34)%
404.81	0.01822(±0.00006)	0.93777	0.01943	-0.54(±0.38)%	-0.59(±0.35)%

The reflectivity at 184.9 nm in air was scaled up by the reflectivity change from air to vacuum in the thermal-vacuum chamber test.

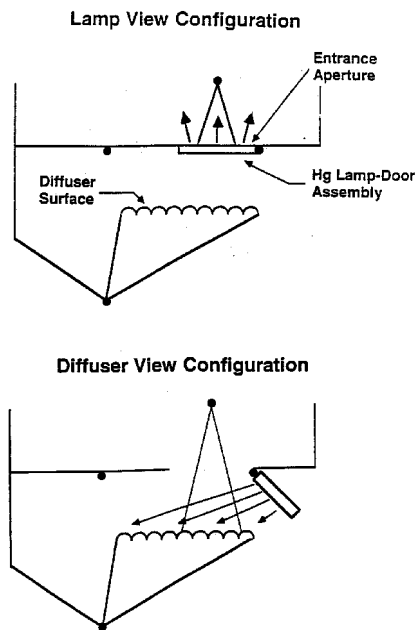


Figure 11.1: Onboard calibration system configuration: Lamp view, diffuser view.

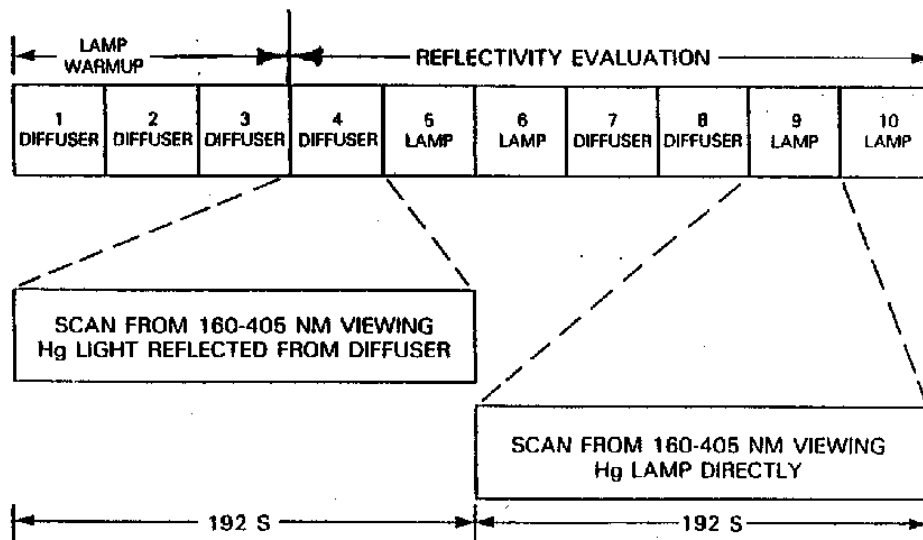


Figure 11.2: Sweep mode diffuser reflectivity measurement sequence.

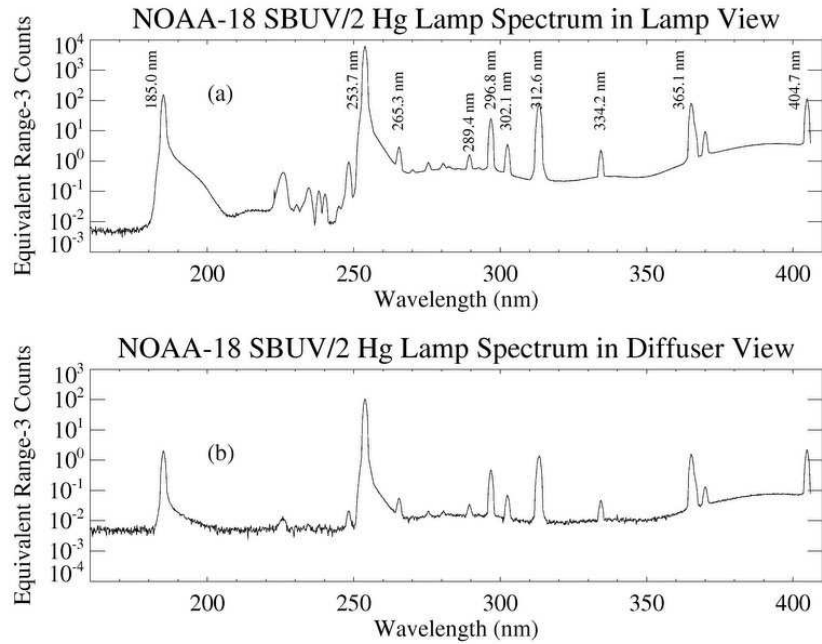


Figure 11.3: Mercury lamp spectrum: (a) Lamp view; (b) Diffuser view.

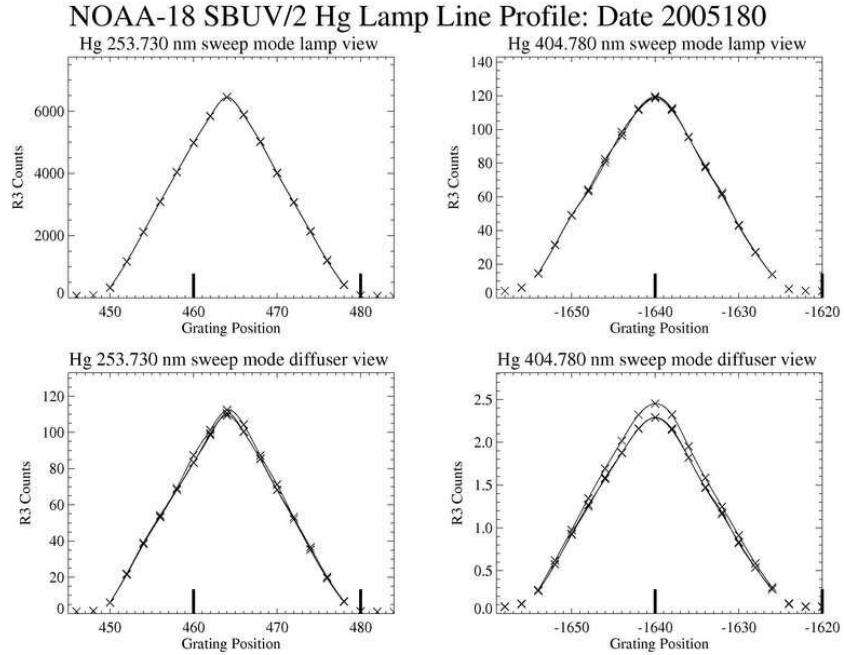


Figure 11.4: Sweep mode line profiles (lamp, diffuser): 253.7 nm, 404.8 nm.

NOAA-18 SBUV/2 Sweep Diffuser Reflectivity: Date 2005264 Seq 1

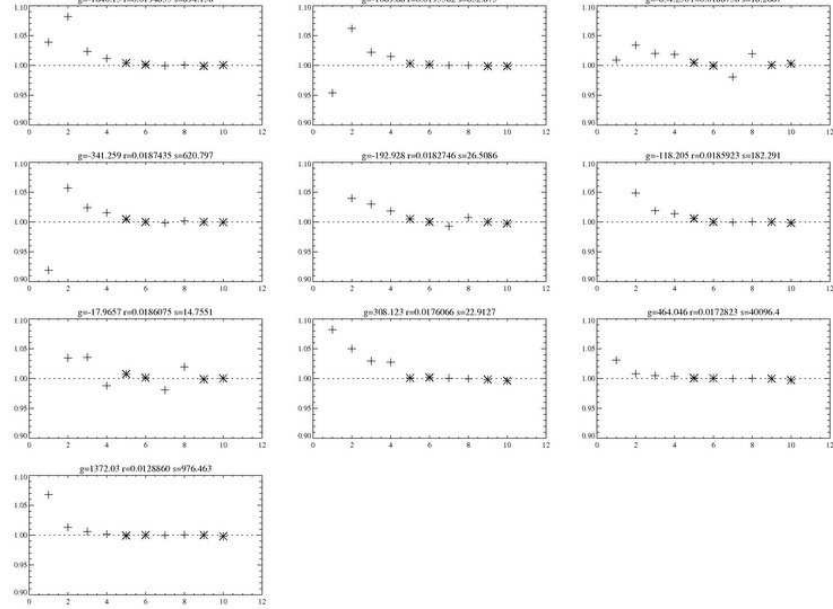


Figure 11.5: Line intensity evolution during sweep mode sequence: All lines.

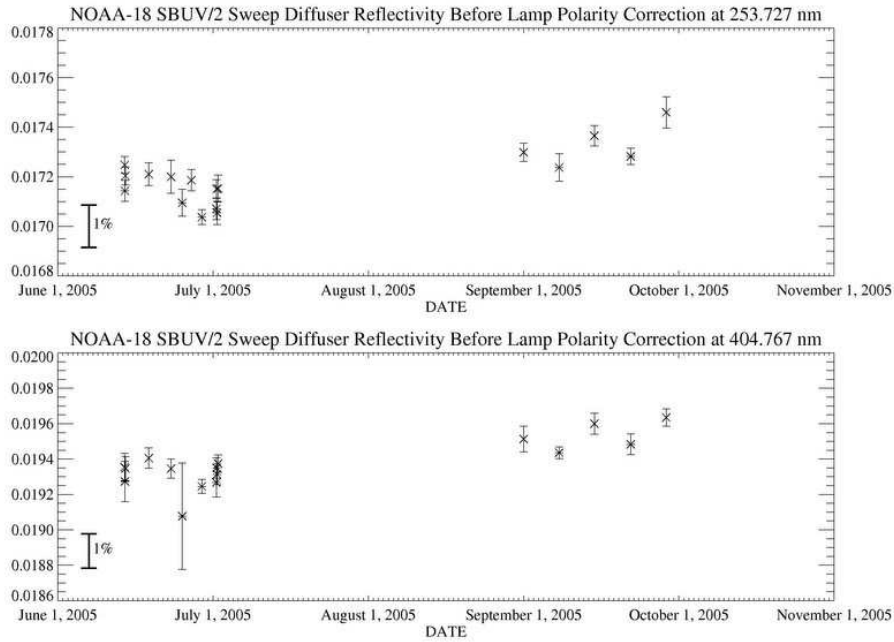


Figure 11.6: Diffuser reflectivity time series (no polarity correction): (top) 253.7 nm; (bottom) 404.8 nm.

Discrete Mode Reflectivity Calibration

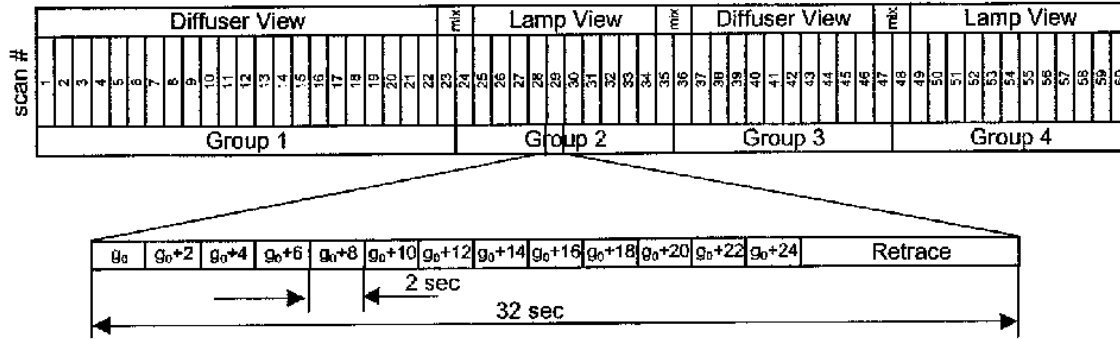


Figure 11.7: Discrete mode diffuser reflectivity measurement sequence.

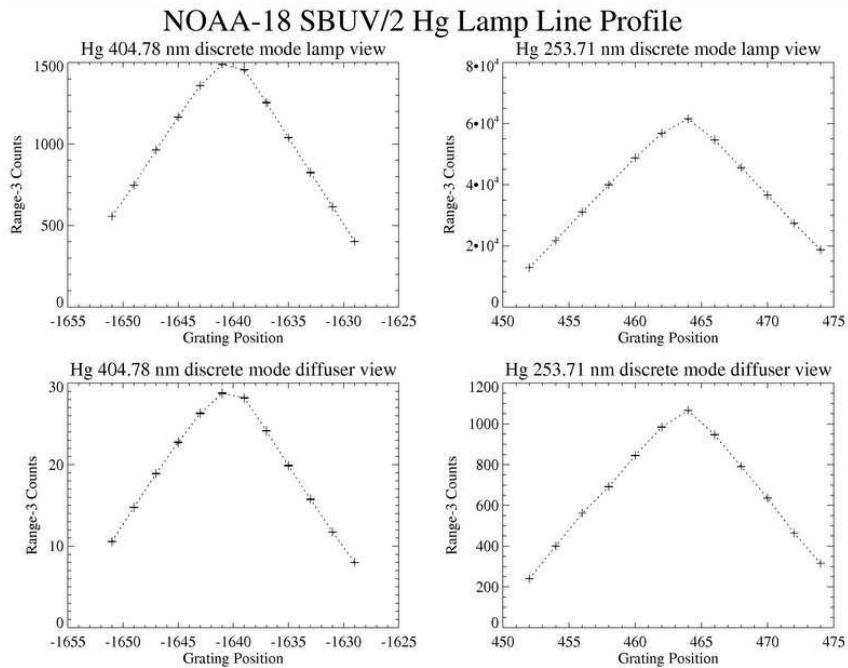


Figure 11.8: Discrete mode line profiles (lamp, diffuser): 404.8 nm, 253.7 nm.

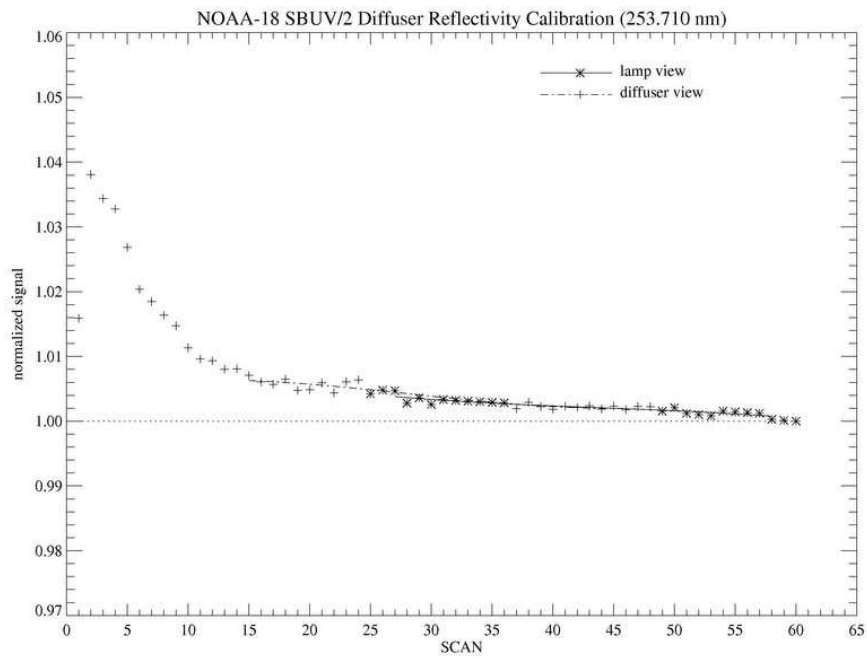


Figure 11.9: Discrete mode line intensity evolution at 253.7 nm.

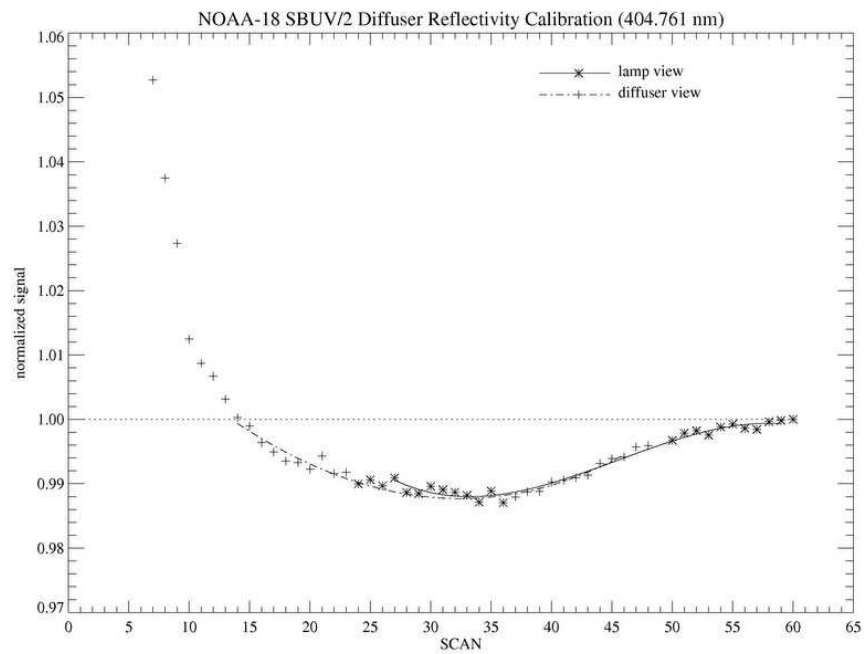


Figure 11.10: Discrete mode line intensity evolution at 404.8 nm.

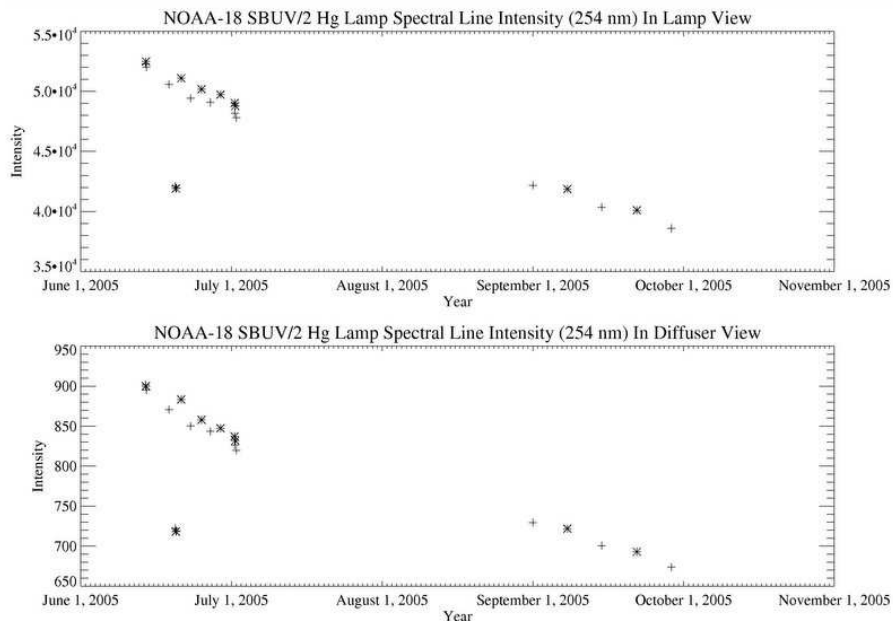


Figure 11.11: Hg lamp intensity time series at 253.7 nm: (top) Lamp view; (bottom) Diffuser view.

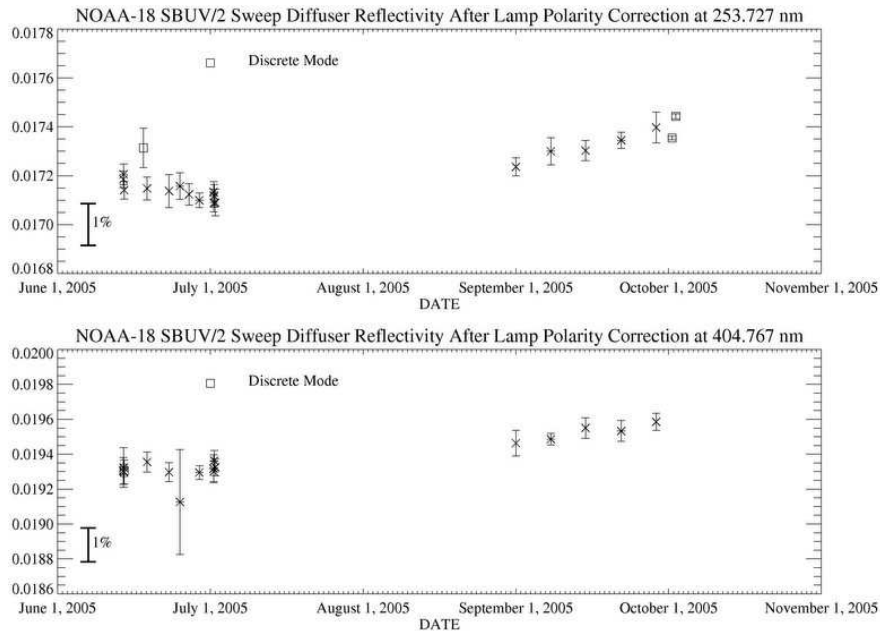


Figure 11.12: Diffuser reflectivity time series (after polarity correction): (top) 253.7 nm; (bottom) 404.8 nm.

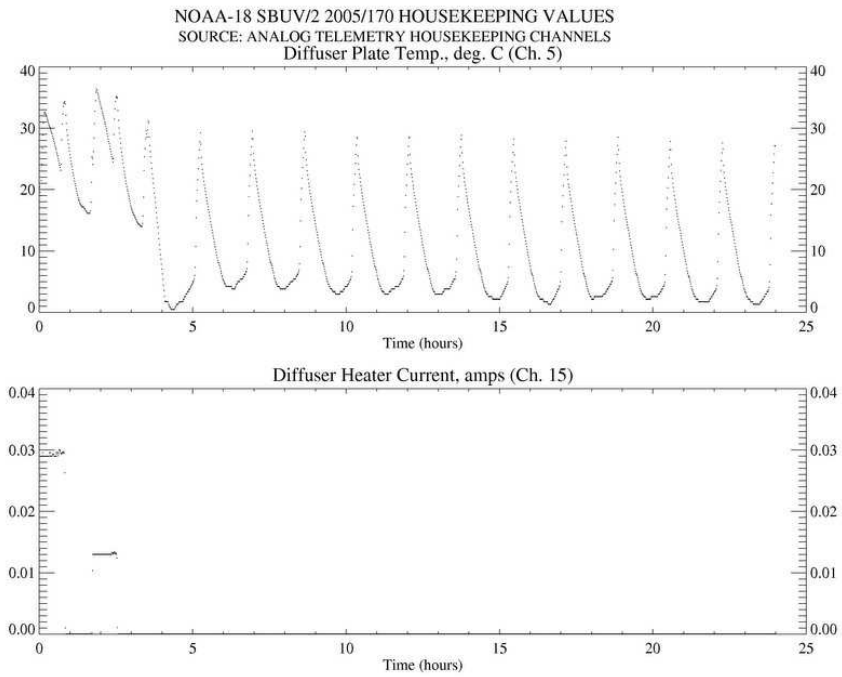


Figure 11.13: Diffuser plate temperature [*top*] and diffuser heater current [*bottom*] during diffuser decontamination procedure on 2005 day 170.

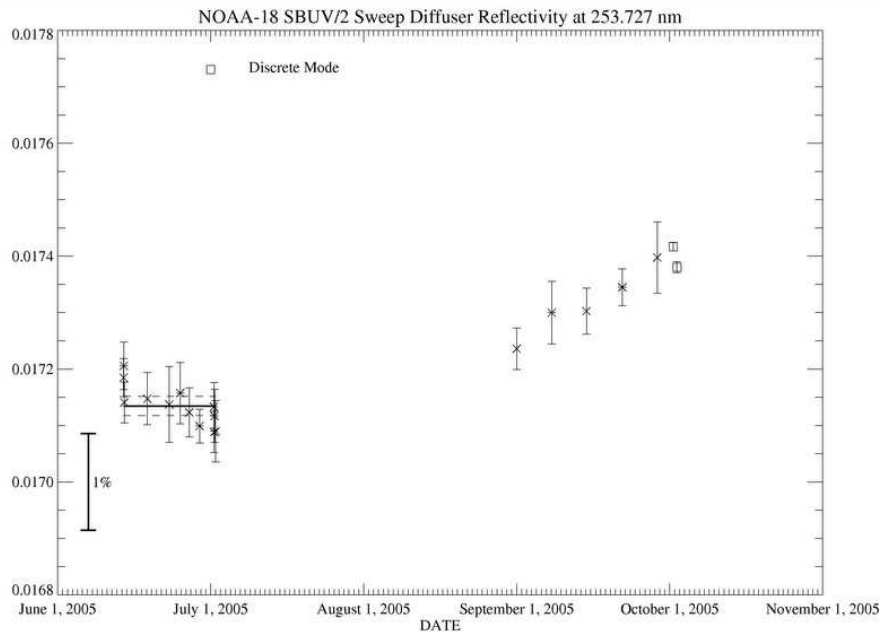


Figure 11.14: Diffuser reflectivity time series at 253.7 nm: June-September 2005.

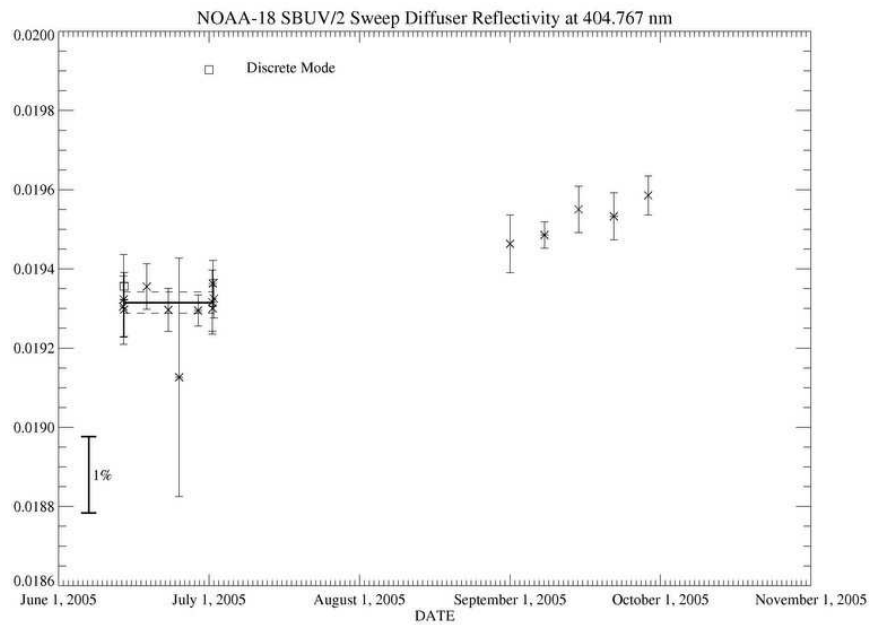


Figure 11.15: Diffuser reflectivity time series at 404.8 nm: June-September 2005.

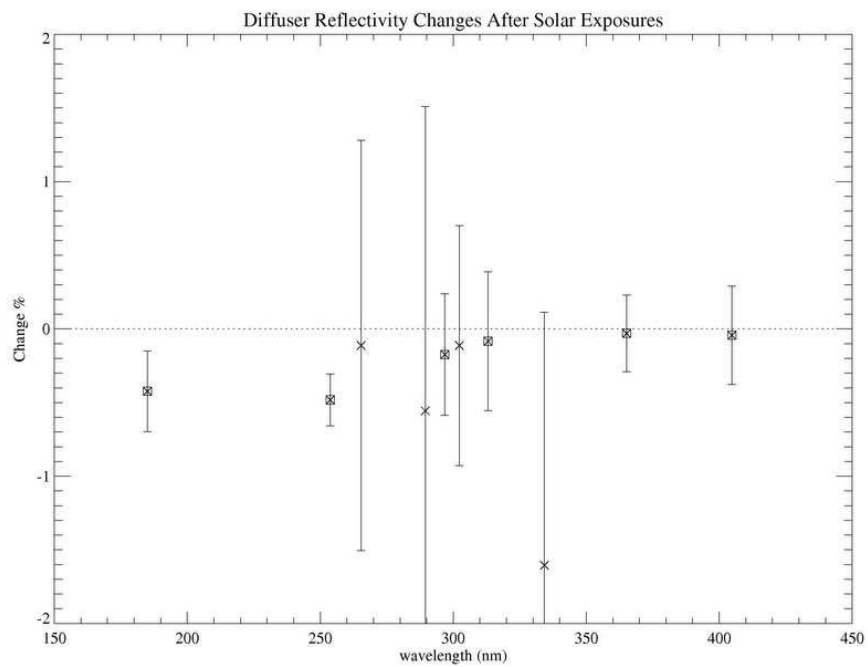


Figure 11.16: Inflight diffuser reflectivity changes after initial solar exposure. Strong lines are indicated by squares.

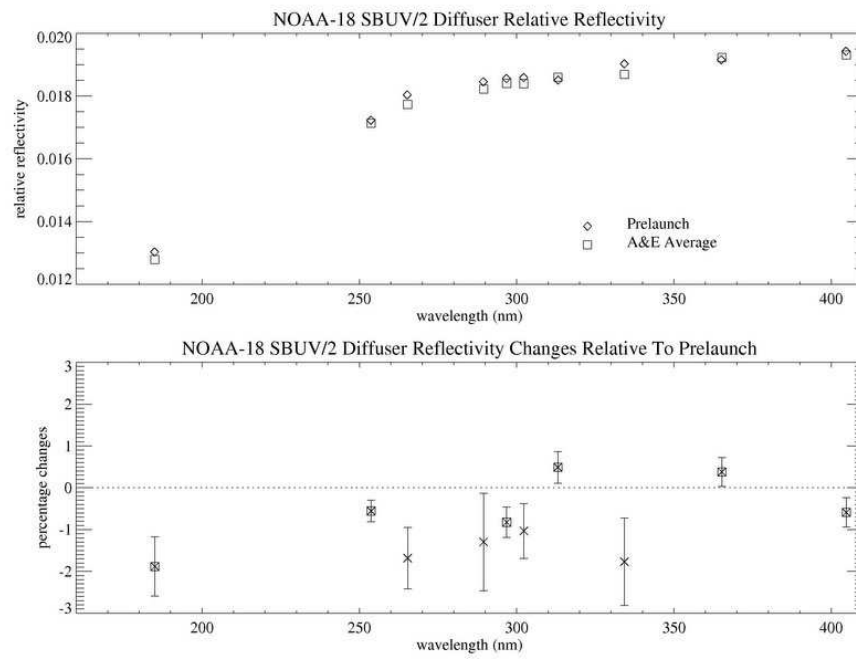


Figure 11.17: (top) Diffuser reflectivity spectral dependence; (bottom) Spectral dependence of diffuser reflectivity change: Inflight vs. prelaunch.

12. Radiometric Calibration

12.1. Prelaunch Characterization

The NOAA-18 SBUV/2 absolute radiometric calibration is based on measurements made in the laboratory before sensor launch and adjustments to the prelaunch constants suggested by observed on-orbit sensor behavior. The initial measurement procedures and results are described in depth in Section 8.2.6 of Volume 2 [Data Book]. Prelaunch procedures and results are reviewed only briefly here.

Ball Aerospace uses FEL lamps (1000 watt tungsten-halogen incandescent bulbs with quartz envelopes) for the wavelength range 260-406 nm, and deuterium-arc lamps to provide adequate signal at wavelengths below 260 nm. The spectral and goniometric (angular) characteristics of each source lamp were measured by NIST preceding and following each sequence of calibration measurements. The final prelaunch radiometric calibration measurements for the FM#7 instrument were completed in April 2003.

Figure 12.1 shows the ratio of calibration constants measured in air and vacuum as observed in sweep mode operation. Air-to-vacuum differences range from +3% to -6%, with a sharp peak associated with the Woods anomaly region near 232 nm. The large magnitude of these differences relative to air-to-vacuum differences observed with early SBUV/2 instruments has been considered and analyzed in several Ball Aerospace memoranda [Fowler, 1994, 1995].

The ratio between sweep mode and discrete mode calibration constants is nominally 12.5, based on the difference in sample integration times. Previous SBUV/2 instruments have observed slightly lower sweep/discrete ratios, although the differences are typically less than 1%. The NOAA-18 sweep/discrete calibration constant ratio is within 0.5% of the nominal value at all wavelengths for both radiance and irradiance data, as shown in Figure 12.2.

12.2. On-Orbit Validation

The difference between NOAA-18 “Day 1” discrete mode solar observations from 2005 day 171 processed with prelaunch calibration constants and solar irradiance values measured during the SSBUV-2 (Space Shuttle Backscattered Ultraviolet) flight in October 1990 are plotted in Figure 12.3. At the shortest wavelengths, differences exceed 9% and all deviations at the SBUV/2 discrete wavelengths exceed 2%. Note that these irradiance values were processed with radiometric calibration constants measured in air for consistency with the radiance calibration used in ozone processing. The irradiance value measured by the cloud cover radiometer (CCR) at 378.6 nm is also lower than the expected value. NOAA-18 sweep mode measurements made on the first day of observations also show spectrally dependent errors. These results are discussed further in Section 13.

Separate analysis of NOAA-18 radiance data showed comparable differences using prelaunch calibration constants. We conclude from these data that the “albedo” calibration [radi-

ance/irradiance] of the FM#7 instrument has not changed. We would like to produce accurate radiance and irradiance values for all users. We have therefore derived adjustment factors for ozone processing based on the solar irradiance difference shown in Figure 12.3. The values shown in Table 12.1 are essentially reciprocal values of the points plotted in Figure 12.3. A table of discrete radiance calibration constants obtained by multiplying measured pre-launch calibration constants by the calibration adjustment factors listed in Table 12.1 is presented in Table 12.2. A corresponding table of corrected irradiance calibration constants is presented in Table 12.3. These tables present the discrete calibration constants currently recommended for use in NOAA operational ozone processing.

12.3. “Day 1” Solar Irradiances

Since the instrument sensitivity change discussed in Section 12.2 prevents us from using observed NOAA-18 SBUV/2 solar irradiance values for ozone processing, we created the “Day 1” irradiance values by interpolating the SSBUV-2 irradiances to the NOAA-18 operational wavelengths. These irradiances were also adjusted for solar activity changes between October 1990 and June 2005, using $\Delta\text{Mg II} = -3.1\%$ and interpolated scale factors. The recommended “Day 1” irradiance values are listed in Table 12.4.

TABLE 12.1
Calibration Adjustment Factors for Ozone Processing

<i>Channel</i>	<i>Grating Position</i>	<i>Wavelength [nm]</i>	<i>Adjustment Factor</i>
1	486	252.039	1.0781
2	195	273.702	1.1025
3	67	283.164	1.0750
4	5	287.732	1.0561
5	-58	292.364	1.0570
6	-130	297.643	1.0634
7	-190	302.032	1.0585
8	-243	305.901	1.0592
9	-336	312.671	1.0469
10	-404	317.604	1.0377
11	-594	331.318	1.0178
12	-714	339.923	1.0295
CCR	-	378.62	1.0817

TABLE 12.2
Revised Radiance Calibration Constants [$mW/m^2/nm/count/ster$]

<i>Channel</i>	<i>Grating Position</i>	<i>Wavelength [nm]</i>	<i>Range 1</i>	<i>Range 2</i>	<i>Range 3 [anode]</i>	<i>Range 3 [cathode]</i>
1	486	252.039	1.4652e-06	1.4710e-04	1.3591e-02	3.3221e-02
2	195	273.702	1.4169e-06	1.4223e-04	1.3142e-02	3.2366e-02
3	67	283.164	1.5536e-06	1.5595e-04	1.4409e-02	3.5554e-02
4	5	287.732	1.4813e-06	1.4870e-04	1.3739e-02	3.3920e-02
5	-58	292.364	1.3859e-06	1.3912e-04	1.2855e-02	3.1751e-02
6	-130	297.643	1.3026e-06	1.3076e-04	1.2081e-02	2.9846e-02
7	-190	302.032	1.2516e-06	1.2564e-04	1.1609e-02	2.8678e-02
8	-243	305.901	1.2248e-06	1.2294e-04	1.1360e-02	2.8060e-02
9	-336	312.671	1.1623e-06	1.1667e-04	1.0780e-02	2.6612e-02
10	-404	317.604	1.1020e-06	1.1063e-04	1.0222e-02	2.5218e-02
11	-594	331.318	9.4116e-07	9.4479e-05	8.7296e-03	2.1477e-02
12	-714	339.923	8.7988e-07	8.8328e-05	8.1613e-03	2.0033e-02
CCR	—	378.62	—	—	8.0171e-03	8.0171e-03

TABLE 12.3
Revised Irradiance Calibration Constants [$mW/m^2/nm/count$]

<i>Channel</i>	<i>Grating Position</i>	<i>Wavelength [nm]</i>	<i>Range 1</i>	<i>Range 2</i>	<i>Range 3 [anode]</i>	<i>Range 3 [cathode]</i>
1	486	252.039	7.1201e-06	7.1476e-04	6.6042e-02	1.6144e-01
2	195	273.702	6.8284e-06	6.8549e-04	6.3336e-02	1.5599e-01
3	67	283.164	7.4313e-06	7.4600e-04	6.8928e-02	1.7007e-01
4	5	287.732	7.0789e-06	7.1063e-04	6.5660e-02	1.6211e-01
5	-58	292.364	6.6197e-06	6.6453e-04	6.1400e-02	1.5165e-01
6	-130	297.643	6.2224e-06	6.2463e-04	5.7714e-02	1.4258e-01
7	-190	302.032	5.9767e-06	5.9998e-04	5.5436e-02	1.3695e-01
8	-243	305.901	5.8438e-06	5.8664e-04	5.4204e-02	1.3389e-01
9	-336	312.671	5.5290e-06	5.5503e-04	5.1283e-02	1.2660e-01
10	-404	317.604	5.2232e-06	5.2434e-04	4.8447e-02	1.1952e-01
11	-594	331.318	4.4027e-06	4.4197e-04	4.0837e-02	1.0047e-01
12	-714	339.923	4.0969e-06	4.1127e-04	3.8000e-02	9.3275e-02
CCR	—	378.62	—	—	3.6061e-02	3.6061e-02

TABLE 12.4
“Day 1” Solar Irradiances for Ozone Processing

<i>Channel</i>	<i>Grating Position</i>	<i>Wavelength</i> [nm]	<i>Irradiance</i> [mW/m ² /nm]
1	486	252.039	42.027
2	195	273.702	186.70
3	67	283.164	331.09
4	5	287.732	333.73
5	-58	292.364	545.55
6	-130	297.643	538.55
7	-190	302.032	453.56
8	-243	305.901	586.79
9	-336	312.671	689.90
10	-404	317.604	792.54
11	-594	331.318	993.47
12	-714	339.923	1050.12
CCR	—	378.62	1302.74

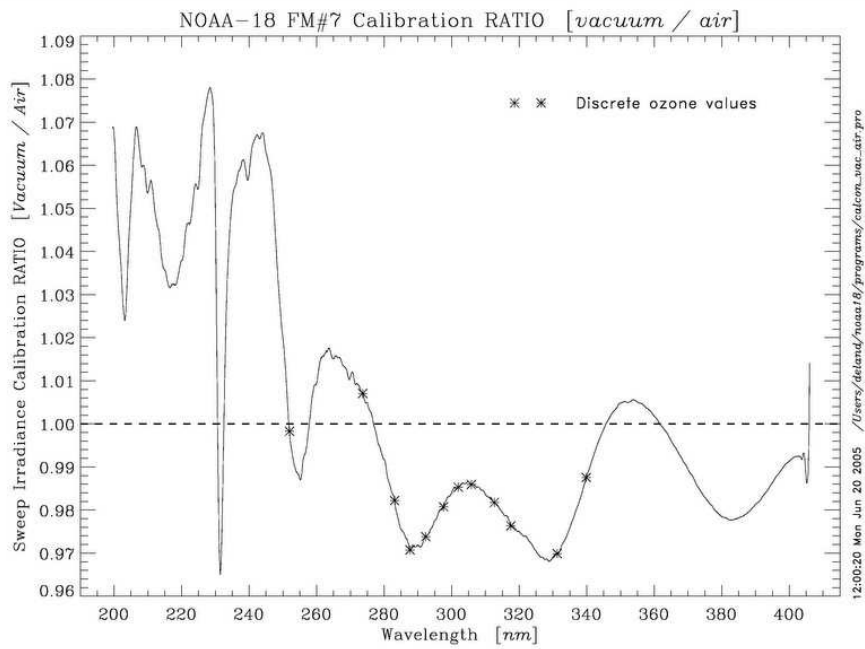


Figure 12.1: FM#7 sweep mode vacuum/air calibration ratio.

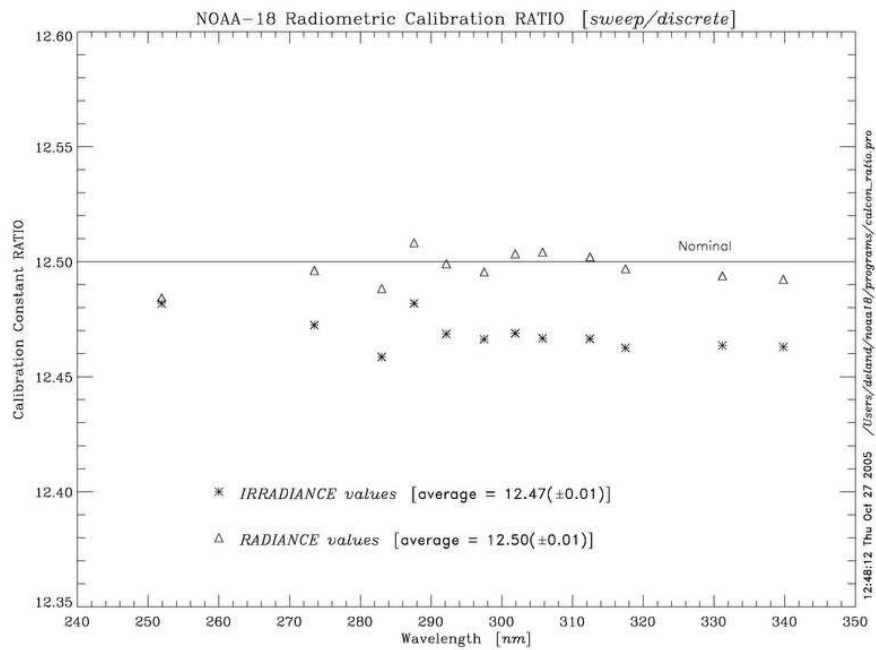


Figure 12.2: FM#7 sweep/discrete calibration ratio.

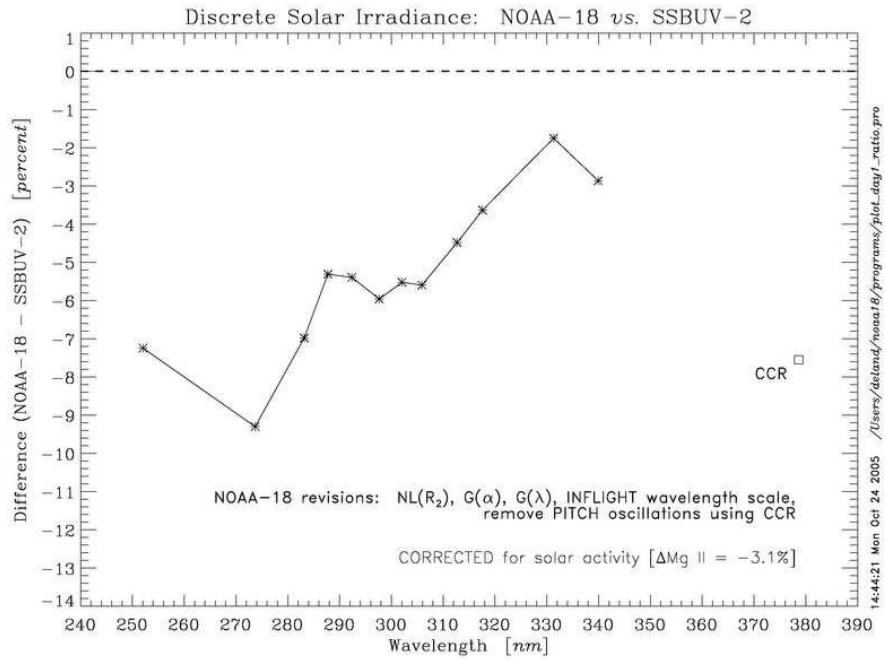


Figure 12.3: Discrete mode solar irradiance comparison: NOAA-18 SBUV/2 (20 June 2005) vs. SSBUV-2 (7-9 October 1990).

13. Solar Irradiance

13.1. Sweep Mode

NOAA-18 SBUV/2 sweep solar measurements are processed using a vacuum calibration to provide coverage down to 160 nm. Figure 13.1 shows the difference between the “Day 1” irradiance spectrum and a reference spectrum constructed from measurements taken during the ATLAS-1 Shuttle mission on March 29, 1992 [Thuillier *et al.*, 2004]. The NOAA-18 data have been corrected for differences in solar activity level between the dates of the measurements. The small-scale structure reflects minor wavelength scale differences between these spectra. The absolute difference has a significant spectral dependence, varying from -3% at 360 nm to -10% at 190 nm. These results are very comparable to the discrete mode comparisons with SSBUV-2 shown in Figure 12.3 when air-to-vacuum calibration differences are considered. The irradiance difference changes character dramatically for $\lambda < 180$ nm, increasing to $+13\%$ at 175 nm and $+35\%$ at 165 nm. SBUV/2 calibration is more difficult below 190 nm due to rapid decreases in both instrument sensitivity and deuterium lamp signal. A correction function was derived for the sweep mode irradiance calibration by fitting the difference data in Figure 13.1 with a weighted smoothing function (*heavy line*) developed by SSAI staff. The correction was fixed for $\lambda < 165$ nm because the SBUV/2 data quality is low in that region.

When regular NOAA-18 solar measurements began in August 2005, it quickly became clear that significant calibration changes continued to occur on-orbit. Figure 13.2 shows the ratio of the daily average sweep spectrum on 2005/242 (August 30) to the initial sweep spectrum measured on June 20. No correction has been made for solar variation, which was $+1.1\%$ using the NOAA-17 Mg II index. The regular spectral structure between 250-406 nm is consistent with the air/vacuum calibration ratio shown by the dashed line.

Most optical surfaces in the SBUV/2 instrument are coated with magnesium fluoride (MgF_2) to enhance UV reflectivity at short wavelengths. Laboratory tests with SBUV/2 instruments consistently show larger vacuum/air calibration differences than can be explained by changes in the index of refraction. Ball Aerospace personnel have studied this behavior, and speculate that the MgF_2 overcoating absorbs water vapor in the laboratory, and that outgassing effects in vacuum cause the observed spectral dependence [Fowler, 1994, 1997]. The potential effects are exacerbated for later SBUV/2 instruments (FM#6, FM#7, FM#8), where the change from an optically contacted 4-segment depolarizer to an air spaced depolarizer adds six coated surfaces to the optical path. NOAA-17 SBUV/2 (FM#6) data showed rapid initial growth in the magnitude of the spectral features, decreasing asymptotically to a constant value after ~ 18 months.

13.2. Pitch Angle Oscillations

Examination of NOAA-18 solar irradiance data immediately revealed the presence of a regular variation, as shown in Figure 13.3 [*top panel*]. The amplitude varied from $\sim 0.3\%$ peak-to-peak at $\alpha = 0^\circ$ to 0.6% p-p at $\alpha = 20^\circ$. The periodic variation observed in CCR data [*middle panel*] is

identical, as shown by the complete cancellation in the monochromator/CCR ratio [*bottom panel*]. The variation is also observed in sweep mode data, as shown in Figure 7.7. Power spectral analysis of sweep mode monochromator data determined a period of approximately 8.7 seconds (Figure 13.4). Discussions with POES program engineers revealed that the NOAA-18 spacecraft is undergoing a regular pitch angle oscillation with a frequency of ~ 0.114 Hz [= 8.8 seconds], and a magnitude of $\pm 0.05^\circ$. The spacecraft pitch axis is closely aligned with the normal to the SBUV/2 diffuser plate, and the reported oscillations are consistent with the variation in incidence angle necessary to produce the observed irradiance fluctuations. SBUV/2 is apparently the only instrument on NOAA-18 that has a measurable effect in science data from this phenomenon. These data have helped spacecraft engineers to confirm that the oscillations are not an aliasing of a variation at a different frequency.

Lockheed Martin engineers have not yet identified a source mechanism for the oscillations. A software revision to the spacecraft control laws that would reduce (but not eliminate) the oscillations has been proposed, but not yet tested on orbit. We developed a correction function by assuming that all fluctuations in CCR data within a single scan represent errors caused by the pitch angle oscillation, and then using those results to adjust both monochromator and CCR irradiance values. This adjustment reduces the standard deviation of daily average discrete mode measurements by as much as a factor of 2. The pitch angle correction will be applied to all solar measurements used for long-term instrument characterization.

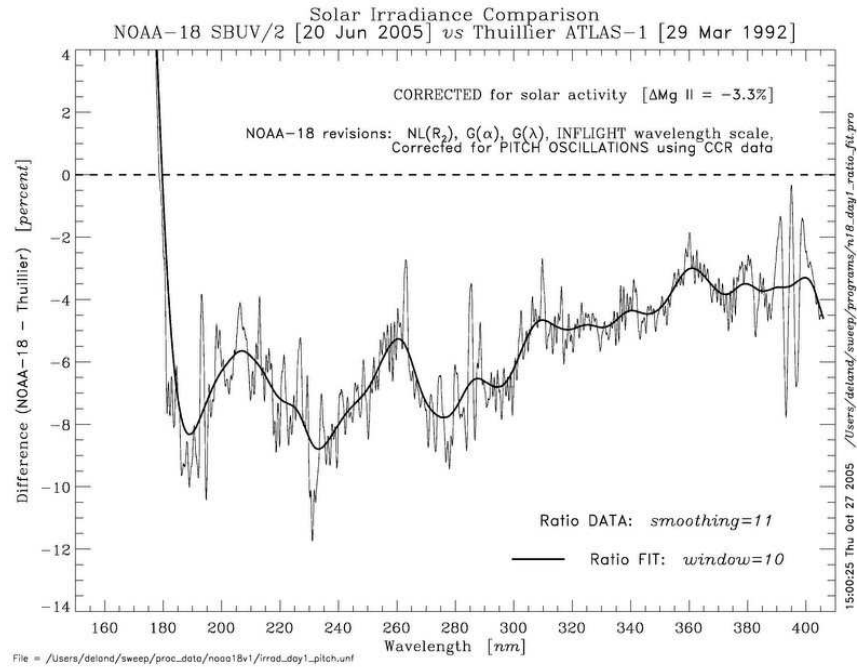


Figure 13.1: Sweep mode solar irradiance comparison: NOAA-18 SBUV/2 (20 June 2005) vs. Thuillier et al. [2004] reference spectrum from ATLAS-1 (29 March 1992).

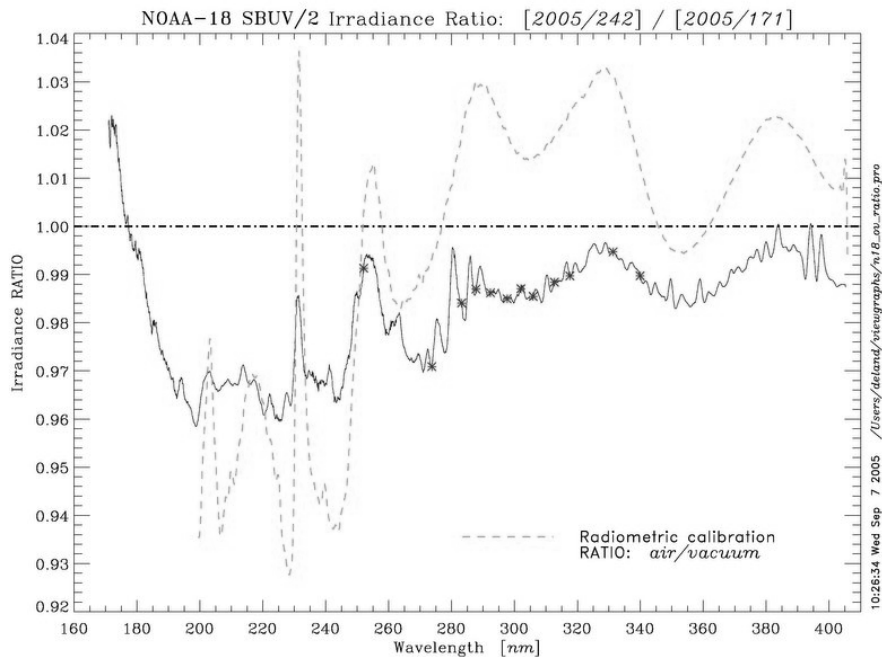


Figure 13.2: Sweep mode irradiance ratio: 2005 day 242 vs. 2005 day 171 + air/vacuum calibration ratio [dashed line].

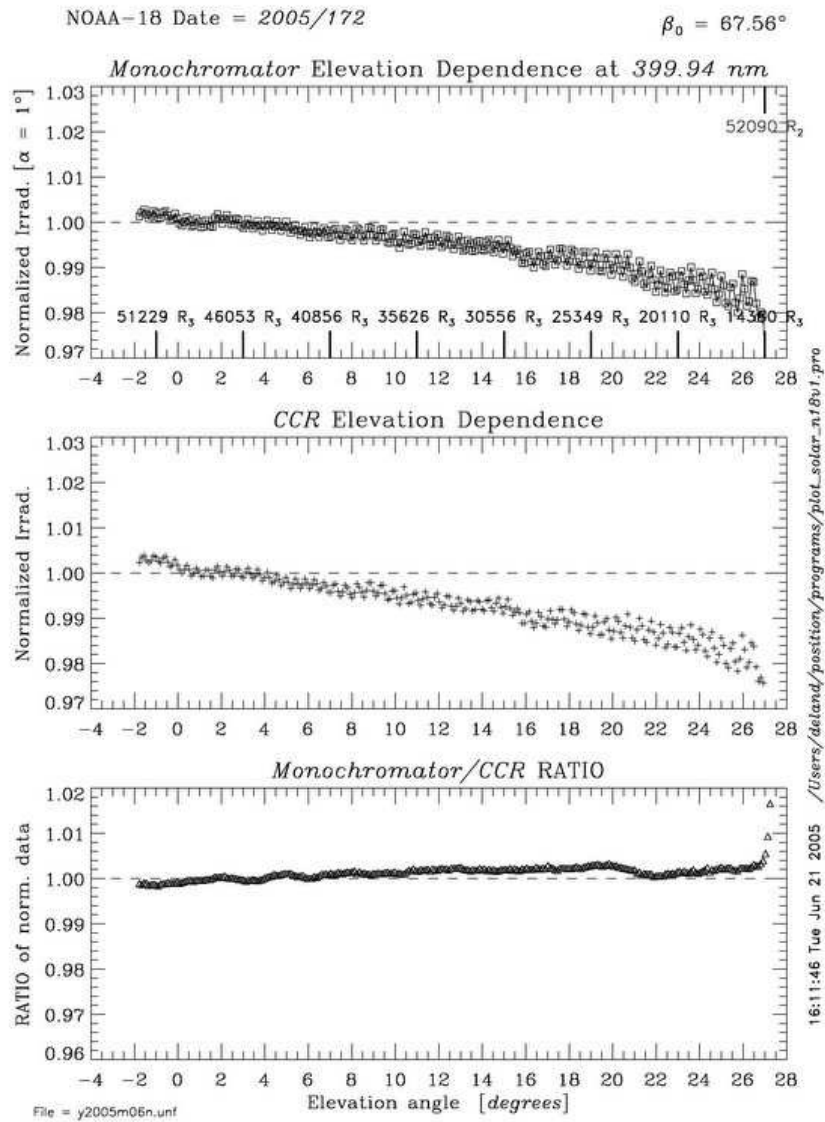


Figure 13.3: Position mode solar irradiance data at 400 nm for 2005/172.

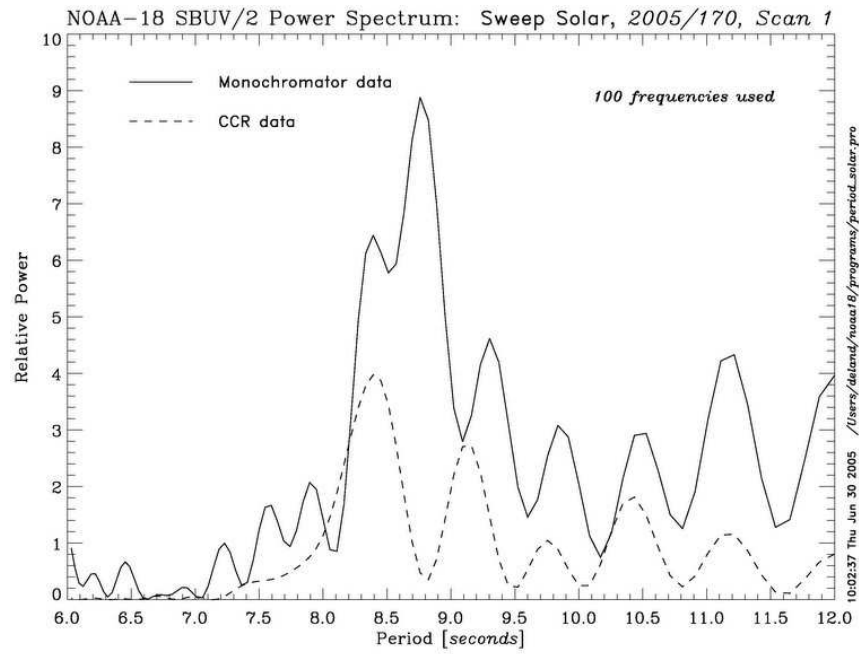


Figure 13.4: Power spectral analysis of sweep mode solar irradiance data.

14. Out-of-Band Response (OOBR) Correction

The origin of the out-of-band response (OOBR) error observed in on-orbit SBUV/2 radiance data is discussed in *DeLand et al.* [2005]. Preliminary correction function values were adopted at that time from the results of NOAA-17 on-orbit analysis, based on the similarity between FM#7 and FM#6 (NOAA-17) Hg lamp signals away from strong emission lines.

The on-orbit analysis technique used here identifies a baseline albedo signal (*vs.* latitude) at each wavelength, then calculates a linear fit to deviations of the monochromator albedo values relative to the coincident CCR albedo. Figure 14.1 shows an example of this method for NOAA-18 channel 2 (273.7 nm) data. The derived slope is transformed into a function of the 331 nm albedo (A_{331}) for operational use. This procedure can only be used for the shortest SBUV/2 wavelengths (252-292 nm), because surface reflectivity effects become important at longer wavelengths. The on-orbit correction coefficients derived using this method are more than a factor of 2 smaller than the prelaunch estimates.

For longer wavelengths (297-306 nm), a slit function model was developed that adds a specified “shoulder”, representing the OOBR error, to the nominal triangular shape (Figure 14.2). This modified slit function is then convolved with high resolution spectra (radiance=TOMRAD, irradiance=SOLSTICE) at specified conditions (*e.g.* SZA=30°, total ozone = 275 DU) to produce a calculated OOBR correction coefficient. The calculated values for NOAA-18 show excellent agreement with empirical results at shortest wavelengths (Figure 14.3). Revised OOBR coefficients are listed in Table 14.1. Figure 14.4 shows the spectral dependence of the calculated OOBR radiance error for a high scene reflectivity case ($R = 0.9$). The radiance corrections are approximately 5-7% for discrete ozone wavelengths between 250-290 nm, although higher values seen at solar absorption features.

TABLE 14.1
Revised OOB Correction Coefficients

<i>Channel</i>	<i>Grating Position</i>	<i>Wavelength [nm]</i>	<i>Correction Coefficient [prelaunch]</i>	<i>Correction Coefficient [revised]</i>
1	486	252.039	1.25e-04	0.57e-04
2	195	273.702	1.48e-04	0.62e-04
3	67	283.164	1.61e-04	0.63e-04
4	5	287.732	1.81e-04	0.69e-04
5	-58	292.364	1.41e-04	0.62e-04
6	-130	297.643	1.30e-04	0.79e-04
7	-190	302.032	1.30e-04	1.16e-04
8	-243	305.901	1.30e-04	1.08e-04
9	-336	312.671	0.0	0.0
10	-404	317.604	0.0	0.0
11	-594	331.318	0.0	0.0
12	-714	339.923	0.0	0.0

$$A_{\text{corrected}}(\lambda) = A_{\text{observed}}(\lambda) - C(\lambda) * A_{\text{observed}}(331 \text{ nm})$$

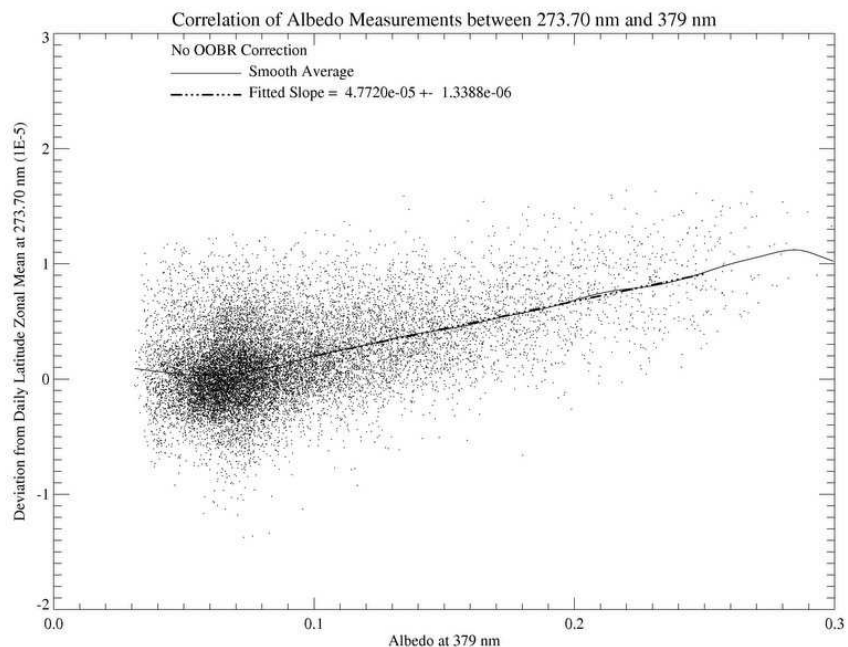


Figure 14.1: Albedo error at 273.7 nm vs. CCR albedo data.

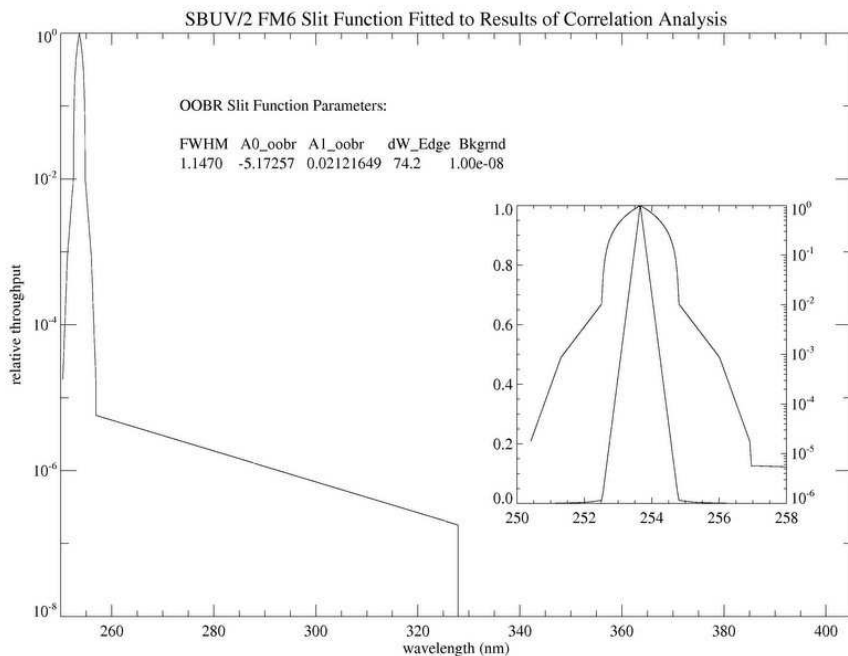


Figure 14.2: Slit function model for OOB analysis.

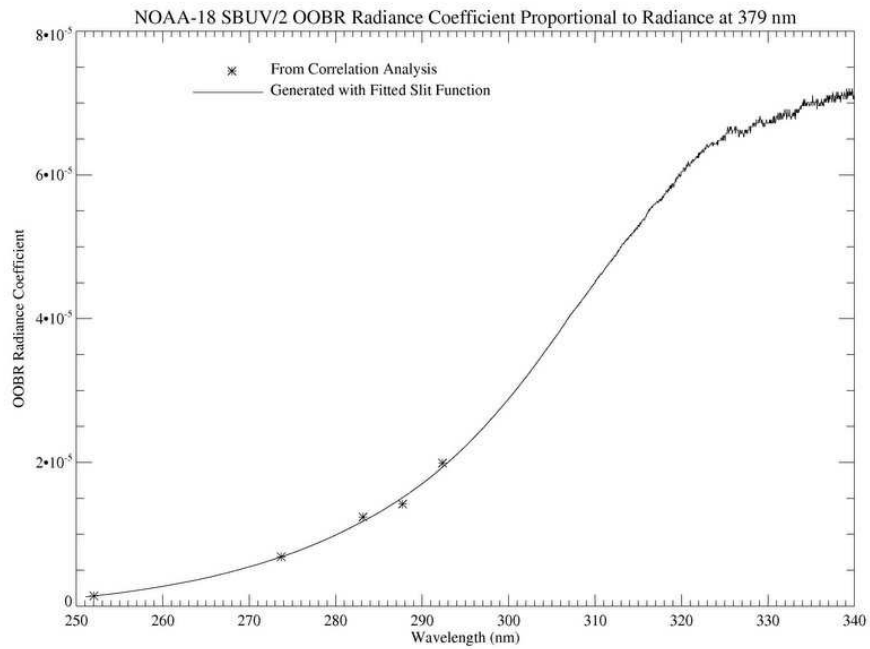


Figure 14.3: FM#7 OOB correction coefficient: Spectral dependence.

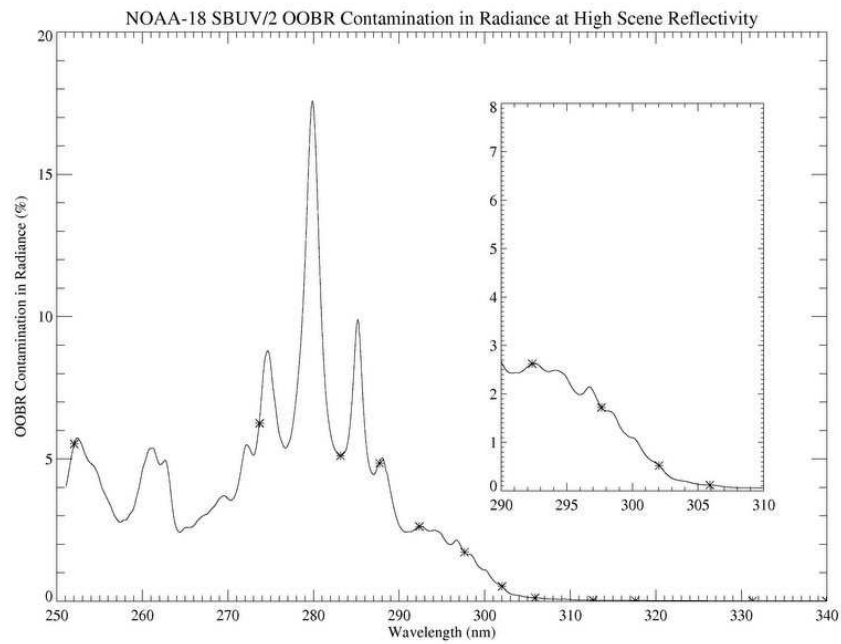


Figure 14.4: Calculated NOAA-18 OOB radiance error for high surface reflectivity [90%].

15. Ozone Validation

An initial processing of NOAA-18 ozone data was performed using prelaunch calibration data and SSBUV solar irradiance values from *DeLand et al.* [2005]. These data showed large differences (~25 DU) in total ozone comparisons with NOAA-16 data. SSAI reprocessed all NOAA-18 ozone data from June 2005 through September 2005 to determine initial total ozone pair adjustment factors for operational V6 processing, using the revised calibration constants and “Day 1” irradiances presented in Tables 12.3 and 12.4. The B-pair vs. D-pair equatorial difference calculated from this revised processing decreased to 1-2 DU in the first month. Figure 15.1 shows the variation in this difference during the first four months of NOAA-18 operation. The time-dependent calibration applied to these data was derived using only a few observations, so we expect to reduce the drift with further analysis. We calculated A-pair/B-pair, B-pair/C-pair, and A-pair/D-pair ratios to develop pair adjustment factors. The recommended pair adjustments for V6 processing are listed in Table 15.1, and represent averages of all available data.

Figure 15.2 shows comparisons between NOAA-16 total ozone and NOAA-18 total ozone processed with the updated pair adjustment factors. The NOAA-18 “best” ozone and A-pair ozone values are 1-2 DU lower than NOAA-16 for selected equatorial and mid-latitude bands (*top, middle panels*). NOAA-18 B-pair ozone is initially higher than NOAA-16, then drifts downward with time (*bottom panel*). We also compared ozone products from Version 8 (V8) algorithm processing. The rotational Raman scattering (or Ring effect) correction to N-values in the V8 code can change the inter-satellite ozone comparisons from the V6 results. Figure 15.3 shows that the B-pair difference is very similar to the V6 result (*top left*), but that the A-pair difference has increased to -5 DU (*top right*).

Figure 15.4 shows a comparison of NOAA-16 and NOAA-18 V8 profile ozone data for a single week in July 2005 at the Equator. The differences are less than $\pm 5\%$ for layers 1-13 ($z \leq 40$ km). Some larger differences are seen at higher altitudes, with NOAA-18 ozone values ~10% lower than NOAA-16 at layer 15 (~47 km).

TABLE 15.1
Total Ozone Pair Adjustment Factors Relative to A-pair [*inflight*]

<i>Ozone Pair</i>	<i>Adjustment Factor</i>	<i>Data Range for Analysis</i>
B	0.976	$\chi = 50-60^\circ$
C	1.120	$\chi = 70-80^\circ$
D	0.964	$\chi = 25-35^\circ, \text{ latitude} = \pm 15^\circ$

adjustment: $\Omega_A = \Omega_{\text{pair}} * \text{Factor}$

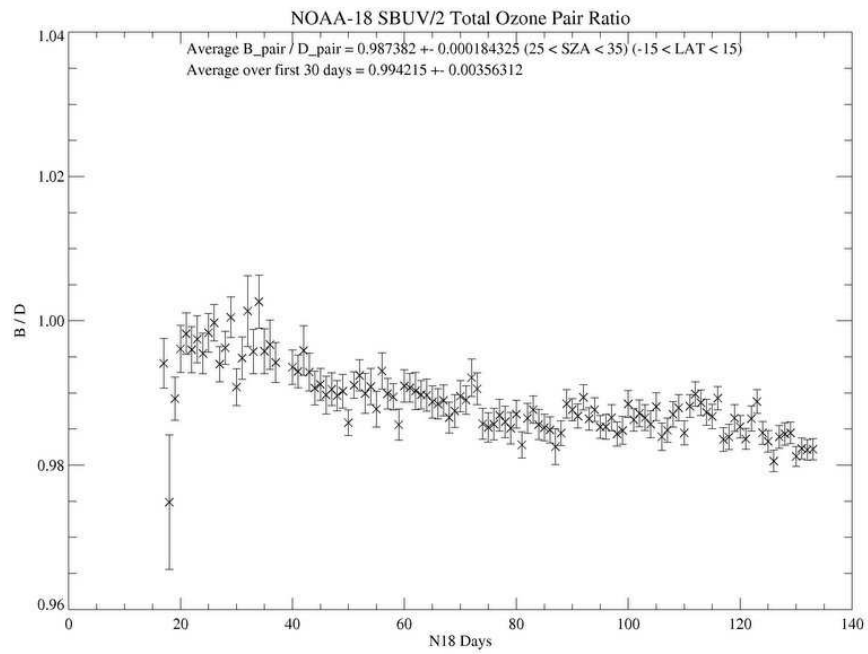


Figure 15.1: NOAA-18 V6 total ozone: Difference between B-pair and D-pair at Equator.

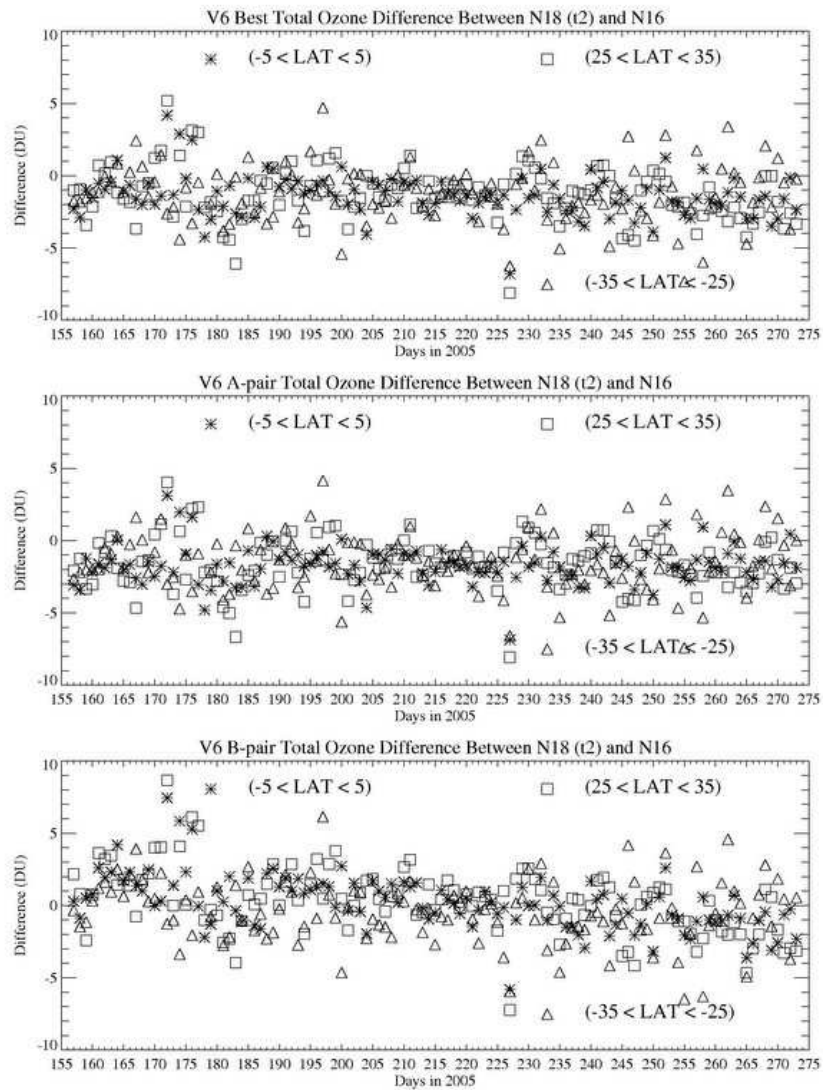


Figure 15.2: Comparison of V6 total ozone values between NOAA-18 and NOAA-16 in three latitude bands; (*top*) “Best” ozone; (*middle*) A-pair; (*bottom*) B-pair.

Version-8 Total Ozone Comparison Between NOAA-18 and NOAA-16

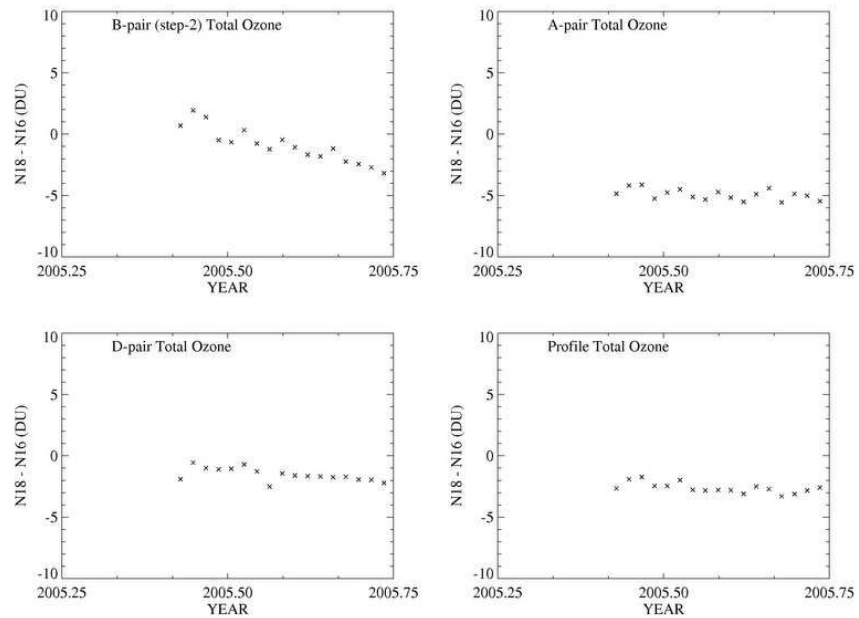


Figure 15.3: Comparison of V8 total ozone values between NOAA-18 and NOAA-16 at the Equator; (*top left*) B-pair; (*top right*) A-pair; (*bottom left*) D-pair; (*bottom right*) Integrated profile.

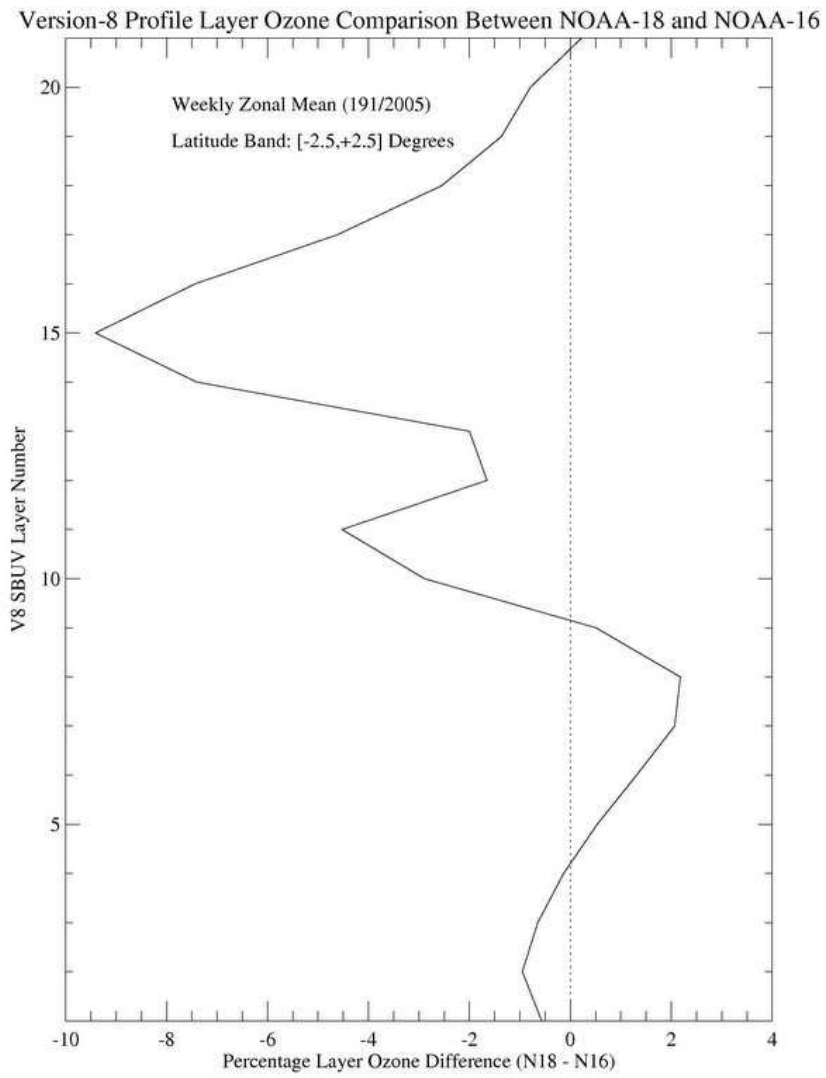


Figure 15.4: Comparison of V8 profile layer ozone values between NOAA-18 and NOAA-16 at the Equator in July 2005.

16. Conclusion

The NOAA-18 SBUV/2 instrument has successfully completed on-orbit activation and evaluation phase testing. The use of Range 3 anode data provides a significant improvement in data quality for total ozone products. The instrument characterization is generally consistent with prelaunch calibration data. Comparison of “Day 1” solar measurements with reference solar spectra show a significant change in absolute calibration from the final prelaunch measurements. Radiometric sensitivity changes have continued during initial operations, but appear to be slowing. Careful analysis will be required to derive appropriate time-dependent and wavelength-dependent instrument characterization, particularly during first 6 months of operation. Table 16.1 provides the location in this document of calibration data needed for SBUV/2 ozone processing.

TABLE 16.1
Ozone Processing Calibration Data for NOAA-18 SBUV/2

<i>Quantity</i>	<i>Location</i>
Wavelength Calibration Ebert Coefficients	Table 6.3, p. 30
Standard Ozone Wavelengths	Table 6.4, p. 31
Radiance Calibration Constants	Table 12.3, p. 92
Irradiance Calibration Constants	Table 12.2, p. 92
Electronic Offsets	Table 5.1, p. 18
Nonlinearity Corrections	Table 10.1, p. 67
PMT Temperature Correction	Table 8.1, p. 50
Interrange Ratio IRR_{12}	p. 57
Interrange Ratio IRR_{23A} (anode mode)	p. 57
Interrange Ratio IRR_{23C} (cathode mode)	Tables 9.1-9.2, p. 57
Goniometric Correction	Tables 7.1-7.4, p. 41-42
“Day 1” Solar Irradiances	Table 12.4, p. 93
Out of Band Response (OOBR) Correction Coeff.	Table 14.1, p. 102
Total Ozone Pair Adjustment Factors	Table 15.1, p. 105

References

- Ball Aerospace Engineering Division, Specification Compliance and Calibration Data Book for SBUV/2 Flight Unit #7 (S/N 008), IN021-A-049, Rev. A (2 volumes), 26 March 2004.
- DeLand, M. T., L. K. Huang, R. P. Cebula, S. L. Taylor, and C. G. Wellemeyer, *NOAA-14 SBUV/2 V6.1 Calibration Report*, **RSTX-3050-BJ8-MD-98-003**, 223 p., 2 October 1998.
- DeLand, M. T., and L. K. Huang, *NOAA-16 SBUV/2(FM#3) Activation and Evaluation Phase (A&E) Report*, **SSAI-2015-180-MD-2001-01**, 161 p., 29 June 2001.
- DeLand, M. T., L. K. Huang, and C. A. McKay, SBUV/2 FM#7 prelaunch instrument characterization for NOAA-N, **SSAI-2015-180-MD-2005-01**, 31 January 2005.
- Fowler, W. K., Spectral sensitivity characteristic of the SBUV/2 instrument – differences in air and vacuum, Ball SER **SBUV-WF-94-749**, 6 September 1994.
- Fowler, W. K., The differences in sensitivity of SBUV/2, FM#3, in air and vacuum, Ball SER **SBUV-WF-95-766**, 14 February 1995.
- Fowler, W. K., Depolarizer test recommendation, Ball SER **SBUV-WF-97-882**, 11 July 1997.
- Jaross, G., R. P. Cebula, M. DeLand, C. G. Wellemeyer, S. L. Taylor, R. D. McPeters, A. J. Krueger, P. K. Bhartia, E. Hilsenrath, and J. R. Herman, BUV instrument solar diffuser degradation, *Proc. SPIE Int. Soc. Opt. Eng.*, **3427**, 432-444, 1998.
- Pitz, E., Nonlinearity measurements on photometric devices, *Appl. Optics*, **18**, 1979.
- SASC Technologies, Inc., Solar Backscattered Ultraviolet Radiometer, version 2 (SBUV/2) User's Guide, **SASC-T-5-5085-028-85**, ver. 2, 198 p., 19 December 1986.
- Thuillier, G., L. Floyd, T. N. Woods, R. Cebula, E. Hilsenrath, M. Hersé, and D. Labs, Solar irradiance reference spectra for two solar active levels, *Adv. Space Res.*, **34**, 256-261, 2004.